FUSION-FISSION AND ASSOCIATED NUCLEAR STRUCTURE EFFECTS AT LOW ENERGIES

A THESIS

Submitted to the

FACULTY OF SCIENCE

THAPAR UNIVERSITY, PATIALA

for the degree of

DOCTOR OF PHILOSOPHY

by

Deepika Jain

SCHOOL OF PHYSICS AND MATERIALS SCIENCE

THAPAR UNIVERSITY

PATIALA-147004

(INDIA)

Dedicated to

My Beloved Parents

and other family members

Thapar University, Patiala

CANDIDATE'S DECLARATION

I hereby certify that the thesis entitled "**FUSION-FISSION AND ASSOCIATED NUCLEAR STRUCTURE EFFECTS AT LOW ENERGIES**" in partial fulfillment of the requirements for the award of Degree of Doctor of Philosophy in the School of Physics and Materials Science, Thapar University, Patiala, is a record of my own work carried under the supervision of Prof. Manoj K. Sharma. The matter presented in this thesis has not been submitted by me in part or full for the award of any other degree in any other university or institute.

Deepika jain

This is to certify that the above statement made by the candidate is correct to the best of our knowledge.

Prof. Manoj K. Sharma
(Supervisor and HOD)

Dean R&SP

External Examiner 22.11.14

Date 22/11/14

Acknowledgments

Thank God for the wisdom and perseverance that he has been bestowed upon me during Ph.D time, and indeed, through my life: "I can do everything through him who give me strength." After the completion of this thesis, as I look back, all those people come into my mind that stood by me during the last years and helped me contribute my bit to the world of science through my Ph.D.

Foremost, I would like to express my sincere and deepest gratitude to my supervisor, Prof. Manoj Kumar Sharma, Head, School of Physics and Materials Science, Thapar University, Patiala for the continuous support of my Ph.D study and research. I am very grateful for his patience, motivation, enthusiasm and immense knowledge. His guidance helped me in all the time of research and writing of this thesis. I could not have imagine having a better mentor for my Ph.D study. He is not only guided me but also trusted me to dabble with nuclear physics to achieve the goals I desired. I learned a lot from him about life, research, how to tackle new problems and how to develop techniques to solve them. His ability to select and to approach compelling research problems, high scientific standards, and hard work set an example. I admire his ability to balance research interests and personal pursuits. I can not forget to thank Madam Sharma for her motherly affection, care and of course the delicious food occasionally.

I am also very grateful to Prof. (Retd.) Raj K. Gupta, Physics Department, Panjab University, Chandigarh for his scientific advice and knowledge and many insightful discussions and suggestions. Their continuous feedback and interest through our meetings and mails contributed in a special way to the success of my thesis.

I express my thanks to Prof. Kulvir Singh for providing me the necessary facilities in the department and for his affectionate behavior throughout my research period. Special thanks to Prof. O. P. Pandey for the encouragement and moral support at bad times. It is also my pleasure to express my thanks to all the faculty and staff of the Physics Department for their cooperation and help. I would like to thank my committee members, Dr. Suneel Kumar, Dr. Alka Upadhyay and Dr. R. K. Sharma *for their useful suggestions during the progress report presentations. Thanks also goes to Dr. P. K. Bajpai, Dean of Research and Sponsored Projects for providing the possible research facilities.*

The thesis would not have come to a successful completion, without the help I received from my senior Dr. Raj Kumar, Postdoctoral Fellow, Dept. of Physics and Astronomy "G. Galilei", Univ. of Padova, Italy. Thank you for the fun and the encouraging discussions during my Ph.D career. Words are short to express my deep sense of gratitude towards other seniors, Dr. Birbikram Singh, Dr. Shefali Kanwar, Dr. Varinderjit Kaur, Dr. Gudveen Sawhney, Dr. Manpreet Kaur, Dr. Harjinder Singh. Sincere thanks to all my labmates Kirandeep Sandhu, Gurvinder Kaur, Rajni and other friends especially Dr. Rajni, Dr. Anupriya Jain, Meenakshi, Chandni, Samiksha, Rubina, Paramjyot Jha, Parveer, Sangeeta for their help, moral support and jovial company. Thanks for the friendship and memories.

Of course no acknowledgments would be complete without giving thanks to my grand parents (Mr. Shanti Prakash Jain and Mrs. Padmawati Jain) and parents (Mr. Pink Raj Jain and Mrs. Neeru Jain). My parents have instilled many admirable qualities in me and given me a good foundation with which to meet life. Their understanding, faith, advise, intellectual spirit and undescribable support to me throughout my whole life are invaluable. I am very grateful to my brother (Mr. Puneet Jain) and bhabhi (Mrs. Henna Jain) for constant help and encouragement. A special thanks to my niece Malya, whose smiling face have always made me refreshing. I am thankful to my cousin (Aashima Jain) for her love and support. You have been the most indispensable source of strength for me. Thank you for everything.

The financial support from Council of Scientific and Industrial Research (CSIR), as a senior research fellow is gratefully acknowledged.

Deepika Jain

Patiala
(Deepika Jain)
Date 22/11/14.

List of Publications

I. International Journals:

1. Skyrme forces and the fusion-fission dynamics of the ^{132}Sn+^{64}Ni→ ^{196}Pt* reaction, **Deepika Jain**, Raj Kumar, Manoj K. Sharma and Raj K. Gupta , Phys. Rev. C **85**, 024615 (2012).

2. Reaction dynamics of Pt* isotopes formed using stable and radioactive Sn beams, **Deepika Jain**, Raj Kumar and Manoj K. Sharma, Phys. Rev. C **87**, 044612 (2013).

3. Effect of deformation and orientation on interaction barrier and fusion cross-sections using various proximity potentials,
   Deepika Jain, Raj Kumar and Manoj K. Sharma, Nucl. Phys. A **915**, 106-124 (2013).

4. Formation and decay cross-sections of ^{66}As* formed in an exotic proton-halo ^{8}B induced reaction,
   Gurvinder Kaur, **Deepika Jain**, Raj Kumar and Manoj K. Sharma, Nucl. Phys. A **916**, 260-274 (2013).

5. Entrance channel effect with stable and radioactive beams using dynamical cluster decay model,
   Raj Kumar and **Deepika Jain**, Nucl. Phys. A **929**, 169-183 (2014).

6. Systematic analysis of hot Yb* isotopes using energy density formalism,
   Deepika Jain, Manoj K. Sharma, Raj Kumar and Raj K. Gupta, Eur. Phys. J. A **50**, 155 (2014).

7. Fusion Excitation Functions of ^{132}Sn+^{64}Ni reaction using ℓ-summed Wong formula,

Deepika Jain, Raj Kumar and Manoj K. Sharma, AIP Conf. Proc. **1423**, 126 (2012).

8. Entrance channel effects in the decay of ^{190}Pt* using radioactive Sn beams, **Deepika Jain**, Raj Kumar and Manoj K. Sharma, AIP Conf. Proc. **1524**, 209 (2013).

9. Fission dynamics of ^{240}Cf* formed in ^{34,36}S induced reactions, **Deepika Jain**, Gurvinder Kaur and Manoj K. Sharma, EPJ web of Conferences (accepted).

10. Alpha-decay Chain and Associated Cluster Emission from Neutron Deficient ^{237}Cf nucleus, **Deepika Jain** and Manoj K. Sharma, JPS Conf. Proc. (accepted).

II. In Conferences, Symposiums and Workshops:

1. Nuclear reaction dynamics using density dependent interaction potential, **Deepika Jain** and Manoj K Sharma, 14th Punjab Science Congress, Feb. 7-9, 2011, Pg-126, SLIET, Longowal, India.

2. Decay of ^{196}Pt* formed by radioactive beam of ^{132}Sn using dynamical cluster-decay model, **Deepika Jain**, Raj Kumar, Manoj K Sharma and Raj K. Gupta, 2nd National Conference on Advanced Materials and Radiation Physics (AMRP-2011), Nov. 4-5, 2011, RP-O-08, SLIET, Longowal, India.

3. Comparative study of different nuclear potentials in fusion of ^{48}Ca+^{96}Zr above and below the Coulomb barrier, **Deepika Jain**, Raj Kumar and Manoj K Sharma, DAE Symposium on Nuclear Physics, Vol. **56**, 550, Dec. 26-30, 2011, Andhra University, Vishakhapatnam, India.

4. Decay of ^{132}Sn+^{58}Ni→ ^{196}Pt* using Skyrme energy density formalism in dynamical cluster-decay model, **Deepika Jain**, Raj Kumar, Manoj K Sharma and Raj K. Gupta, DAE Symposium on Nuclear Physics, Vol. **56**, 512, Dec. 26-30, 2011, Andhra University, Vishakhapatnam, India.

5. Dynamics of ^{66}As* formed in exotic proton halo ^{8}B induced reaction at near barrier energies, Gurvinder Kaur, **Deepika Jain**, Raj Kumar and Manoj K Sharma, 11th International Conference on N-N Collision (NN2012), May 27-June 1, 2012, San Antonio, Texas.

6. Fusion excitation functions of ^{66}As formed in ^{8}B + ^{58}Ni reaction at near barrier energies, Gurvinder Kaur, **Deepika Jain**, Raj Kumar and Manoj K Sharma, DAE symposium on Nuclear Physics, , Vol. **57**, 502, Dec. 3-7, 2012, Delhi University, New Delhi.

7. Deformation effects on fusion cross-sections using various proximity potentials, **Deepika Jain**, Raj Kumar and Manoj K Sharma, DAE symposium on Nuclear Physics, , Vol. **57**, 504, Dec. 3-7, 2012, Delhi University, New Delhi.

8. Impact of radioactive beams in reaction dynamics of compound nuclear systems, **Deepika Jain**, Raj Kumar and Manoj K Sharma, International Conference on emerging trends in Physics for Environmental (ETPEMM-12), Pg-93, Dec. 17-19, 2012, Punjabi University, Patiala.

9. Isospin and deformation effects on spin dependent interaction potential., **Deepika Jain**, Manoj K Sharma, Raj Kumar and Raj K. Gupta, National Conference On Nuclear Physics, March 1-3, 2013, Sambalpur University, Orissa.

10. Entrance channel effect in the formation of ^{200}Pb, Rajni, Raj Kumar, **Deepika Jain** and Manoj K Sharma, DAE symposium on Nuclear Physics, Vol. **58**, 412, Dec. 2-6, 2013, BARC, Mumbai.

11. Role of spin-orbit interaction and Skyrme forces in Ni-induced reactions, **Deepika Jain**, Manoj K Sharma, Raj Kumar and Raj K. Gupta, DAE symposium on Nuclear Physics, Vol. **58**, 416, Dec. 2-6, 2013, BARC, Mumbai.
12. Entrance channel effect using stable and radioactive Sn-beams, Raj Kumar and **Deepika Jain**, X Latin American Symposium of Nuclear Physics and Application, Dec. 1-6, 2013, Montevideo, Uruguay.
13. Decay of radionuclide Californium, **Deepika Jain** and Manoj K. Sharma, Emerging Trends in Physics for Ionizing Radiations, Aerosols and Material Science, Dec. 13-14, 2013, Punjabi University, Patiala.

Contents

Abstract **1**

1 Introduction **7**
1.1 Nuclear reactions 9
1.2 Classification of heavy ion reactions 10
1.3 Different models for nucleus-nucleus interaction potential 13
1.4 Deformation and orientation 18
1.5 The model 21
1.6 Organization of the Thesis 23

Bibliography **26**

2 Methodology **33**
2.1 Introduction 33
2.2 The Dynamical Cluster-decay Model for hot and rotating compound systems 35
2.2.1 The Coulomb potential 42
2.2.2 Rotational Energy due to angular momentum 43
2.2.3 The Proximity Potential for deformed, oriented nuclei 43
2.2.4 Skyrme Energy Density Formalism in semiclassical extended Thomas Fermi approach 47
2.3 Wong Formula and its extension to include explicit summation of ℓ effects 52
2.3.1 Wong formula 52
2.3.2 Extended Wong Model 55

Bibliography **56**

3 Use of various Skyrme forces in fusion- fission dynamics **63**
3.1 Introduction: 63
3.2 Calculations and discussion of the results 66
3.2.1 Decay of ^{196}Pt* using the DCM 67
3.2.2 Fusion cross-sections for ^{196}Pt* using ℓ-summed extended-Wong model 73

3.3 Conclusions 74

Bibliography **76**

4 Isotopic analysis of Pt* nuclei formed using stable and radioactive Sn beams **79**

4.1 Introduction 79

4.2 Calculations and Results 82

4.2.1 Decay of Pt^* formed using stable and radioactive Sn-beams using DCM 85

4.2.2 Fusion cross-sections for ^{190}Pt* using ℓ-summed extended-Wong model 93

4.2.3 Fusion hindrance in Sn-induced reactions 96

4.3 Conclusions 97

Bibliography **98**

5 Comparative analysis of proximity potentials with deformation effects included **101**

5.1 Introduction 101

5.2 Calculations and Results 104

5.2.1 Effect of deformation and orientations on barrier characteristics 105

5.2.2 Application of various deformed proximity interactions in the calculations of fusion cross-sections 109

5.3 Conclusions 116

Bibliography **117**

6 Dynamics of hot Yb* isotopes formed via different reaction channels **122**

6.1 Introduction 122

6.2 Role of spin saturated and unsaturated interactions in O- and Ni-based reactions 123

6.2.1 Spin-orbit interaction potentials for spherical and deformed choices of nuclei 125

6.2.2 Fusion cross-sections for $^{156-168}$Yb* using different Skyrme forces with in framework of ℓ-summed Wong model 130

6.3 Entrance channel effect in decay of ^{172}Yb* formed using stable and radioactive beams 135

6.4 Conclusions 139

Bibliography **142**

7 Summary and outlook **145**

List of Tables

3.1 The ER and fission cross-sections for ^{196}Pt* system, calculated on the DCM at different $E_{c.m.}$'s for various Skyrme forces, compared with the experimental data [1]. The upper-limit of ER cross-section at $E_{c.m.}$=142.5 MeV, included in Fig. 3.8, is not included here. The quasi-fission (qf) contribution in fission is also calculated, wherever required. 70

4.1 The ER cross-sections and relevant variables for ^{188,190,191,192}Pt* system formed via ^{132}Sn+^{58}Ni and ^{124,126127,128}Sn+^{64}Ni, calculated with the DCM at different $E_{c.m.}$'s for level density parameter a=A/9, compared with the experimental data [14]. 83

5.1 Fusion barrier heights V_B and positions R_B with inclusion of deformation up to β_2 and "optimum" orientations [3] for the use of different proximity potentials for 52 asymmetric systems in increasing order of Z_PZ_T. 108
5.2 Same as Table 5.1 but for Bass 80 and Denisov DP along with empirical values. 110

6.1 The contribution of spin-orbit density dependent part V_J in nuclear interaction potential V_N for various isotopes of Yb* formed from O+Sm reactions, with inclusion of deformation and optimum orientation, using ETF in SEDF approach. 129
6.2 Fusion cross-section and the maximum value of angular momentum (ℓ_{max}) used for different Ni-induced reactions with ^{100}Mo, at $E_{c.m.}$ above and below the Coulomb barrier, using Skyrme force GSkI. Note, ℓ_{max} for ^{160}Yb* and ^{164}Yb* are the empirically fitted values. 134

6.3 The ER cross section and relevant variables for ^{124}Sn+^{48}Ca and ^{132}Sn+^{40}Ca, forming the same compound system $^{172}Yb^{*}$ are calculated using DCM at different excitation energies. The experimental data from Ref. [17] is also listed. The predicted ER cross-section for ^{132}Sn+^{40}Ca are also tabulated for above barrier energies. The barrier modification ΔV_B is for $1n$ channel at ℓ=ℓ_{max}. 140

List of Figures

1.1 The sketch of damped reaction stage (I-IV) leading to the formation of fission-like fragments, which compete in the way to complete fusion (V) of the initial projectile P and target T nuclei. 12

1.2 Schematic diagrams for deformed nuclei ((a),(b) oblate and (c),(d) prolate only) with corresponding optimum orientations along collision axis for "cold, elongated"((a), (d)) or "hot, compact"((b), (c)) configurations, from Table 1 [63]. 20

2.1 The geometry of the classical hydrodynamical model of Kröger and Scheid for calculating the mass parameter $B_{\eta\eta}$. 37

2.2 The scattering potential for ^{196}Pt*→^{195}Pt+n at fixed temperature T=1.5 MeV using SIII and GSkI forces. The barrier penetration points and barrier lowering parameter defined as $\Delta\ V_B$=$V(R_a)$-V_B is also shown for both the forces at their respective ℓ_{max} value. 39

2.3 Schematic configurations of two axially symmetric deformed, oriented nuclei, lying in the same plane and for various θ_1 and θ_2 values in the range 0^0 to 180^0. 40

2.4 Interaction potentials calculated for ^{48}Ca+^{96}Zr reaction at T=0 MeV using various version of nuclear proximity potentials at optimum orientations $\theta_1^{opt.}$=0^0 and $\theta_2^{opt.}$=90^0. 47

2.5 The half-density radius R_0 and the surface thickness a in fm, plotted as a function of mass number A of nuclei, each fitted to a polynomial in A. The data are from [69, 70]. 51

3.1 (a) Fragmentation potential $V(A_2)$ for the decay of compound nucleus ^{196}Pt*, plotted at $\ell = 0$ and ℓ_{max} values, using different Skyrme forces and compared with Blocki *et al.* interaction from [5]. (b) Same as for (a) but for the compound nucleus ^{176}Pt*. 67

3.2 Preformation probability P_0 as a function of fragment mass A_i corresponding to the fragmentation potential in Fig. 3.1(a). 68

3.3 The neck-length parameter ΔR plotted as a function of $E_{c.m.}$ for (a) ER, (b) fission, and (c) qf process, using the Skyrme forces SSk (solid line with hollow circle), GSkI (solid line with rectangle) and SIII (solid line with hollow triangle). 69
3.4 Comparison of experimental evaporation residue σ_{ER} and fission cross-section σ_{fiss} for ^{132}Sn+^{64}Ni reaction [1] with calculations made in DCM, using the three Skyrme forces (a) GSkI, (b) SSk, and (c) SIII. 71
3.5 Barrier-lowering parameter ΔV_B as a function of $E_{c.m.}$ for mass one particle at $\ell = \ell_{max}$ for SSk, GSkI, and SIII Skyrme forces. 72
3.6 Interaction potentials $V(R)$ of ^{132}Sn+^{64}Ni for the three Skyrme forces and Blocki *et al.* potential at fixed $E_{c.m.}$ and θ_i values for co-planar nuclei (Φ=0^0). 72
3.7 Barrier height V_B as a function of $E_{c.m.}$ for ^{132}Sn+^{64}Ni, using the three Skyrme forces SIII (solid line), GSkI (dashed line) and SSk (dotted line), and the Blocki *et al.* (dashed-dot line) potential at fixed θ_i values for co-planar nuclei (Φ=0^0). 74
3.8 (a) Fusion excitation functions of ^{132}Sn+^{64}Ni$\rightarrow$^{196}Pt* using the extended-Wong model, and (b) deduced ℓ_{max} values *vs.* $E_{c.m.}$, using the Skyrme forces SIII (dotted line), GSkI (solid line) and SSk (dashed line). 75

4.1 Fragmentation potentials V(A$_2$) for the decay of ^{190}Pt* formed in ^{132}Sn+^{58}Ni and ^{126}Sn+^{64}Ni reaction channel at comparable $E_{c.m.}$ values using (a) spherical and (b) deformation considered. 81
4.2 Preformation probability P_0 as a function of fragment mass A_i for the decay of ^{190}Pt* formed in ^{132}Sn+^{58}Ni and ^{126}Sn+^{64}Ni reaction channels at approximately same $E_{c.m.}$ values for level density parameters a=A/9 using (a) spherical and (b) deformation considered. 82
4.3 The ℓ-summed P_0, P and cross-section (σ) for the decay of $^{190}Pt^*$ as a function of light fragment mass A_2 at approximately similar $E_{c.m.}$ for (a) ^{132}Sn+^{58}Ni and (b) ^{126}Sn+^{64}Ni reactions. 86
4.4 Comparison of experimental evaporation residue σ_{ER} for the decay of CN $^{190}Pt^*$ formed in ^{132}Sn+^{58}Ni and ^{126}Sn+^{64}Ni reactions, with calculations made in the DCM. 86
4.5 Fragmentation potentials V(A$_2$) for the decay of ^{190}Pt* formed in ^{132}Sn+^{58}Ni reaction channel at a given $E_{c.m.}$. using different proximity potentials considered. 87

4.6 Total interaction potentials V(R) of ^{132}Sn+^{58}Ni for (a) the proximity potentials Prox 1977, Prox 1988, mod-Prox 1988 and Denisov 2002 and (b) level density parameters A/8, A/9 and A/10 for the case of Prox 1977, at $E_{c.m.}$=188.72 MeV for ℓ=0 case. 88
4.7 Same as Fig. 4.1 but for (a) Proximity 1988, (b) mod-Prox 1988 and (c) Denisov 2002. 89
4.8 Same as Fig. 4.2 but for level density (a) A/8 and (b) A/10. 90
4.9 Fragmentation potential V(A_2) for the decay of $^{188,190,191,192,196}Pt^*$ nuclei, plotted for ℓ=0$\hbar$ (below)and ℓ_{max} (above) values. 91
4.10 Barrier-lowering parameter ΔV_B as a function of $E_{c.m.}$ for the decay of $^{190,191,192,196}Pt^*$ nuclei at ℓ=ℓ_{max}. Inset shows the barrier modification for the reaction of ^{132}Sn with ^{58,64}Ni targets. 92
4.11 Barrier height V_B as a function of $E_{c.m.}$ for ^{132}Sn+^{58}Ni, using illustrated proximity potentials. 94
4.12 (a) Fusion excitation functions of ^{132}Sn+^{58}Ni$\rightarrow$^{190}Pt* using the extended- Wong model, and (b) deduced ℓ_{max} values *vs.* $E_{c.m.}$, using four proximity potentials i.e. Prox 77, Prox 88, mod-Prox 88 and Denisov 2002. 95

5.1 The nuclear interaction potential is shown in (a) to (e) and corresponding total interaction potential in (f) to (j) using Prox 77, Prox 88, Prox 00, Bass 80 and Denisov DP, for ^{48}Ca+^{96}Zr reaction as a function of internuclear distance R (fm) at T=0 MeV for both deformed and spherical choice of nuclei. 105
5.2 (a) Nuclear interaction potential and (b) total interaction potential for ^{48}Ca+^{96}Zr system at different θ_2 values keeping $\theta_1 = 0^0$ fixed at T=0 MeV. 106
5.3 The percentage deviation of barrier height as a function of the product of charges Z_1Z_2 using different versions of the proximity potential, taking deformations up to β_2 at “optimum” orientations [3]. 107
5.4 Comparison of fusion cross-sections calculated using various nuclear proximity potentials with in the Wong formula, integrated over θ_i, and the experimental data for (a) ^{16}O+^{92}Zr [25] (b) ^{16}O+^{112}Sn [29] (c) ^{16}O+^{186}W [22] (d) ^{48}Ca+^{96}Zr [38] (e) ^{48}Ca+^{154}Sm [42] reactions, as a function of $E_{c.m.}$. The upward arrow point out the Coulomb barrier of the reaction. 112
5.5 Same as Fig. 5.4 except that this shows comparison for (a) ^{46}Ti+^{64}Ni [27] (b) ^{64}Ni+^{64}Ni [37] (c) ^{64}Ni+^{74}Ge [39] (d) ^{64}Ni+^{100}Mo [41] and (e) ^{132}Sn+^{64}Ni [43] reactions. 114

5.6 Cross section at each angle for ^{16}O+^{92}Zr, ^{48}Ca+^{96}Zr reaction using Prox 1977 and ^{46}Ti+^{64}Ni reaction using Prox 1988 at respective highest experimental $E_{c.m.}$ values. 115

6.1 The spin-orbit interaction potential $V_J(R)$ at T=0 for increasing neutrons in the projectile/target nucleus, starting from ^{56}Ni+^{100}Mo, using (a) spherical and (b) deformed nuclei, for SIII force. 125

6.2 The spin-orbit interaction potential $V_J(R)$ at T=0 for increasing neutrons in the target nucleus, starting from ^{16}O+^{140}Sm, using (a) spherical and (b) deformed nuclei, for SIII force. Note the difference in scale *w.r.t.* Fig. 6.1 126

6.3 Spin-orbit interaction barrier height V_{JB} as a function of the mass number of the projectile nucleus, as the target remains fixed, using semiclassical approach with three forces SIII, GSkI and KDE0v1. . . 127

6.4 (a) and (b): the spin-orbit dependent interaction potentials $V_J(R)$; (c) and (d): the spin-orbit independent interaction potentials $V_P(R)$; and (e) and (f): the total nuclear interaction potentials $V_N(R) = V_P(R) + V_J(R)$, for isotopes of Yb* formed from ^{16}O+^{140,142,144,146,148,150,152,154,156}Sm, for deformed and oriented nuclei, at T=0 and 2 MeV, using Skyrme force SIII. 129

6.5 Spin-orbit interaction barriers V_{JB} for ^{16}O+^{148}Sm reaction at different θ_2 values, keeping $\theta_1 = 0^0$ fixed, for the three Skyrme forces SIII, GSkI and KDE0v1 at T=0 MeV. 130

6.6 (a) Spin-orbit and (b) total interaction potential for ℓ=0 case of ^{60}Ni+^{100}Mo reaction at fixed orientations, using various Skyrme forces. 131

6.7 Fusion cross section as a function of $E_{c.m.}$, calculated by using the ℓ-summed Wong model, integrated over θ_i, for Skyrme forces SIII, GSkI and KDE0v1, and compared with experimental data for (a) ^{60}Ni+^{100}Mo, and (b) ^{64}Ni+^{100}Mo systems. 132

6.8 Same as Fig. 6.7, but for (a) ^{16}O+^{144}Sm, and (b) ^{16}O+^{148}Sm systems. 133

6.9 Variation of fusion cross-section with increasing neutron number of CN Yb*, formed from Ni+Mo reactions, using the GSkI force, at above- and below-barrier energies. 133

6.10 (a) Fragmentation potential $V(A_2)$ for the decay of ^{172}Yb*, formed in two different entrance channels ^{124}Sn+^{48}Ca and ^{132}Sn+^{40}Ca are compared at comparable center of mass energy for deformed choice of nuclei at extreme ℓ-values using proximity formula. (b) Same as part (a) but for preformation probability. 136

6.11 (a) Experimental ER cross section [17] is compared with the one calculated using DCM for the decay of ^{172}Yb*, formed in two different entrance channels ^{124}Sn+^{48}Ca and ^{132}Sn+^{40}Ca at comparable $E_{c.m.}$. (b) Neck-length parameter ΔR for the two reaction as in part (a). The deduced maximum value of angular momentum at different energies for two reactions is shown in the inset. (c) Same as part (b) but for deduced values of barrier modification ΔV_B at ℓ_{max}. 137

Abstract

The work presented in this thesis deals with the formation and decay of variety of nuclear systems formed in heavy ion reactions using ℓ-summed Wong formula and dynamical cluster decay model (DCM) respectively. The study is done using two types of nuclear interaction potentials; one is obtained from proximity theorem and other via Skyrme Energy Density Formalism (SEDF). A non-statistical model DCM is based on collective clusterization approach and is used to account for the decay of hot and rotating nuclei formed in low energy heavy ion collisions. The main advantage of DCM over other statistical model is that it contains the structural information of the decaying nucleus via the relative preformation probability of the decaying fragments, before penetrating the interaction barrier. It is relevant to mention here that the temperature, angular momentum, deformations and orientation effects of the reaction partners and decaying products are dully incorporated respectively in Wong and DCM approach. The thesis comprises of seven chapters, a brief account of which is discussed below.

Chapter 1, presents the general introduction of the present work which includes the status of the experimental and theoretical developments to understand the dynamics of fusion-fission and associated nuclear structure effects. To study the formation and decay of nuclear systems, the precise and systematic understanding of various nucleus-nucleus interaction potentials is essential, a brief account of such interactions is summarized in this chapter. Beside this, the role of angular momentum, entrance channels, deformations and orientations, fusion hindrance etc. have been discussed.

Chapter 2 gives the details of the methodology used, the dynamical cluster-decay model (DCM) based on the Quantum Mechanical Fragmentation Theory ($QMFT$) for binary fragmentation, which find its basis in the collective mass transfer process. The process of binary decay like neutron evaporation, α-decay, cluster

decay, fission fragments etc is treated in two steps: In first step the quantum mechanical preformation probability of the cluster in the mother nucleus is evaluated and the second step accounts for the penetration of the cluster through the interaction barrier. In this model the preformation probability of all possible clusters within the mother nucleus is calculated by solving stationary Schrodinger equation in mass asymmetry (η) coordinate. The role of temperature dependence of the proximity potential, Coulomb interaction potential, rotational energy and binding energies is briefly discussed. Details of the Skyrme energy density formalism (SEDF), used to calculate the interaction potential between the two colliding nuclei is also described. Finally the Wong's formula and its extended version are also described in brief.

In **Chapter 3**, the dependence of fusion-fission process on Skyrme forces is analyzed by using the dynamical cluster-decay model (DCM) and the ℓ-summed extended-Wong model. An extensive study on ^{132}Sn+^{64}Ni$\rightarrow$^{196}Pt* reaction is carried out, where the nuclear proximity potential is obtained by using the semiclassical extended Thomas Fermi (ETF) approach in Skyrme Energy Density Formalism (SEDF) under Frozen density approximation. The DCM gives an excellent fit to the measured fusion-evaporation residue (ER) and the fission cross-sections at below and above-barrier energies, with ER data needing "barrier lowering" at below-barrier energies for each Skyrme force, an in built property of DCM, and the fission cross-sections show a contribution of quasi-fission (qf) at the above-barrier two/ three highest energies, depending on the type of Skyrme force. Calculations are illustrated for three Skyrme forces GSkI, SSk and SIII. Another interesting result is that there is a change of fission mass distribution from a predominantly asymmetric to symmetric one with decrease in the N/Z ratio of compound nucleus, independent of the choice of nuclear interaction potential, which gives an opportunity to address the isospin effects in Pt* nucleus. Within ℓ-summed extended-Wong model we observe that the GSkI and SSk forces fit the total fusion cross-section data almost exactly, whereas SIII force needs "barrier modification" in order to fit the data at below-barrier energies. This happens because the isospin and neutron-proton asymmetry nature of GSkI and SSk forces is different from that of the SIII force, and that the center-of-mass energy $E_{c,m,}$ dependence of the barrier height for SIII (and Blocki *et al.*) force differs strongly (by a constant amount of $\sim$7 MeV) as compared to those for GSKI and SSk forces. In this chapter, the role of deformations and orientations is investigated by employing a variety of Skyrme forces such as SIII, GSkI and SSK within energy density formalism (EDF) approach. Beside this the fusion probability is estimated using ℓ-summed Wong formula (or equivalently Hill-Wheeler method) and exclusive role of above mentioned Skyrme forces is dully addresed.

In **Chapter 4**, we have studied the role of deformations and orientations by using different proximity potentials to analyse the persistence of entrance channel effect in the decay of ^{190}Pt* compound nucleus formed by using ^{132}Sn+^{58}Ni and ^{126}Sn+^{64}Ni reactions. The inclusion of deformations significantly effects the fragmentation profile of ^{190}Pt* compound nucleus with in the framework of DCM. Moreover, the decay pattern of Pt* nuclei formed using stable ^{124}Sn beam is also investigated. For both entrance channels i.e. ^{132}Sn+^{58}Ni and ^{126}Sn+^{64}Ni, the fragmentation potential and preformation probability of decaying fragments is almost identical at comparable center-of-mass energies ($E_{c.m.}$), suggesting that the decay of $^{190}Pt^{*}$ is perhaps independent of it's formation effects. In order to check for the persistence of entrance channel independence in the decay of Pt^{*} compound nucleus, various versions of nuclear proximity potentials and different values of level density parameter are employed in the calculations and the signature of entrance channel independence seem to sustain throughout. It is also observed that with inclusion of deformation effects up to quadrupole (β_2) with in the optimum orientation approach, the structure of potential energy surfaces changes significantly. The ^{132}Sn+^{58}Ni reaction is also studied using four proximity potentials i.e. Prox 1977, Prox 1988, mod-Prox 1988 and Denisov 2002 with in the framework of ℓ-summed extended-Wong model for addressing the fusion hindrance phenomena. We find that Prox 77 and Prox 88 fit the total fusion cross-section data only at above barrier energies whereas Denisov 2002 underestimate the data at all energies due to its least sensitiveness towards asymmetry and isospin. So a stronger nuclear interaction potential mod-Prox 1988 that accounts for isospin effect and asymmetry of the colliding nuclei is employed, which fits the data with smooth variation of $\ell_{max}(E_{c.m.})$. Our calculations indicate that the isospin and asymmetry of colliding nuclei also play an important role in the fusion dynamics particularly at below barrier region.

In previous chapters, the decay patterns of Pt* compound nuclei formed using radioactive and stable beams are analysed, by employing various nuclear interaction potentials calculated using EDF as well as available nuclear proximity potentials. In **Chapter 5**, the effect of deformation and orientation on barrier height and barrier position is studied using different types of proximity potentials for some 52 colliding nuclei with mass asymmetry parameter in range of 0 to 0.96. Various proximity potentials like Prox 77, Prox 88, Prox 00, Bass 80 and Denisov DP are used to extract barrier characteristics. These potentials cover a wide range of barrier and have different isospin and asymmetry dependence. With the inclusion of deformations, the barrier height and barrier position gets modified along with a significant change in the curvature of interaction potential. In order to study the possible effect of these deformation and orientation dependent proximity potentials, an effort is made in the framework of Wong formula to address O-, Ca- and Ni- based reactions in medium mass region in reference to available data on fusion cross-sections across the Coulomb barrier. For ^{16}O- and ^{48}Ca-based reactions, Prox 77 gives better comparison with experimental data as compared to other potentials around the Coulomb barrier energies whereas for ^{64}Ni-based reactions Prox 88 seems a better option. At energies above the Coulomb barrier Bass 80 and Denisov DP compete with each other. The angular dependence of cross-section is also studied. In summary, it is observed that deformation and orientation degree of freedom play a significant role in reaction dynamics of chosen set of heavy ion reactions.

Upto now, the role of nuclear shape of colliding and decaying fragments is addresses using proximity pocket formulas as well as the EDF based Skyrme approach. Although the barrier profile calculated using proximity and EDF based nuclear interaction looks similar, but the latter approach seem to have merit over the earlier one. The main advantage of using the Skyrme approach is that the hamiltonian used in microscopic EDF approach consists of two terms namely: spin-orbit dependent and spin-orbit independent interaction potentials, which otherwise is not possible while using phenomenological models i.e. proximity potentials. Hence, in **Chapter 6**, a systematic study of the spin-orbit density dependent interaction potential is carried out, with spherical as well as deformed choices of nuclei, for a variety of near-symmetric and asymmetric colliding nuclei leading to various isotopes of compound nucleus Yb*, using the semiclassical extended-Thomas Fermi formulation (ETF) of the Skyrme energy density formalism (SEDF). We observe that the spin-orbit density interaction barrier-height (V_{JB}) and barrier-position (R_{JB}) increase systematically with increase in number of neutrons in either the projectile or target, for spherical systems. On allowing deformation effects with optimum orientations, the barrier-height increases systematically with enhanced magnitude as compared to the spherical case, in going from ^{156}Yb* to ^{172}Yb* nuclear systems formed via near-symmetric Ni+Mo or asymmetric O+Sm colliding nuclei, except that for the oblate-shaped nuclei, the barrier height and barrier distribution does not follow the usual trend. The temperature does not change the behavior of spin-orbit density dependent (V_J) and independent (V_P) interaction potentials, except for some minor modifications in the magnitude. The orientation degree of freedom also plays an important role in modifying the barrier characteristics and hence produce a large effect on the fusion cross section. The fusion excitation function of compound nuclei ^{160,164}Yb* formed in different incoming channels, seem to suggest that the new forces GSkI and KDE0v1 respond better than the old SIII force. The fusion cross-sections are also predicted for few other isotopes of Yb*. Beside this, the decay pattern of hot and rotating ^{172}Yb* compound nucleus, formed in two entrance channels ^{124}Sn+^{48}Ca and ^{132}Sn+^{40}Ca, is studied using the dynamical cluster-decay model.

Finally, in **chapter 7**, the summary and significance of the work of this thesis and the scope for possible extension of present work is discussed.

Chapter 1

Introduction

All the matter of the universe is made up of tiny particles called atom. The concept of atom was introduced in the fifth century BC by the Greek philosophers Leucipps and Democritos. Prior to them it was believed that matter could be divided into smaller and smaller constituents indefinitely. However, the concept of atom remained purely speculative until the beginning of nineteenth century AD. The British physicist, J. J. Thomson discovered the negatively charged electron. Later the positively charged proton was discovered and consequently it was established that atom is a neutral particle. Following this Thomson [1] gave a plum pudding model in which the atom consisted of a uniformly charged sphere of proton throughout which were distributed an equal and opposite charge in the form of electrons. This model could account for the stability of atoms, but could not address the discrete wavelengths observed in the spectra of light emitted from excited atoms and provided disagreement with the pioneering Rutherford α-scattering experiment [2]. In 1932, Chadwick discovered the neutron and provided the path to address missing ingredient of nuclear matter. Even then there was a problem in classical physics that the electrons would be constantly accelerating and would therefore lose energy by radiation, leading to the collapse of the atom. This problem was solved by Bohr as he applied the newly emerging quantum theory, including relativistic effects described by the Dirac equation and Bohr structure of atom was conceived. Later, Heisenberg, another founder of the quantum theory, applied quantum mechanics to investigate the nucleus and the dynamics of neutrons and protons named as nucleons. In this case however, the force binding the nucleus is not the electromagnetic force that holds electrons in their orbits, but is a short range force whose magnitude is independent of the type of nucleon. This binding interaction is called the strong nuclear force. These ideas still form the essential framework of our understanding of the nucleus today, where nuclei are bound states of nucleons held together by a strong charge-independent short-range force. Near the end of nineteenth century, the discovery of natural radioactivity [3] had been discovered and led to contemplate the nature of nucleus. In 1919, Rutherford achieved the first artificial radioactivity [4]. The nuclear transmutation experiments of Rutherford, Cock-Croft and Walton, Curie and Juliet and Fermi suggested new experimental methods to solve basic problems regarding the nuclear structure, nuclear properties, nuclear forces, transition probabilities etc., which considerably motivated nuclear reaction studies [4]. Soon nuclear reactions were used as a tool to understand the properties of nuclear interactions in various physical conditions.

The investigation on nuclear reactions provide a way to explain the phenomena like fusion, fission, deep inelastic collision (DIC), quasi-fission (qf) etc. arising when the two nuclei collide each other and the forces under which they interact. The above processes generally depend on the excitation energy, impact parameter, angular momentum, atomic masses, charges of the nuclei etc. The ability to explain all the phenomena is complicated as the nuclear interaction is not fully understood, despite a considerable amount of effort spend in studying it. The number of particles of a self-bound nuclear system ranges from two nucleons in the deuteron to nearly three hundred in the super-heavy nuclei currently being studied [5–7]. Furthermore, neutron stars are thought to be made of nuclear matter, bound due to gravitational forces, and under more extreme physical conditions than ordinary nuclear matter, but presumably subject to the same interactions [8].

1.1 Nuclear reactions

The process in which two nuclei, or else a nucleus of an atom and a subatomic particle (proton, neutron), collide to produce one or more nuclides is known as a nuclear reaction. The nuclear reaction dynamics is usually classified into three categories on the basis of energy of incident projectile as low energy (E$\leq$ 15 MeV/nucleon), intermediate energy (15$<$ E$<$ 500 MeV/nucleon) and high energy (E$\geq$ 500 MeV/nucleon). In low energy reactions mean nuclear force field acting between the two nuclei dominate in comparison to high energy reactions where direct nucleon-nucleon interactions take place while in intermediate energy reactions both the aspects play their role. The heavy ion (HI) induced low energy nuclear reactions, is a topic of resurgence interest for nuclear physics community as it leads to better understanding of nuclear forces with formation of heavy nuclei away from valley of stability and subsequently providing the much needed nuclear structure information. Heavy ions are the nuclei equal to or heavier than the α-particle i.e. nuclei having atomic number greater than or equal to 2 and mass number greater than or equal to 4. Thus, α-particle can be called as the lightest heavy ion. In the beginning, the nuclear physics research was centered around the ground state properties of these nuclei as well as the reactions induced by lighter projectiles such as neutron, proton etc. The invention of new particle accelerators and the availability of heavy ion and radioactive ion beams provided many possibilities for exploring new aspects of nuclear physics. With the heavy ions, it became possible to produce reaction products with very high excitation energies. Using these heavy and radioactive ions with sufficient energy, it is possible to fuse two nuclei to form a single compound system with larger mass, charge and particle number than any of the stable nuclei; the idea inspired the community to search for the superheavy elements (SHEs). Synthesis of superheavy elements is a challenging topic, as it represents deep insight into the shell stabilization and structure effects. The existences of long-life SHEs were predicted theoretically in late 1960s and early 1980s [9,10]. The synthesizing and discovering new superheavy elements proves long-held nuclear theories regarding the existence of the island of stability and possibly the ultimate limits of the periodic table of the elements. These discoveries will also help to better understand, how nuclei are held together and how they resist the fission process. The main emphasis is to explore the borderline of the nuclear chart towards its upper end, where the strong Coulomb repulsive force is acting between the many protons.

1.2 Classification of heavy ion reactions

When two heavy ions approach each other, they experience a long range Coulomb repulsion and a short range attractive nuclear force. The competition between the two forces define a barrier with an energy pocket inside it. Since these heavy ions carry angular momentum, a repulsive centrifugal force is also present, the effect of which is to increase the barrier height and decrease the depth of the energy pocket. Therefore, a certain amount of projectile energy is required to initiate a heavy ion reaction. Depending upon various quantities such as energy, angular momentum, mass etc, heavy ion collisions display a variety of phenomena i.e. compound nucleus (CN) and non-compound nucleus (nCN) processes. The CN process leads to fusion-fission (FF), evaporation residue (ER) or equivalently light particles LPs, intermediate mass fragment (IMF) and heavy mass fragment (HMF). On the other hand nCN processes proceed via deep inelastic collision (DIC), quasifission (qf), fast fission etc.

In complete fusion reaction, a composite system is expected to be formed after an intimate contact and transient amalgamation of projectile and target nucleus leading to the formation of fully equilibrated Compound nucleus. The CN can not be formed, if the entrance channel introduces more input angular momenta than the composite system can sustain. In this process, complete transfer of kinetic energy, mass and angular momentum takes place and the composite system completes several rotations during which it equilibrates in all degree of freedom [11]. It may, further, be pointed out that the kinetic energy of projectile in the center of mass frame is converted into the excitation energy of the CN. The compound system thus formed in a reaction are highly excited and carry large angular momentum. Such a hot, rapidly rotating system is not stable and decays to its ground state prior to its detection. The excitation energy at the formation is decided by the reaction Q-value and kinetic energy. After a relatively long period of nuclear time (typically from 10^{-19} to 10^{-15} second), CN loses its memory of how it was formed and independent of the properties of the reactants, it disintegrates, either in particle emission [12] or fission [11]. Particle emission, often called as evaporation, leave behind the evaporation residue (ER), an entity similar to the CN except for the evaporated particles.

In general the nuclear systems formed via heavy ion collisions, decay through the fission and ER channels depending on the mass of compound nucleus formed, type of target/projectile and energies involved. For light compound systems with $A_{CN} \sim$ 40-80, the fission yield is minimal and the light-particles (LPs) emission is always accompanied by intermediate mass fragments, the IMF. In this mass region the IMFs (with $2 < Z < 10$ and $5 \leq A \leq 20$) contribution is very small of the order of 5-10 percent, in comparison to LPs contribution. However, for the heavy nuclear systems $A_{CN} \sim 200$, the most probable decay mode of the CN is fission/ heavy mass fragments (HMFs), due to its instability against centrifugal repulsion, with small contribution from neutrons and γ-rays emission, just in contrast to decay process of light compound systems. Further increase in angular momentum, non-compound nucleus processes begin to dominate. It is not necessary that a composite system trapped inside the potential energy always evolve towards a CN. Experimentally it was observed that depending upon the energy, angular momentum, mass asymmetry of the entrance channel etc, the composite system can either equilibrate in all degree of freedom or re-separate before complete equilibration. These unequilibrated processes are normally known as non-compound nucleus processes and include DIC [13],

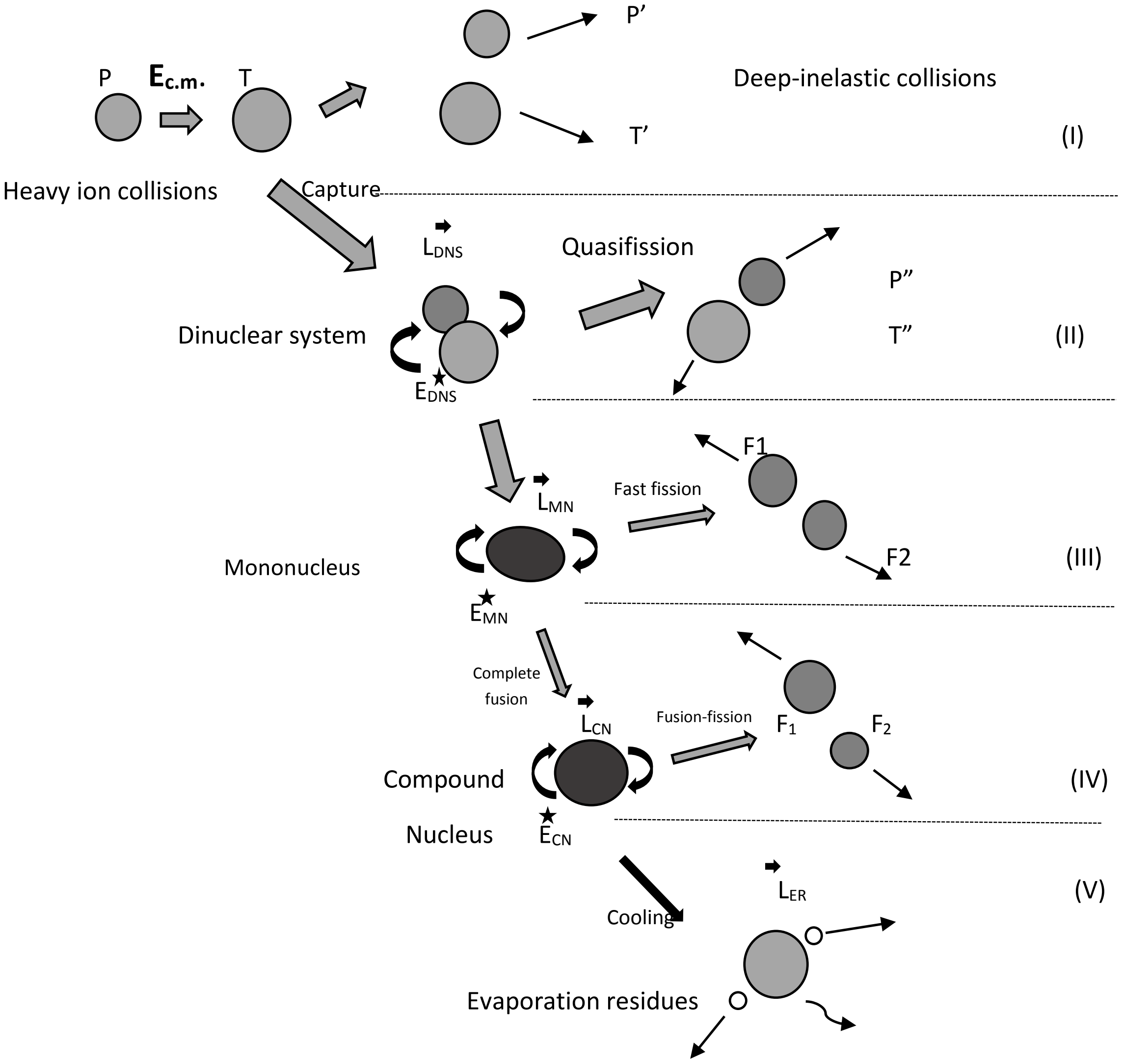

Figure 1.1: The sketch of damped reaction stage (I-IV) leading to the formation of fission-like fragments, which compete in the way to complete fusion (V) of the initial projectile P and target T nuclei.

qf [14–16], fast fission [14, 17, 18] etc. The sketch of all these CN and nCN processes is shown in Fig. 1.1. The first are deep-inelastic collisions and the second are capture reactions shown on top of Fig. 1.1. The difference between capture and DIC depends on whether a path of the relative motion has been trapped into well of the nucleus-nucleus interaction or not (see Fig. 2 of Ref. [19]). If there is not a potential well, only the DIC takes place. In the case of capture the full momentum trasfer takes place, while it does not occur in the DIC. Quassifission is a non-equilibrium process originating due to the compact saddle point configuration of the system compared to the compact configuration. Moreover, qf refers to a process where incoming nuclei in a reaction do not loose their identity and as a result decay into projectile and target like fragments. Fast fission is another non-equilibrium process that dominates at higher energies. This process occurs when the fission barrier vanishes as a result of large angular momentum. The potential trap also may vanish at such high angular momentum and the system will not get sufficient time to equilibrate before re-separation. Only fusion-fission carries the information about the shape of the saddle point, as it is traversed during the fission decay, whereas qf does not reach the shapes inside the saddle point. One more thing has been observed that when two interacting nuclei touch each other by their lateral surfaces (near-side collision) a high probability of CN is expected, whereas, a high qf probability is expected in the elongated configuration when nuclei touch each other by their poles (near-tip collision) [20–22].

1.3 Different models for nucleus-nucleus interaction potential

The nucleon-nucleon interaction is the key for the proper understanding of any nuclear phenomena. In nuclear reactions, emphasizes is laid on the interaction between incident particle and the target nucleus, since the nuclear decay processes are more sensitive to the total potential in the nuclear surface region. The total potential as a function of distance consists of the sum of the long range Coulomb repulsive force, centrifugal interaction and nuclear potential terms. The centrifugal and Coulomb part of the interaction potential are well known, however nuclear interaction part is not fully understood as yet. Further the Coulomb potential alone cannot define the barrier, so an appropriate choice of nuclear potential is extremely desirable to understand heavy ion reaction dynamics. From literature it is clear that no experiment can impart extract information about fusion barriers directly. All experiments measure fusion cross-sections [23] and then with the help of theoretical models, one can extract the fusion barriers. Theoretical models are helpful in understanding the nuclear interactions at a microscopic/macroscopic level. Thus for a better understanding of the world around us, the more accurate and microscopic methods for calculating the ion-ion interaction, between the colliding nuclei, should be exploited. Several forms of the complex short ranged attractive nuclear potential have been used in literature. The two commonly used approaches for calculating the ion-ion potentials are discussed in the following:

(i) Phenomenological models: These models use a simple analytical expression for calculating the nucleus-nucleus interaction known as proximity potential. These proximity potentials are the benchmark and backbone for majority of microscopic/macroscopic fusion models. All proximity potentials are based on the proximity force theorem, according to which the nuclear part of the interaction potential can be taken as the product of a factor depending on the mean curvature of the interaction surface and a universal function (depending on the separation distance) and is independent of the masses of colliding nuclei. This concept did introduce a great amount of simplification in nuclear potential studies [24, 25], and has been used extensively to understand nuclear reaction dynamics at low energies. Firstly, Bass [26,27] introduce a expression for interaction potential and after that Blocki [28] gave a simple formula as a function of separation between the surfaces of the two colliding nuclei, known as the pocket formula of proximity potential. With the passage of time, several improvement/modifications were made in the proximity potentials through surface energy coefficient or the universal function and/or nuclear radius to explain the experimental data. In literature there are more than 20 versions of the proximity potential [29–31] derived either from the proximity potential or from the parametrized versions in terms of the proximity concept. Some of these potentials have been fitted to the experimental fusion barrier height and have been very successful in describing scattering data.

(ii)Energy density formalism (EDF): In energy density formalism, the nucleus-nucleus interaction potential, as a function of separation distance, is defined as the difference of the energy expectation value of the colliding nuclei that are overlapping (at a finite separation distance R) and are completely separated (at $R=\infty$) [32, 33]. The Hartree-Fock (HF) method can be considered as the microscopic background to built up the EDF model. In 1927, D. R. Hartree introduced a self- consistence field method, to calculate approximate wave functions and energies for atoms and ions. This method with effective interaction allows one to caculate in region where realistic calculations become impractical and a least amount of numerical effort is required. It was first adopted by Vautherin and Brink [34] in order to study the ground state properties of spherical nuclei by using Skyrme interaction [35]. The full HF calculations were not possible in energy density formalism due to non availability of expressing the kinetic energy density (τ) of the compound nucleus at HF level. To overcome this difficulty, semiclassical approaches to this quantity based on the Thomas-Fermi (TF) method or its extensions (ETF) have been used for obtaining τ in the compound system.

The ETF approach of Grammaticos and Voros [36] starts from the semiclassical expansions based on the Wigner transformation and it was applied to the case of fermions governed by a one-body Hamiltonian. Expansions upto fourth order in $\hbar$ of the density matrix for various spin- independent potentials were considered to provide a more accurate description of the nuclear surface. With the aid of the semiclassical expression the total energy of the system becomes a functional of the nucleon density only. Firstly, no spin dependent term is considered in the calculations and it is however well known after the success of traditional Shell-Model, that the single-particle nuclear hamiltonian must incorporate a spin-orbit part in order to account for the observed nuclear properties correctly. Thus, in the later papers of Grammaticos and Voros [37], the spin orbit part is incorporated by extending their semiclassical expansions to the realistic case where the effective one-body Hamiltonian for nucleons contains spin-dependent terms. Consequently Gupta and collaborators [38–42], studied the role of the spin-orbit density part of the interaction potential in microscopic shell model formulation of Skyrme energy density formalism (SEDF) which is shown to be important, not only for its significant contribution to fusion cross sections, but also for the α-nucleus structure of colliding N=Z, α-nuclei and its suppression for colliding non-α nuclei. Moreover, in Ref. [43], it was also shown that both approaches (microscopic shell model and semiclassical formulation) can reproduce same shell effects if the results of semiclassical SEDF calculations are normalized with respect to (one or both) spin saturated nuclei.

Here, in this thesis we use energy density formalism given by Vautherin and Brink which uses the density dependent Skyrme interactions that consists of spin dependent and spin independent part with in semiclassical ETF approach [36, 37, 44, 45]. The Skyrme force is an effective interaction (depending upon a limited number of parameters) between nucleons in nucleus providing a zero-range potential as suggested by T.H.R Skyrme in 1950's. Initially, Standard Skyrme effective force (SSEF) [34,46] was used which contain only single density dependent term and spin-orbit term giving the value of the nuclear matter incompressibility coefficient k_∞ in the range of 300-400 MeV, which is higher than the experimental value of ∼220 MeV. In order to obtain a reasonable value of k_∞ and other several properties of the normal and isospin rich nuclei, the Generalized Skyrme effective force (GSEF) [47,48] came into picture. Generalization of the Skyrme effective force can be realized by adding several density-dependent terms to each of the three, namely, local, nonlocal and spin-orbit parts of the SSEF. There are 240 Skyrme interaction parameter sets in the literature, out of which only 16 are shown to satisfy the current understanding of the physics of nuclear matter over a wide range of applications [49]. These 16 forces are obtained by using GSEF Hamiltonian and satisfy various properties like binding energy, charge rms radii etc. mainly for spherical and or neutron rich nuclei. For neutron deficient nuclei, other forces having single spin-orbit term may play significant role in calculation of fusion cross-sections.

The interaction potential calculated by EDF are usually done under two extreme physical assumptions:

(a) The approximation under which the time of collision being so slow that at each stage of the collision the nucleons of the two ions reach the equilibrium configuration, called the 'adiabatic approximation'.

(b) The approximation under which the time of collision is so small that the internal structure of the two ions is unmodified and the nuclear density overlap without changing their shapes, called 'sudden density approximation' that includes the effect of exchange terms due to anti-symmetrization. The sudden density approximation excluding the effect of exchange terms is also known as frozen density approximation [50]. The exchange effects arise for a composite system because $\tau(\rho)$ and $\vec{J}(\rho)$ are expressed as functions of the ρ_i (i=1,2 for two nuclei), which, in turn, are the sums of their nucleon densities (ρ_i=ρ_{in}+ρ_{ip}), with ρ=ρ_1+ρ_2. On the other hand, in frozen density, the composite nucleus densities are simply the sums of the densities of two incoming nuclei. Recently, authors of [51] study the effects of adding the densities in sudden and frozen approximation on the interaction potentials for medium mass and superheavy mass region reactions, and showed that the barriers obtained for the frozen densities approximation, are more realistic as compared to that for sudden approximation. Following this systematic, we prefer to follow frozen density approximation in this work.

Since the semiclassical ETF approach allows us to expresses the kinetic energy density $\tau(\vec{r})$ and spin-orbit density $J(\vec{r})$ as functions of nucleon density $\rho(\vec{r})$ and its derivatives, used in self-consistent variational approach with nucleon densities as the variational quantities, the Skyrme energy density becomes a functional of the nucleon densities alone, and hence eliminates completely the use of single particle wave functions. The (variational) nucleon densities are taken as the the modified (two-parameter) Fermi density with an additional parameter [44, 45, 52, 53]. The kinetic energy density $\tau(\vec{r})$ and spin-orbit density $J(\vec{r})$ are taken up to second order. Although the higher order contributions [37,44,45] to both $\tau(\vec{r})$ and $\vec{J}(\vec{r})$ are available in the semiclassical approach at the ETF level, however second order terms are enough for the numerical convergence [45]. Here, we use the surface diffuseness and nuclear radii, the two parameters of Fermi-density, obtained from a polynomial fit to the experimental data [54,55].

The role of different proximity potentials are same as that of using various Skyrme forces in SEDF approach. By using both types of nucleus-nucleus interaction potential, fusion hindrance phenomena [56,57] can be handled. Fusion hindrance has become a hot topic of research in nuclear physics in which there is a steep fall of fusion cross sections at energies below the barrier. This can be tackled by modifying the shape of the potential inside the barrier at sub-barrier energies by employing suitable nuclear interaction.

1.4 Deformation and orientation

One of the nuclear properties for which the nuclear interaction is responsible is the nuclear shape. Actually, we do not know if some of the nuclei are really deformed since the optical instruments available today don't allow us to see the nucleus. But there are many indirect observations which lead us to this conclusion. If we consider the nucleus isotropic and rotating, we will see no change if it is spherical. If it is deformed then we will see some rotational characteristics, e.g. specific γ-rays emitted when the nucleus decays. We can also see the deformation from the distribution of the charge in the nucleus which will tell us how the nucleons are distributed inside the nucleus and gives a hint of deformation. Nuclei may have extreme shapes, the higher multi-pole deformations, β_λ(λ= 2, 3, 4) or extreme neutron-to-proton ratios where the term β is a measure of how much the scissioning nucleus deviates from the spherical shape. In general, elongated (prolate) and flattened (oblate) are most commonly observed deformed nuclear shapes. Higher order deformations, such as octupole (β_3) and hexadecapole (β_4) are also possible, as are triaxial deformations and other more exotic shapes. The contribution of these higher multipole deformations along with the choice of appropriate orientations lead to enormous exotic shapes which in turn are immensely useful to understand various aspects of nuclear structure and dynamics at extreme conditions therby providing important information for future experiments. Experiments can create such nuclei, using artificially induced fusion or nucleon transfer reactions, employing ion beams from an accelerator. With the advent of new generation of accelerators, which are capable of accelerating not only heavy ions but also radioactive ion beams (RIB) to produce exotic nuclei, vast amount of experimental data is being accumulated, from lighter nuclei to some super heavy ones. Collisions between the deformed, oriented nuclei have been investigated in early 1980s and Greiner [58] suggested that oriented ^{238}U+^{238}U collisions could lead to a very long lived (life-time $\sim 10^{-20}$ second) giant molecule. Many calculations were made [59]- [61] and all showing that the barrier is lowered due to deformations and orientations of the colliding nuclei. It is lowest for the 0^0, 180^0 orientations of two ^{238}U nuclei. This gives pole-to-pole or nose-to-nose configuration. As ^{238}U is a prolate deformed nucleus and hence the barrier height is studied only for prolate-prolate collisions. Experimentally, the compound nucleus production cross-sections were shown to be very sensitive to the choice of reaction partners. Even for the same compound nucleus, different target-projectile combinations give different fusion cross-sections and may also lead to different physical processes.

It is well known that the fusion probability of heavy nuclei decreases rapidly with the increase of charge number of target and projectile [62]. Even if the kinetic energy of the projectile is large enough to overcome the fusion barrier, compound nucleus is not always formed. But during this process, a large amount of kinetic energy may be lost. This situation may be different for deformed and oriented nuclei, because the distance between the two colliding nuclei at the touching point depends on the orientation of deformed nuclei. This suggests that the fusion process is affected by

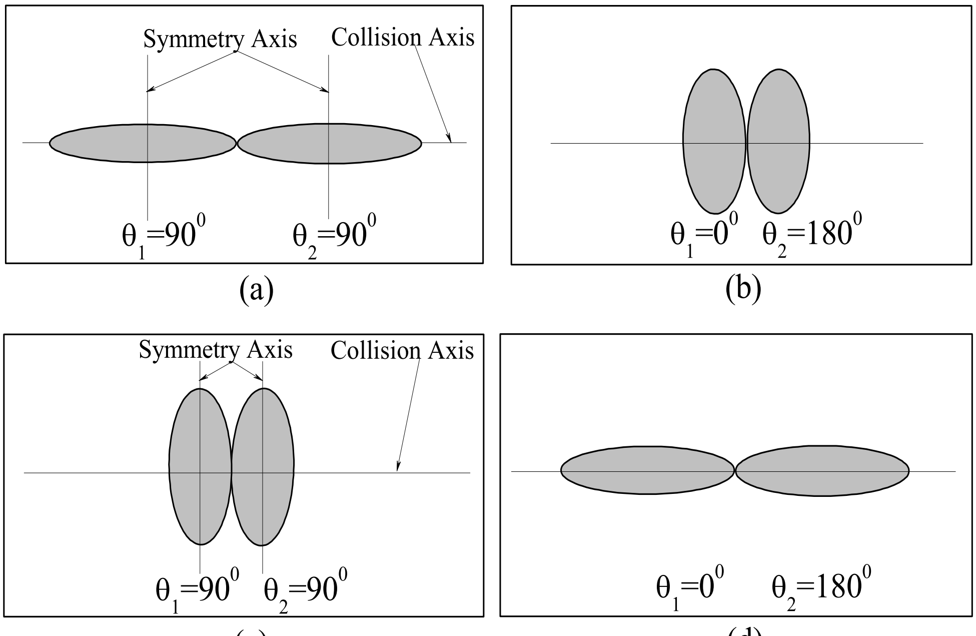

(a) (b)

(c) (d)

Figure 1.2: Schematic diagrams for deformed nuclei ((a),(b) oblate and (c),(d) prolate only) with corresponding optimum orientations along collision axis for “cold, elongated”((a), (d)) or “hot, compact”((b), (c)) configurations, from Table 1 [63].

the colliding angle (i.e. angle between the symmetric axis of nucleus and the collision Z-axis). A detailed study [63] based on Quantum Mechanical Fragmentation Theory (QMFT) shows that the interaction barrier (height as well as position) is greatly affected by deformed and oriented colliding nuclei. This study shows that each pair of quadrupole deformed nuclei results in a lower barrier or, alternatively, a most compact configuration for only some specific orientations. In other words, for coplanar nuclei, the orientations are optimized (uniquely fixed) for each pair of quadrupole deformed (prolate or oblate) or quadrupole deformed + spherical colliding nuclei leading to cold or hot fusion configurations. The optimum orientations are given for cold, non-compact fusion configuration corresponds to largest interaction radius but the lowest barrier whereas for hot, compact fusion configuration gives the highest barrier / smallest interaction radius. A schematic diagram is illustrated in Fig. 1.2, only for prolate-prolate and oblate-oblate deformed colliding nuclei along collision axis for both cold, elongated and hot, compact configurations. Therefore, in order to have meaningful predictions of formation and decay paths of nuclear reactions, it is important to investigate the effective role of deformation and orientations in the calculation of effective nuclear interaction.

1.5 The model

Normally, in heavy ion collisions, the compound nucleus formed has high excitation energy and carries large angular momentum. In order to study the decay of a hot and rotating compound system, we have used the Dynamical Cluster-decay Model (DCM) [64–66] adopted from Preformed Cluster Model (PCM) [67, 68] which finds its basis in QMFT [69]. The statistical model i.e. Hauser Feshbech [70, 71] analysis which is best to understood the emission of multiple LP's and the Fission models [72] easily explain the IMFs production separately whereas DCM has the advantage that it can be applied to all possible decay process like ER, Fusion-fission, qf etc. Another advantage of DCM over other statistical model is that it contains the structural information of the decaying nucleus via the preformation of the fragments with relative probabilities, before penetrating the interaction barrier. The DCM has the in-built characteristics of barrier modification through the only parameter of the model, the neck length parameter, which is related to the total kinetic energy TKE(T) or effective Q-value at temperature T of the hot CN, defined in terms of the CN binding energy and ground state binding energies of the emitted fragments. The DCM is applied for both negative as well for positive Q-value systems, with complete angular momentum and charge dispersion effects. It may be relevant to mention here that the nucleus-nucleus potential used in DCM calculations are either through the proximity potentials with temperature effects included through the nuclear radii [73] and surface width [74] or with semiclassical ETF approach of SEDF, where temperature dependence is taken from Ref. [75]. Beside the temperature and angular momentum effects in the above mentioned dynamical cluster-decay model, the deformations and orientation effects of the reaction partners and decaying products are also taken care of. We have also used Wong formula [76] for calculation of fusion reaction cross sections which is a special case of the DCM with preformation probability P_0=1. A point of difference in the two models (Wong and DCM) is that the penetrability P_ℓ in Wong formula is calculated in Hill-Wheeler [77] approximation of inverted harmonic oscillator for the interaction potential $V_\ell(R)$ of the incoming channel, whereas the same in DCM is based on Wentzel-Kramers-Brillouin (WKB) approximation.

In this thesis, following problems are studied:

- The recent data on decay of the compound systems ^{196}Pt* at below and above barrier energies is addressed using DCM, by employing nucleus-nucleus interaction potential obtained from the semiclassical ETF approach in SEDF under frozen density approximation.
- Fusion hindrance, Entrance channel and Isotopic effects are investigated, by using stable and radioactive Sn beams using different proximity potentials in the framework of DCM.
- The effect of deformation and orientation degree of freedom is analysed on barrier characteristics of a number of heavy ion reactions by using various proximity potentials with in Wong formalism.
- The role of spin-orbit density interaction potential, is investigated using SEDF method under frozen density approximation in O- and Ni-based reactions by using ℓ-summed Wong formula [78].

The above mentioned theoretical study, explained in the later chapters, imparts important information regarding the nuclear reaction dynamics and related nuclear structure information for better understanding of nuclear behavior in intermediate and heavy mass region.

1.6 Organization of the Thesis

The thesis is organized as follows:

Chapter 2 describes the details of the dynamical cluster-decay model (DCM), is a reformulation of preformed cluster decay model (PCM) for ground state decay, which is based on the Quantum Mechanical Fragmentation Theory ($QMFT$) for binary fragmentation, uses a collective mass transfer process. DCM is a two step process: The first step is the formation of the cluster in the compound nucleus, followed by the second step in which preformed cluster penetrates the barrier. In this model the preformation probability of all possible clusters within the mother nucleus can be calculated. The temperature dependence of the proximity potential, Coulomb interaction potential, rotational energy and binding energies are also discussed. Beside the temperature and angular momentum effects in the above mentioned dynamical cluster-decay model, the deformations and orientation effects of the reaction partners and decaying products are also investigated. Details of the nuclear potentials; one calculating using proximity theorem and other using Skyrme energy density formalism of Vautherin and Brink is also described. Details of Wong's model for calculation of fusion reaction cross sections which is a special case of the DCM with preformation probability P_0=1 is also given in this chapter.

In **Chapter** 3, we have studied the decay of CN ^{176,196}Pt*, formed in ^{112,132}Sn+^{64}Ni reaction, within the framework of the DCM by using variety of nuclear proximity potentials; one derived from SEDF-based semiclassical ETF method and other from Blocki *et al.* potential. It is observed that the GSkI and SSk forces behave nearly alike , since same fragments contribute to decay process and the same is true for SIII and Blocki *et al.* potential. The DCM gives an excellent fit for ^{196}Pt* → ^{132}Sn+^{64}Ni reaction to the measured fusion-evaporation residue (ER) and the fission cross-sections at below and above-barrier energies, with ER data needing "barrier lowering" at below-barrier energies, and the fission cross-sections show the necessity of qf contribution at the highest two/ three energies, depending on the Skyrme force used. Another interesting result is that there is a change of fission mass distribution from a predominantly asymmetric to symmetric one with decrease in the N/Z ratio of compound nucleus, independent of the choice of nuclear interaction potential, which gives an opportunity to address the isospin effects in Pt* nucleus. The fusion cross-sections are also calculated independently by using the ℓ-summed extended-Wong Model. Within the ℓ-summed extended-Wong model we find that the GSkI and SSk forces fit the total fusion cross-section data exactly, whereas SIII force needs "barrier modification" in order to fit the data at below-barrier energies.

In **Chapter** 4, various versions of nuclear proximity potentials and different values of level density parameter are employed to study the entrance channel effect in ^{190}Pt* compound nuclei. On comparing the results of calculations for the two reaction channels, it is observed that CN formation is independent of the different entrance channel and it persists even with the use of different nuclear proximity potentials and level density parameter. Beside this, the fission mass distribution of Pt isotopes formed in ^{124,126,127,128,132}Sn+^{64}Ni$\rightarrow^{188,190,191,192,196}$Pt* reactions is also studied. With the neutron excess in the projectile/target, the barrier lowering (ΔV_B) decreases (less negative), hence fusion hindrance also decreases which is in agreement with experimental observation. In addition to this, the different proximity potentials are also used with in the framework of ℓ-summed extended-Wong model for addressing the fusion hindrance phenomena. It is found that mod-Prox 1988, having strong dependence of isospin and asymmetry of colliding nuclei, describes the experimental data very well at above, and especially at below the Coulomb barrier energies with smooth variation of $\ell_{max}(E_{c.m.})$.

In **Chapter** 5, the effect of deformation and orientation on barrier height and barrier position is studied using different types of proximity potentials for some 52 colliding nuclei with mass asymmetry parameter in range of 0 to 0.96. Various proximity potentials like Prox 77, Prox 88, Prox 00, Bass 80 and Denisov DP [31] are used to extract barrier characteristics. These potentials cover a wide range of barrier and have different isospin and asymmetry dependence. With the inclusion of deformations, the barrier height and barrier position gets modified along with a significant change in the curvature. In order to study the possible effect of these deformation and orientation dependent proximity potentials, application is made in the framework of Wong formula to O-, Ca- and Ni- based reactions in medium mass region in reference to available data on fusion cross-sections at near and above the Coulomb barrier energies. For ^{16}O- and ^{48}Ca-based reactions, Prox 77 gives better comparison with experimental data as compared to other potentials around the Coulomb barrier energies whereas for ^{64}Ni-based reactions Prox 88 seems close to the experimental data. At energies above the Coulomb barrier Bass 80 and Denisov DP compete with each other. It is observed that deformation and orientation degree of freedom plays a significant role in reaction dynamics.

In **Chapter** 6, we investigated the role of deformations independently on spin saturated (spin-orbit independent) and unsaturated (spin-orbit dependent) potentials which collectively gives the nuclear interaction potential derived from Skyrme energy density formalism (SEDF). Hence the role of deformations are investigated on spin independent and spin dependent interaction potential for a variety of near-symmetric and asymmetric colliding nuclei leading to various isotopes of compound nucleus Yb*. The comparative analysis with spherical choice is also worked out. We observe that the spin-orbit density interaction barrier-height (V_{JB}) and barrier-position (R_{JB}) increase systematically with increase in number of neutrons in either the projectile or target, for spherical systems. On allowing deformation effects with optimum orientations, the barrier-height increases by a large order of magnitude, as compared to the spherical case, in going from ^{156}Yb* to ^{172}Yb* nuclear systems, except that for the oblate-shaped nuclei, the V_{JB} is highest and R_{JB} shifts towards smaller (compact) interaction radius. The temperature and use of various Skyrme forces does not change the behavior of spin-orbit density dependent (V_J) and independent (V_P) interaction potentials, except for some modification in the magnitude. Finally, we have also calculated the fusion cross-sections of ^{60,64}Ni+^{100}Mo and ^{16}O+^{144,148}Sm reactions within framework of ℓ-summed Wong model to address the fusion hindrance phenomenon. Beside this, DCM is used to study the decay of CN $^{172}Yb^{*}$, formed in two different reactions i.e. ^{124}Sn+^{48}Ca and ^{132}Sn+^{40}Ca in order to investigate the entrance channel effect and fusion enhancement phenomena.

Finally, **Chapter** 7, summarizes the overall work of the thesis. Brief notes regarding the significance of the work and conclusion drawn from it are explicitly given in this chapter. There is a definite scope for extension of this work in future.

Bibliography

[1] J. J. Thomson, Phil. Mag. **44**, 293 (1897).

[2] E. Rutherford, Phil. Mag. **21**, 669 (1911).

[3] H. Becquerel, Comp. Rend. **122**, 450 (1896).

[4] E. Rutherford, Phil. Mag. **37**, 537 (1919); **37**, 581 (1919).

[5] S. Hofmann *et al.*, Z. Phys. A **350**, 277 (1995); **354**, 229 (1996).

[6] Niyti and R. K. Gupta, Phys. Rev. C **89**, 014603 (2014).

[7] G. Kaur, N. Grover, K. Sandhu and M. K. Sharma, Nucl. Phys. A **927** 232-248 (2014).

[8] T. K. Jha, P. K. Raina, P. K. Panda and S. K. Patra, Phys. Rev. C **74**, 055803 (2006).

[9] R K Gupta, W Scheid and W Greiner, Phys. Rev. Lett. **35**, 353 (1975).

[10] R K Gupta, A Śandulescu and W Greiner, Phys. Lett. B **67**, 257 (1977).

[11] N. Bohr and J. A. Wheeler, Phys. Rev **56**, 426 (1939).

[12] V. Weisskopf, Phys. Rev **52**, 295 (1937).

[13] W. U. Schroder and J. R. Huizenga Treatise on heavy-ion science, damped nuclear reactions, (Plenum Press, New York, 1984) p. 115.

[14] C. Ngo, Prog. Part. Nucl. Phys. **16**, 139 (1986).

[15] W. J. Swiatecki, Phys. Scr. **24**, 113 (1981).

[16] B. B. Back *et al.*, Phys. Rev. C **32**, 195 (1985).

[17] C. Lebrum *et al.*, Nucl. Phys. A **321**, 207 (1979).

[18] B. Borderie *et al.*, Z. Phys. A **299**, 263 (1981).

[19] A. Nasirov *et al.*, Eur. Phys. J. A **49**, 147 (2013).

[20] D. J. Hinde *et al.*, Phys. Rev. C **53**, 1290 (1996).

[21] J. C. Mein *et al.*, Phys. Rev. C **55**, R995 (1997).

[22] K. Sandhu, M. K. Sharma and R. K. Gupta, Phys. Rev. C **86**, 064611 (2012).

[23] L. F. Canto, P. R. S. Gomes, R. Donangelo, and M. S. Hussein, Phys. Rep. **424**, 1 (2006).

[24] N. Wang, X. Wu, Z. Li, M. Liu, and W. Scheid, Phys. Rev. C **74**, 044604 (2006).

[25] V. Y. Denisov, Phys. Lett. B **526**, 315 (2002).

[26] R. Bass, Nucl. Phys. A **231**, 45 (1974).

[27] R. Bass, *Nuclear Reactions with Heavy Ions* (Springer-Verleg, Berlin, 1980).

[28] J. Blocki, J. Randrup, W.J. Swiatecki, and C.F. Tsang, Ann. Phys. (N.Y.) **105**, 427 (1977).

[29] J. Randrup and J. S. Vaagen, Phys. Lett. B **77**, 170 (1978).

[30] J. R. Birkelund and J. R. Huizenga, Phys. Rev. C **17**, 126 (1978).

[31] I. Dutt, and R. K. Puri, Phys. Rev. C **81**, 064609 (2010); *ibid* **81**, 064608 (2010).

[32] K. A. Brueckner, J. R. Buchler, and M. Kelley, Phys. Rev. **173**, 944 (1968).

[33] D. M. Brink and Fl. Stancu, Nucl. Phys. A **270**, 236 (1976).

[34] D. Vautherin and D. M. Brink, Phys. Rev. C **5**, 626 (1972).

[35] T. H. R. Skyrme, Phil. Mag. **1**, 1043 (1956); Nucl. Phys. **9**, 615 (1959).

[36] B. Grammoticos and A. Voros, Ann. Phys. **123**, 359 (1979).

[37] B. Grammoticos and A. Voros, Ann. Phys. **129**, 153 (1980).

[38] R. K. Puri *et al.*, Phys. Rev. C **43**, 315 (1991).

[39] R. K. Puri and R. K. Gupta, Phys. Rev. C **51**, 1568 (1995).

[40] M. K. Sharma, H. Kumar, R. K. Puri, and R. K. Gupta, Phys. Rev. C **56**, 1175 (1997).

[41] M. K. Sharma, R. K. Puri, and R. K. Gupta, Eur. Phys. J. A **2**, 69 (1998).

[42] R. Arora, R. K. Puri, and R. K. Gupta, Eur. Phys. J. A **8**, 103 (2000).

[43] R. K. Gupta, D. Singh, and W. Greiner, Phys. Rev. C **75**, 024603 (2007).

[44] M. Brack, C. Guet, and H. -B. Hakansson, Phys. Rep. **123**, 275 (1985).

[45] J. Bartel and K. Bencheikh, Eur. Phys. J. A. **14**, 179 (2002).

[46] P. G. Reinhard *et al.*, Phys. Rev. C **60**, 014316 (1999).

[47] B. K. Agrawal, S. Shlomo, and V. Kim Au, Phys. Rev. C **72**, 014310 (2005).

[48] B. K. Agrawal, S. K. Dhiman, and R. Kumar, Phys. Rev. C **73**, 034319 (2006).

[49] M. Dutra *et al.*, Phys. Rev. C **85**, 035201 (2012).

[50] G.-Q. Li, J. Phys. G: Nucl. Part. Phys. **17**, 1 (1991).

[51] R. Kumar, M. K. Sharma, and R. K. Gupta, Nucl. Phys. A **870**, 42 (2011).

[52] V. Yu. Denisov and W. Nörenberg, Eur. Phys. J. A **15**, 375 (2002).

[53] A. Dobrowolski, K. Pomorski, and J. Bartel, Nucl. Phys. A **729**, 713 (2003).

[54] L. R. B. Elton, *Nuclear Sizes* (Oxford University Press, London, 1961).

[55] H. de Vries, C. W. de Jager, and C. de Vries, At. Data Nucl. Data Tables **36**, 495 (1987).

[56] K. Hagino *et al.*, Phys. Rev. C **55**, 276 (1997).

[57] K. Hagino, A. Vitturi, C. H. Dasso and S. M. Lenzi, Phys. Rev. C **61**, 037602 (2002).

[58] W. Greiner, *International NATO Advanced Study Institute (NASI) Course on Quantum Electrodynamics of Strong Fields*, Lahnstein 1981;

M. Seiwert, N. Abul-Naga, V. Oberacker, J. A. Maruhn and W. Greiner, Gesellschaft für Schwerionenforschung (GSI) Annual Report 1981.

[59] A. J. Baltz and B. F. Bayman, Phys. Rev. **C 26**, 1969 (1982).

[60] M. J. Rhoades-Brown, V. E. Oberacker, M. Seiwert and W. Greiner, Z. Phys. **A 310**, 287 (1983).

[61] N. Malhotra and R.K. Gupta, Phys. Rev. **C 31**, 1179 (1985).

[62] K. Nishio, H. Ikezoe, S. Mitsuoka, K. Satou, and S. C. Jeong, Phys. Rev. C **63**, 044610 (2001).

[63] R. K. Gupta, M. Balasubramaniam, R. Kumar, N. Singh, M. Manhas, and W. Greiner, J. Phys. G: Nucl. Part. Phys. **31**, 631 (2005).

[64] R. K. Gupta, in *Cluster in Nuclei*, Lecture Notes in Physics 818, Vol. I, edited by C. Beck (Springer-Verlag, Berlin, 2010), p. 223.

[65] K. Sandhu, M. K. Sharma, and R. K. Gupta, Phys. Rev. C **85**, 024604 (2012).

[66] M. Kaur, R. Kumar, and M. K. Sharma, Phys. Rev. C **85**, 014609 (2012).

[67] S. S. Malik and R. K. Gupta, Phys. Rev. C **39**, 1992 (1989).

[68] S. Kumar and R.K. Gupta, Phys. Rev. C **55**, 218 (1997).

[69] R. K. Gupta and W. Greiner, in *Heavy Elements and Related New Phenomena*, edited by W. Greiner and R. K. Gupta (World Scientific, Singapore, 1999), Vol. **I**, p. 397; *ibid* Vol. **I**, p. 536.

[70] R. J. Charity, M. A. McMahan, G. J. Wozniak, R. J. McDonald, L. G. Moretto, D. G. Sarantites, L. G. Sobotka, G. Guarino, A. Pantaleo, L. Fiore, A. Gobbi, and K.D. Hildenbrand, Nucl. Phys. A **483**, 371 (1988).

[71] T. Matsuse, C. Beck, R. Nouicer, and D. Mahboub, Phys. Rev. C **55**, 1380 (1997).

[72] S. J. Sanders, A. Szanto de Toledo, and C. Beck Phys. Rep. **311**, 487 (1999).

[73] N. J. Davidson, S. S. Hsiao, J. Markram, H. G. Miller, and Y. Tzeng, Nucl. Phys. A **570**, 61c (1994).

[74] G. Royer and J. Mignen, J. Phys. G: Nucl. Part. Phys. **18**, 1781 (1992), and earlier references therein.

[75] S. Shlomo and J. B. Natowiz, Phys. Rev. **C44**, 2878 (1991).

[76] C. Y. Wong, Phys. Rev. Lett. **31**, 766 (1973).

[77] D. L. Hill and J. A. Wheeler, Phys. Rev. **89**, 1102 (1953); T. D. Thomas, Phys. Rev. **116**, 703 (1959).

[78] R. Kumar, M. Bansal, S. K. Arun, and R. K. Gupta, Phys. Rev. C **80**, 034618 (2009).

[79] J. F. Liang *et al.*, Phys. Rev. C. **85**, 031601(R) (2012).

Chapter 2

Methodology

2.1 Introduction

In the present work, the dynamics of fusion-fission and associated nuclear structure effects are investigated using different nuclear interaction potential with in the framework of dynamical cluster decay model (DCM) [1]- [10] as well as wong model [11]- [13]. For the formation of compound nucleus, Wong model is used in which penetration probability to cross the barrier for forming composite system is calculated by using Hill-wheeler approximation. To investigate the nuclear disintegration of excited compound nucleus into intermediate mass fragments (IMFs) and fusion-fission (ff) production along with the process of multiple particle emission, the Dynamical Cluster decay Model is used. The advantage of using the DCM is that it gives the relative preformation probability of all channels through which an excited compound nucleus can decay. This cluster preformation probability provides a significant information about the nuclear structure of CN system and its decaying fragments.

DCM is a two step process: The first step is the formation of the cluster in the compound nucleus, followed by the second step in which preformed cluster penetrates the barrier. Here, the penetration probability P across the interaction barrier is generally calculated by using WKB approximation. DCM is based on well known

Quantum Mechanical Fragmentation theory, (QMFT) [14]- [27] which is based on collective co-ordinate approach. It is only theory, given prior to experiments, that brings out clearly the applicability of the quantum concept of probability and role of shell effects not only for fusion reactants but also for the other related processes of fission and cluster radioactivity. In QMFT the potential is calculated using macro-microscopic method of Strutinsky [28]. This average two body potential successfully explains the cold and hot fusion reaction dynamics. The QMFT is based on the fact that the fragments are pre-born prior to the decay of the compound nucleus and the preformation probability P_0 of the decaying fragments or clusters formed in the mother nucleus can be calculated by solving a stationary Schrödinger equation in mass fragmentation coordinate. It is relevant to mention here that the deformation and orientation effects of the reaction partners and decay products are explicitly included together with temperature and angular momentum contribution in these models.

To understand the formation and decay of nuclear systems, the precise and systematic understanding of the ion-ion interaction between the colliding nuclei is required. This thesis presents the calculations using two kind of nuclear potentials; one calculated using proximity theorem and other using energy density formalism. With in energy density formalism, two different functional forms of Hamiltonian density are available, one due to Bruckner *et al.* [29]- [32] and other due to Vautherin and Brink [33] which uses the density dependent Skyrme interactions [34]. Here, the later one is used due to an advantage that it is capable of explaining and reproducing the ground state property of large number of nuclei. The energy density formalism is used with Skyrme interaction with in an extended Thomas-Fermi (ETF) approximations for the kinetic energies and spin-orbit terms, upto second order in the spatial derivatives with nucleon density calculated from two parameter Fermi density. The details of ETF method of SEDF is given in section 2.3. Finally the Wong formula is described for estimating the fusion reaction cross-sections in section 2.4.

2.2 The Dynamical Cluster-decay Model for hot and rotating compound systems

The dynamical cluster decay model (DCM) for hot and rotating nuclei is a reformulation of the preformed cluster model (PCM) for ground-state decays in cluster radioactivity (CR) and related phenomena [35]- [40]. The DCM is based on the quantum mechanical fragmentation theory (QMFT) of cold fusion phenomenon in heavy ion reactions and fission dynamics. The $QMFT$ is worked out in terms of the following collective variables:

(i) relative separation coordinate R between the two nuclei or, two fragments.

(ii) Mass and charge fragmentation co-ordinates [14, 26] defined as

$\eta = (A_1 - A_2)/(A_1 + A_2)$ [and $\eta_Z = (Z_1 - Z_2)/(Z_1 + Z_2)$]

(iii) Neck parameter ε, defined by the ratio $\varepsilon = E_0/E'$;

where E_0 is the actual height of the barrier and E' is the fixed barrier of the two center oscillator. $\epsilon = 0$ represents a broad neck formation, whereas $\epsilon = 1$ gives that the neck is fully squeezed in, corresponding to the asymptotic region.

(iv) The multipole deformations $\beta_{\lambda i}$ (λ=2, 3, 4... and i=1, 2) and the orientation degrees of freedom $\theta_i (i = 1, 2)$ of the two deformed colliding nuclei, which in DCM characterizes, respectively as

(i) the nucleon-division (or -exchange) between outgoing fragments, and

(ii) the transfer of kinetic energy of incident channel ($E_{c.m.}$) to internal excitation (total excitation or total kinetic energy, TXE or TKE) of the outgoing channel, since the fixed $R = R_a$ (defined later), at which the process is calculated, depends on temperature T as well as on η, i.e. $R(T, \eta)$.

This energy transfer process follows the relation

$$E^*_{CN} = E_{c.m.} + Q_{in} = \mid Q_{out}(T) \mid + TKE(T) + TXE(T). \tag{2.1}$$

The excitation energy E^*_{CN} of the compound nucleus is related to the nuclear temperature T (in MeV), through a semi-empirical statistical relation [41] as:

$$E^*_{CN} = E_{c.m.} + Q_{in} = \frac{1}{a}AT^2 - T \qquad (MeV). \tag{2.2}$$

where a = 9-11 depending on the mass of the compound nucleus. Q_{in} is the entrance channel Q-value given by $Q_{in} = B_1 + B_2 - B_{CN}$ where B's are the binding energies. Using the decoupled approximation to R- and η-motions, the DCM defines the decay cross section, in terms of partial waves, as [42,43]

$$\sigma = \sum_{\ell=0}^{\ell_{max}} \sigma_\ell = \frac{\pi}{k^2} \sum_{\ell=0}^{\ell_{max}} (2\ell+1) P_0 P; \qquad k = \sqrt{\frac{2\mu E_{c.m.}}{\hbar^2}} \tag{2.3}$$

where, ℓ_{max} is the maximum angular momentum, fixed for the light particle cross-section approaching zero, i.e., $\sigma_{ER}(\ell) \rightarrow 0$ at $\ell = \ell_{max}$ and $\mu = mA_1A_2/(A_1 + A_2)$ is the reduced mass with m as the nucleon mass. P_0 is the preformation probability, refers to η-motion and P is the penetrability, to R-motion.

The preformation probability P_0 for each ℓ is obtained by solving the stationary Schrödinger equation in η, at a fixed R=R_a

$$\left[-\frac{\hbar^2}{2\sqrt{B_{\eta\eta}}} \frac{\partial}{\partial \eta} \frac{1}{\sqrt{B_{\eta\eta}}} \frac{\partial}{\partial \eta} + V(\eta) \right] \psi^\nu(\eta) = E^\nu_\eta \psi^\nu(\eta), \tag{2.4}$$

The states $\psi^\nu(\eta)$ are the vibrational states in the potential $V(\eta)$ and are labelled by the quantum numbers $\nu = 0, 1, 2....$ $B_{\eta\eta}$ is the mass parameter, defining the kinetic energy term. We use here the classical mass parameters of Kröger and Scheid [44] which is based on the hydrodynamical flow, as shown in Fig. 2.1 and gives a simple analytical expression, whose predictions are shown to compare nicely

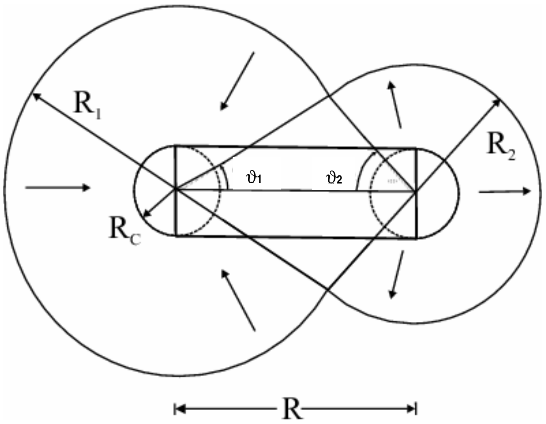

Figure 2.1: The geometry of the classical hydrodynamical model of Kröger and Scheid for calculating the mass parameter $B_{\eta\eta}$.

with the microscopic cranking model calculations. For the $B_{\eta\eta}$ mass we get,

$$B_{\eta\eta} = \frac{AmR^2}{4}\left[\frac{v_t(1+\gamma)}{v_c(1+\delta^2)} - 1\right] \tag{2.5}$$

with

$$\gamma = \frac{R_c}{2R}\left[\frac{1}{1+\cos\vartheta_1}\left(1-\frac{R_c}{R_1}\right) + \frac{1}{1+\cos\vartheta_2}\left(1-\frac{R_c}{R_2}\right)\right] \tag{2.6}$$

$$\delta = \frac{1}{2R}\left[(1-\cos\vartheta_1)(R_1-R_c) + (1-\cos\vartheta_2)(R_2-R_c)\right] \tag{2.7}$$

$$v_c = \pi R_c^2 R \tag{2.8}$$

and $v_t = v_1 + v_2$, is the total conserved volume. The angles ϑ_1 and ϑ_2 and geometry of the model are shown in Fig. 2.1. For $\vartheta_1 = \vartheta_2 = 0$, $\delta = 0$ which corresponds to two touching spheres. $R_c(\neq 0)$ is the radius of a cylinder of length R, having a homogeneous flow in it; whose existence is assumed for the mass transfer between the two spherical fragments. This formalism is generalized for deformed nuclei by using the radii R_1 and R_2 for deformed nuclei, discussed latter in Eq.

2.15.

On solving Eq. (2.4) numerically, $|\psi^{\nu}(\eta)|^2$ gives the probability P_0 of finding the mass fragmentation η at a fixed R on the decay path.

$$P_0(A_2) \propto |\psi^{\nu}(A_2)|^2 \tag{2.9}$$

Starting from the nuclear ground state in spontaneous fission or cluster decay, and to have complete adiabatically, only the lowest vibrational state $\nu = 0$ is occupied. Then, the mass (or charge) distribution yield, proportional to the probability $|\psi(\eta)|^2$ (or $|\psi(\eta_Z)|^2$) of finding a certain mass (or charge) fragmentation η (or η_Z) at a position R on the decay path, when scaled to, say, mass A_2 of one of the fragments ($d\eta = \frac{2}{A}$) is given by:

$$Y(A_2) = |\psi_R^{(0)}(A_2)|^2 \frac{2}{A}\sqrt{B_{\eta\eta}(A_2)}). \tag{2.10}$$

However, if the system is excited or we allow interaction between various degrees of freedom, higher values of ν would also contribute. These enter via the excitation of higher vibrational states, and through the temperature dependent potential V and masses B_{ij}.

The possible consequences of including the excitations of higher vibrational states is considered by assuming a Boltzmann-like occupation of excited states, such as

$$|\psi^{\nu}(\eta)|^2 = \sum_{\nu=0}^{\infty} |\psi^{\nu}(\eta)|^2 \exp\left(-\frac{E_{\eta}^{\nu}}{T}\right) \tag{2.11}$$

The penetrability P in Eq. (2.3) is calculated by the WKB integral and is given as

$$P = \exp\left[-\frac{2}{\hbar}\int_{R_a}^{R_b} \{2\mu[V(R) - Q_{eff}]\}^{1/2} dR\right]. \tag{2.12}$$

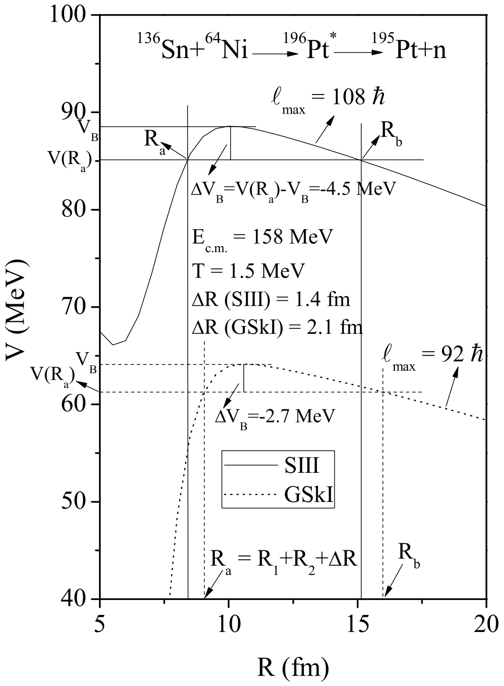

Figure 2.2: The scattering potential for ^{196}Pt*→^{195}Pt+n at fixed temperature T=1.5 MeV using SIII and GSkI forces. The barrier penetration points and barrier lowering parameter defined as $\Delta\ V_B$=$V(R_a)$-V_B is also shown for both the forces at their respective ℓ_{max} value.

This means that the tunnelling begins at R = R_a and terminates at R = R_b with $V(R_a,T) = V(R_b,T) = TKE(T) = Q_{eff}$ for the two turning points which is also illustrated in Fig. 2.2 for ^{196}Pt*→^{195}Pt+n reaction using two Skyrme forces (SIII and GSkI). Q_{eff} is the effective Q-value of decay process, and the first turning point

$$R_a(T) = R_t + \Delta R(\eta, T) \tag{2.13}$$

where

$$R_t = R_1(\alpha_1, T) + R_2(\alpha_2, T) \tag{2.14}$$

with

$$R_i(\alpha_i, T) = R_{0i}(T)[1 + \sum_{\lambda} \beta_{\lambda i} Y_{\lambda}^{(0)}(\alpha_i)], \tag{2.15}$$

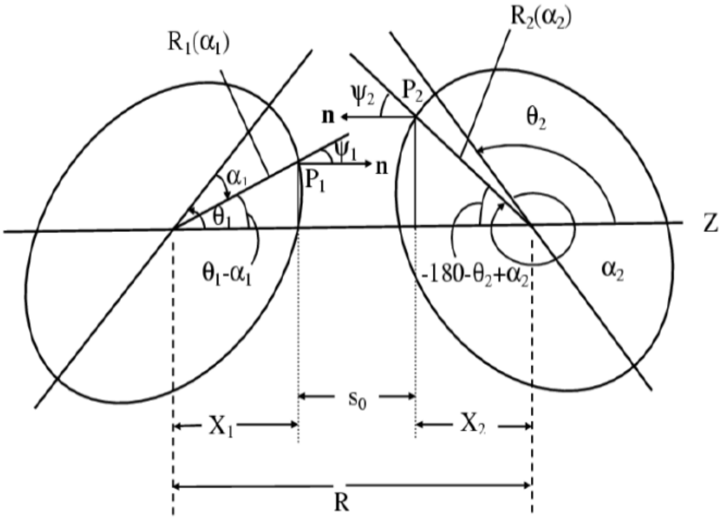

Figure 2.3: Schematic configurations of two axially symmetric deformed, oriented nuclei, lying in the same plane and for various θ_1 and θ_2 values in the range 0^0 to 180^0.

and

$$R_{0i}(T) = R_{0i}(1 + 0.0007T^2). \tag{2.16}$$

The values of R_{0i} are different for different nuclear interaction potentials which are explained later. Here λ=2,3,4... and α_i is an angle that the radius vector R_i of the colliding nuclei makes with the symmetry axis (see Fig. 2.3), measured clockwise. $\Delta R(\eta, T)$ is the neck-length parameter that assimilates the neck formation effects and also allows to define the effective barrier-lowering parameter $\Delta V_B(\ell)$ for each ℓ as the difference between the actual used barrier $V(R_a, \ell)$ and the top of the barrier $V_B(\ell)$ for each ℓ, by defining their difference $\Delta V_B(\ell)$ as the effective "lowering of the barrier" as:

$$\Delta V_B(\ell) = V(R_a, \ell) - V_B(\ell) \tag{2.17}$$

Note, ΔV_B for each ℓ is defined as a negative quantity since the actually used barrier is effectively lowered. This is illustrated in Fig. 2.2. Thus, "barrier lowering" ΔV_B is controlled by the fitting parameter ΔR.

The structure information of the decaying nucleus is contained in preformation factor P_0 via the fragmentation potential $V(\eta, R, T)$, appearing in Eq. (2.4).

The fragmentation potential reads as,

$$\begin{aligned} V(\eta, R, \ell, T) &= -\sum_{i=1}^{2} B_i(A_i, Z_i, \beta_{\lambda i}, T) + V_C(R, Z_i, \beta_{\lambda i}, \theta_i, \phi, T) \\ &+ V_N(R, A_i, \beta_{\lambda i}, \theta_i, \phi, T) + V_\ell(R, A_i, \beta_{\lambda i}, \theta_i, \phi, T) \end{aligned} \tag{2.18}$$

V_C and V_ℓ are the temperature-, deformations- and orientations-dependent Coulomb and angular momentum potentials, described in sections 2.2.1 and 2.2.2 respectively. V_N is the additional attraction due to nuclear interaction potential calculated either by proximity theorem (as discussed in section 2.2.3) or by Skyrme energy density formalism (as discussed in section 2.2.4). B_i (i=1,2) appearing in Eq. (2.18), are the binding energies of the two nuclei, available from the experimental data of Audi-Wapstra [45]. Wherever the experimental B's are not available, the theoretical binding energies of Möller *et al.* [46] are used. Note that within the Strutinsky renormalization procedure [28], the binding energies contain both the macroscopic (liquid drop part) and the microscopic (shell correction) part, which allows us to define the binding energy B of a nucleus at temperature T as the sum of liquid drop energy $V_{LDM}(T)$ and shell correction $\delta U(T)$ i.e

$$B(T) = V_{LDM}(T) + \delta U exp\Big(-\frac{T^2}{{T_0}^2}\Big). \tag{2.19}$$

The calculations of fragmentation potential involve all the possible decaying fragments subsequently exhibiting idea about possible emergence of decay channels such ER, IMF, fission etc. The T dependent liquid drop part of the binding energy $V_{LDM}(T)$ is from Davidson *et al.* [47], based on the semi-empirical mass formula of Seeger [48]. The shell corrections δU in Eq. (2.19) are considered to vanish exponentially for $E^* \geq 60\ MeV$, giving $T_0 = 1.5\ MeV$. At higher excitation energies the shell corrections vanish completely and only the liquid drop part of energy is present. The shell corrections play an important role in determining or empirical fitting of nuclear masses, because the nuclear masses calculated by using the smooth liquid drop formula show large deviations with respect to the experimental data. It means that in the experimental masses there exist deep minima at specific neutron and/or proton numbers indicating the presence of shell structure, the so-called magic numbers in nuclei. This characteristic behavior cannot be reproduced by the liquid drop part alone, which means that the introduction of microscopic shell correction in the mass formula is essential. Thus, shell corrections accounts for the removal of deviation from the liquid drop calculations (uniform distribution of nucleons), and are defined, within Strutinsky method [28].

In general, the microscopic shell correction, along with the liquid drop part, give a proper description of the binding energy of the nucleus, except for some light mass nuclei as shell corrections are not adequately known in this mass region. Henceforth the macro-microscopic calculations of Möller *et al.* [46] are tabulated for $Z \geq 8$ only. Alternatively, one can use the empirical shell correction method of Myers-Swiatecki which again is not satisfactory for light nuclei ($Z \leq 16$). The authors of [42] have modified this empirical method and estimated the shell corrections for light mass nuclei.

2.2.1 The Coulomb potential

Coulomb potential describes the force of repulsion between two interacting nuclei due to their charges. It acts along the line joining the two nuclei. The Coulomb potential for two interacting spherical nuclei is given as

$$V_c = \frac{Z_1 Z_2 e^2}{R} \tag{2.20}$$

For deformed and oriented interacting nuclei, different authors [49]- [52] have given different expressions. The Coulomb potential for two interacting hot, deformed and oriented nuclei is given as [49]:

$$\begin{aligned} V_c(Z_i,\beta_{\lambda i},\theta_i,\alpha_i,T) &= \frac{Z_1Z_2e^2}{R(T)}+3Z_1Z_2e^2\sum_{\lambda,i=1,2}\frac{1}{2\lambda+1}\frac{R_i^{\lambda}(\alpha_i,T)}{R(T)^{\lambda+1}}Y_{\lambda}^{(0)}(\theta_i) \\ & \quad \Big[\beta_{\lambda i}+\frac{4}{7}\beta_{\lambda i}^2Y_{\lambda}^{(0)}(\theta_i)\Big], \end{aligned} \tag{2.21}$$

$Y_{\lambda}^{(0)}(\theta_i)$ are the spherical harmonics function.

2.2.2 Rotational Energy due to angular momentum

The rotational motion gives an additional energy due to the angular momentum ℓ, defined as

$$V_\ell = \frac{\hbar^2\ell(\ell+1)}{2I(T)} \tag{2.22}$$

with I is the moment of inertia. $\mu = \frac{A_1A_2}{A_1+A_2}m$ is the reduced mass with m the nucleon mass. $I(T)= I_{NS}=\mu R^2$, is the non-sticking limit of moment of inertia. In the complete sticking limit, the moment of inertia I_S is given as,

$$I_s(T) = \mu R^2 + \frac{2}{5}A_1mR_1^2(\alpha_1,T)+\frac{2}{5}A_2mR_2^2(\alpha_2,T). \tag{2.23}$$

However in DCM, we use the sticking limit whereas in Wong formula (discussed in section 2.3), non-sticking limit of moment of inertia is used.

2.2.3 The Proximity Potential for deformed, oriented nuclei

When two surfaces approach each other within a small distance of less than $\sim 2fm$, comparable with the surface thickness of interacting nuclei, or when a nucleus is at the verge of dividing into two fragments, then the two surfaces actually face each other across a small gap or crevice. In both cases, the surface energy term alone could not give rise to the strong attraction that is observed when the two surfaces are brought in close proximity. Such additional attractive forces are called proximity forces and the additional potential due to these forces is called the proximity potential. The various versions of proximity potentials used in present work are discussed below:

Proximity 1977 (Blocki)

Blocki *et al.* [53] have reanalyzed and extended a theorem, originally due to Deryagin [54], according to which the force between two gently curved surfaces in close proximity is proportional to the interaction potential per unit area between the two flat surfaces. The original expression of Blocki based on the pocket formula was for spherical nuclei, and is given as

$$\begin{aligned} V_N(s_0) &= f(sh., geo.)\Phi(s_0) \\ &= 4\pi\bar{R}\gamma b\Phi(s_0). \end{aligned} \tag{2.24}$$

The T-dependent proximity potential (V_N) for deformed and oriented nuclei is [55]

$$V_N(A_i, \beta_{\lambda i}, \theta_i, T) = 4\pi\bar{R}(T)\gamma b(T)\Phi(s_0(T)) \tag{2.25}$$

$\Phi(s_0)$ is the universal function, independent of the shapes of nuclei or the geometry of nuclear system, but depends on the minimum separation distance s_0,

$$\Phi(s_0) = \begin{cases} -\frac{1}{2}(s_0 - 2.54)^2 - 0.0852(s_0 - 2.54)^3 \\ -3.437exp(-\frac{s_0}{0.75}) \end{cases} \tag{2.26}$$

respectively, for $s_0 \leq 1.2511$ and $s_0 \geq 1.2511$. Here, s_0 is defined in units of b, i.e. s_0 is s_0/b. This function is defined for negative (the overlap region), zero (touching configuration) and positive values of s_0. b is the diffuseness of the nuclear surface [56],

$$b(T) = 0.99(1 + 0.009T^2). \tag{2.27}$$

The γ is the specific nuclear surface tension given by

$$\gamma = \gamma_0 \left[1 - k_s \left(\frac{N - Z}{A}\right)^2\right] MeV fm^{-2} \tag{2.28}$$

Here N and Z are the total number of neutrons and protons. In the present version, γ_0 and k_s were taken to be 0.9517 MeV/fm^2 and 1.7826, respectively.

$\bar{R}(T)$ is the mean curvature radius (for details see Ref. [55]). The radius vector, R_{0i} for this potential is given as:

$$R_{0i} = \left[1.28A_i^{1/3} - 0.76 + 0.8A_i^{-1/3}\right]. \tag{2.29}$$

Proximity 1988 (Prox 88)

Möller and Nix [57] improved the mass formula by changing the value of coefficients γ_0 and k_s = 1.2496 MeV.fm^{-2} and 2.3, respectively. This modified version was labelled as "Proximity 1988" in 1994 by Reisdrof [58]. It is to be noted that this set of coefficients give stronger attraction i.e. deeper pocket and includes stronger isospin effect as compared to Prox 77.

Bass 1980 (Bass 80)

The universal function for this potential [58] is given by,

$$\Phi(s) = [0.033exp(\frac{s}{3.5}) + 0.007exp(\frac{s}{0.65})]^{-1}. \tag{2.30}$$

The radius vector, R_{0i} for this potential is same as Prox 77.

New Denisov Potential (Denisov DP)

In 2002, Denisov propose a simple analytical expression for the nuclear part of the interaction potential $V_N(R)$ between two nuclei [59], given by

$$\begin{aligned} V_N(r) &= -1.989843\bar{R}\Phi(r - R_1 - R_2 - 2.65)[1 + 0.003525139(\frac{A_1}{A_2} + \frac{A_2}{A_1})^{3/2} \\ &\quad -0.4113263(I_1 + I_2)] \end{aligned} \tag{2.31}$$

with $I_i = (N_i - Z_i)/A_i$. Recently, Dutt and Puri [60] used the radius formula of Royer and Rousseau [61], given by

$$R_{0i} = 1.2332A_i^{1/3}[1 + 2.348443/A_i - 0.151541(A_i - 2Z_i)/A_i] \tag{2.32}$$

in Denisov potential and named it as Denisov DP. The universal function $\Phi(s = r - R_1 - R_2 - 2.65)$ is same as original Denisov [59]. Deformation and temperature effects in all above mentioned potentials are included according to Eq. 2.15 and 2.16 respectively. For more details about other proximity potentials used in this thesis see Ref. [60, 62].

All the proximity potentials used here as shown in Fig. 2.4 are having different isospin and asymmetry dependence. Moreover, these nuclear proximity potentials cover a wide range of barrier characteristics and hence different barrier characteristics modify the fusion cross-sections [62]. Henceforth it is advocated that proper choice of nuclear proximity potential is essential for adequate description of nuclear reaction dynamics. Alternatively, one can also estimate the nuclear proximity potential by employing well known Skyrme energy density formalism and the same is described in section 2.2.4.

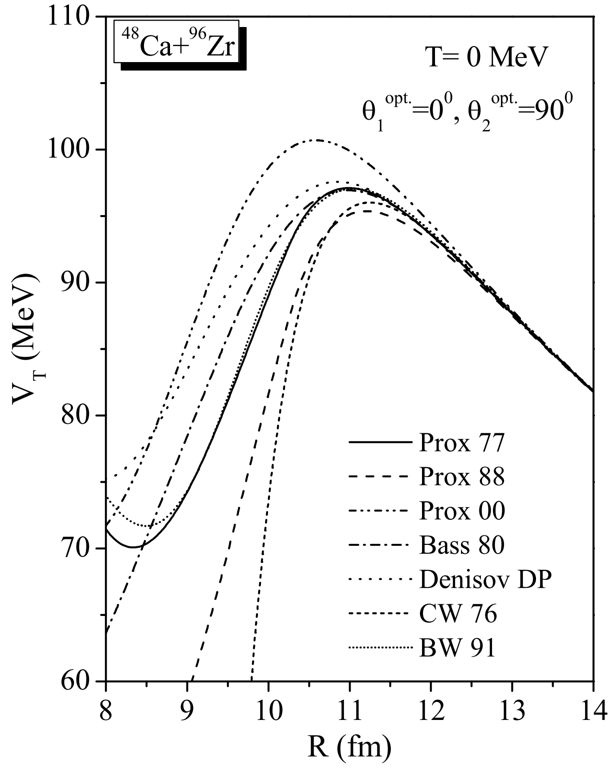

Figure 2.4: Interaction potentials calculated for ^{48}Ca+^{96}Zr reaction at T=0 MeV using various version of nuclear proximity potentials at optimum orientations $\theta_1^{opt.}=0^0$ and $\theta_2^{opt.}=90^0$.

2.2.4 Skyrme Energy Density Formalism in semiclassical extended Thomas Fermi approach

The energy density formalism defines the nuclear interaction potential as

$$V_N(R) = E(R) - E(\infty) \tag{2.33}$$

i.e. the nucleus-nucleus interaction potential as a function of separation distance, $V_N(R)$, is the difference of the energy expectation value E of the colliding nuclei that are overlapping (at a finite separation distance R) and are completely separated (at R=∞), where

$$E = \int H(\vec{r})d\vec{r}, \tag{2.34}$$

with the Skyrme Hamiltonian density [13, 33]

$$\begin{aligned}
H(\rho,\tau,\vec{J}) \;=\; & \frac{\hbar^2}{2m}\tau + \frac{1}{2}t_0\left[(1+\frac{1}{2}x_0)\rho^2 - (x_0+\frac{1}{2})(\rho_n^2+\rho_p^2)\right] \\
& +\frac{1}{2}\sum_{i=1}^{3} t_{3i}\rho^{\alpha_i}\left[(1+\frac{1}{2}x_{3i})\rho^2 - (x_{3i}+\frac{1}{2})(\rho_n^2+\rho_p^2)\right] \\
& +\frac{1}{4}\left[t_1(1+\frac{1}{2}x_1) + t_2(1+\frac{1}{2}x_2)\right]\rho\tau \\
& -\frac{1}{4}\left[t_1(x_1+\frac{1}{2}) - t_2(x_2+\frac{1}{2})\right](\rho_n\tau_n+\rho_p\tau_p) \\
& +\frac{1}{16}\left[3t_1(1+\frac{1}{2}x_1) - t_2(1+\frac{1}{2}x_2)\right](\vec{\nabla}\rho)^2 \\
& -\frac{1}{16}\left[3t_1(x_1+\frac{1}{2}) + t_2(x_2+\frac{1}{2})\right] \\
& \times\left[(\vec{\nabla}\rho_n)^2 + (\vec{\nabla}\rho_p)^2\right] \\
& -\frac{1}{2}W_0\left[\rho\vec{\nabla}\cdot\vec{J} + \rho_n\vec{\nabla}\cdot\vec{J}_n + \rho_p\vec{\nabla}\cdot\vec{J}_p\right] \\
& -A\left[\frac{1}{16}(t_1x_1+t_2x_2)\vec{J}^2 - \frac{1}{16}(t_1-t_2)(\vec{J}_p^2+\vec{J}_n^2)\right].
\end{aligned} \tag{2.35}$$

Here, $\rho=\rho_n+\rho_p$, $\tau=\tau_n+\tau_p$, and $\vec{J}=\vec{J}_n+\vec{J}_p$ are the nuclear, kinetic energy and spin-orbit densities, respectively. m is the nucleon mass, and x_j, t_j (j=0,1,2), x_{3i}, t_{3i}, α_i, (i=1,2,3), W_0, and A are the Skyrme force parameters, fitted recently by Agrawal *et al.* [63, 64], denoting GSkI, GSkII, SSk, KDE0 and KDE forces. These authors modified the earlier well known [65, 66] Hamiltonian density by introducing six additional parameters in third term (two each of x_{3i}, t_{3i} and α_i, (i=1,2)), and an additional last term with constant A=1 to account for tensor coupling with spin and gradient. For the earlier fitted Skyrme forces [65, 66], like SIII, SV, SkM*, etc., the constants A, x_{3i}, t_{3i} and α_i, i=2,3 are all zero, and t_{31}=$\frac{1}{6}t_3$, x_{31}=x_3, and α_1=α.

It is important to note here that the parameters of the new forces GSkI, GSkII, SSk, KDE0 and KDE were determined by fitting several properties of some normal and isospin-rich nuclei [64], and to study with the asymmetric and isospin-rich colliding nuclei, such forces are expected to give more realistic results.

The Hamiltonian density $H(\vec{r})$ is a function of the nucleus density $\rho(\vec{r})$, kinetic energy density $\tau(\vec{r})$ and spin density $J(\vec{r})$. The total Hamiltonian density given in Eq. (2.35) is the sum of the spin-orbit density independent Hamiltonian density $H(\rho,\tau)$ and spin-orbit density dependent Hamiltonian density $H(\rho,\vec{J})$. Then from Eq. (2.33), we get the nuclear interaction potential

$$\begin{aligned} V_N(R) &= \int \left\{ H(\rho,\tau,\vec{J}) - [H_1(\rho_1,\tau_1,\vec{J}_1) + H_2(\rho_2,\tau_2,\vec{J}_2)] \right\} d\vec{r} \\ &= V_P(R) + V_J(R) \end{aligned} \tag{2.36}$$

with the spin-orbit density independent part of the interaction potential

$$V_P(R) = \int \{H(\rho,\tau) - [H_1(\rho_1,\tau_1) + H_2(\rho_2,\tau_2)]\} d\vec{r} \tag{2.37}$$

and the spin-orbit density dependent interaction potential

$$V_J(R) = \int \left\{ H(\rho,\vec{J}) - \left[H_1(\rho_1,\vec{J}_1) + H_2(\rho_2,\vec{J}_2) \right] \right\} d\vec{r} \tag{2.38}$$

In the semiclassical ETF theory, based on SEDF, the Hamiltonian density mentioned in Eq. (2.35) can be written as

$$H(\rho,\tau,\vec{J}) = H(\rho) + H(\vec{J}) \tag{2.39}$$

where $H(\rho)$ and $H(\vec{J})$ refer to terms depending on ρ and/ or τ (τ is also a function of ρ) and $\vec{J}$, respectively. Note that, though $\vec{J}$ is also a function of ρ only but the terms that depend on $\vec{J}$ behave differently from those dependent on ρ and τ.

The kinetic energy density in ETF method, taken up to second order terms for reasons of being enough for numerical convergence [67], is (q=n or p)

$$\begin{aligned}\tau_q(\vec{r}) &= \frac{3}{5}(3\pi^2)^{2/3}\rho_q^{5/3} + \frac{1}{36}\frac{(\vec{\nabla}\rho_q)^2}{\rho_q} + \frac{1}{3}\Delta\rho_q + \frac{1}{6}\frac{\vec{\nabla}\rho_q\cdot\vec{\nabla}f_q + \rho_q\Delta f_q}{f_q} - \frac{1}{12}\rho_q\left(\frac{\vec{\nabla}f_q}{f_q}\right)^2 \\ &+ \frac{1}{2}\rho_q\left(\frac{2m}{\hbar^2}\right)^2\left(\frac{W_0}{2}\frac{\vec{\nabla}(\rho+\rho_q)}{f_q}\right)^2, \qquad (2.40)\end{aligned}$$

with f_q as the effective mass form factor,

$$\begin{aligned}f_q(\vec{r}) &= 1 + \frac{2m}{\hbar^2}\frac{1}{4}\left\{t_1(1+\frac{x_1}{2}) + t_2(1+\frac{x_2}{2})\right\}\rho(\vec{r}) \\ &- \frac{2m}{\hbar^2}\frac{1}{4}\left\{t_1(x_1+\frac{1}{2}) - t_2(x_2+\frac{1}{2})\right\}\rho_q(\vec{r}). \qquad (2.41)\end{aligned}$$

Note that both τ_q and f_q are each functions of ρ_q and/ or ρ only.

The spin $\vec{J}$ is a purely quantal property, and hence has no contribution in the lowest (TF) order. However, at the ETF level, the second order contribution gives

$$\vec{J}_q(\vec{r}) = -\frac{2m}{\hbar^2}\frac{1}{2}W_0\frac{1}{f_q}\rho_q\vec{\nabla}(\rho+\rho_q), \qquad (2.42)$$

also a function of ρ_q and/ or ρ alone.

For the composite system, $\rho = \rho_1 + \rho_2$, and the $\tau(\rho)$ and $\vec{J}(\rho)$ are added as follows:

$$\begin{aligned}\tau(\rho) &= \tau_1(\rho_1) + \tau_2(\rho_2), \\ \vec{J}(\rho) &= \vec{J}_1(\rho_1) + \vec{J}_2(\rho_2), \qquad (2.43)\end{aligned}$$

with $\rho_i = \rho_{in} + \rho_{ip}$, $\tau_i(\rho_i) = \tau_{in}(\rho_{in}) + \tau_{ip}(\rho_{ip})$, and $\vec{J}_i(\rho_i) = \vec{J}_{in}(\rho_{in}) + \vec{J}_{ip}(\rho_{ip})$.

Note that $\vec{J}$ is also a function of ρ alone but, as already noted above, in Eq.

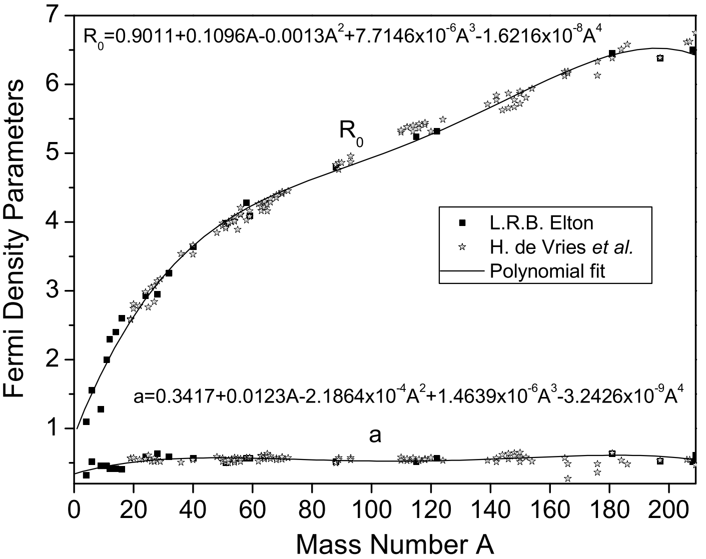

Figure 2.5: The half-density radius R_0 and the surface thickness a in fm, plotted as a function of mass number A of nuclei, each fitted to a polynomial in A. The data are from [69, 70].

(2.36 or 2.38) we still define the Hamiltonian density separately for $\vec{J}$-dependent part because the behaviors of the two parts of the potentials are different (discussed in Chapter 6).

For nuclear density ρ_i, the two-parameter Fermi density (FD) distribution is used, which is made T-dependent as [68]

$$\rho_i(z_i) = \rho_{0i}(T)\left[1+\exp\left(\frac{z_i - R_i(T)}{a_i(T)}\right)\right]^{-1} \quad -\infty \leq z \leq \infty \tag{2.44}$$

with $z_2 = R - z_1 = [R_1(\alpha_1) + R_2(\alpha_2) + s] - z_1$, and central density

$$\rho_{0i}(T) = \frac{3A_i}{4\pi R_i^3(T)}[1+\frac{\pi^2 a_i^2(T)}{R_i^2(T)}]^{-1}. \tag{2.45}$$

Then, since $\rho_i = \rho_{n_i} + \rho_{p_i}$, so for nucleon density we define

$$\rho_{n_i} = (N_i/A_i)\rho_i \qquad \text{and} \qquad \rho_{p_i} = (Z_i/A_i)\rho_i, \tag{2.46}$$

with half density radii R_{0i} and surface thickness parameters a_i at T=0, obtained by fitting the experimental data to respective polynomials (see fig. 2.4) in nuclear mass region A=4-238, as [69, 70]

$$\begin{aligned}R_{0i}(T=0) &= 0.9543 + 0.0994A_i - 9.8851\times10^{-4}A_i^2 \\ &\quad +4.8399\times10^{-6}A_i^3 - 8.4366\times10^{-9}A_i^4 \\ a_i(T=0) &= 0.3719 + 0.0086A_i - 1.1898\times10^{-4}A_i^2 \\ &\quad +6.1678\times10^{-7}A_i^3 - 1.0721\times10^{-9}A_i^4. \qquad (2.47)\end{aligned}$$

The T-dependence in the above formulas are then introduced as in Ref. [71],

$$\begin{aligned}R_{0i}(T) &= R_{0i}(T=0)[1+0.0005T^2], \\ a_i(T) &= a_i(T=0)[1+0.01T^2]. \qquad (2.48)\end{aligned}$$

The above mentioned nuclear proximity potentials are employed to govern the formation and decay processes of variety of heavy ion induced reactions. The decay channels described in section 2.2 are governed via dynamical cluster decay model (DCM) and the formation process (fusion cross-section) are described using well known Wong formula described below.

2.3 Wong Formula and its extension to include explicit summation of ℓ effects

2.3.1 Wong formula

According to Wong [52], the fusion cross-section, in terms of angular-momentum ℓ partial waves, for two deformed and oriented nuclei (with orientation angles θ_i), lying in two same planes, and colliding with center-of-mass (c.m.) energy $E_{c.m.}$, is

$$\sigma(E_{c.m.},\theta_i)=\frac{\pi}{k^2}\sum_{\ell=0}^{\ell_{max}}(2\ell+1)P_\ell(E_{c.m.},\theta_i), \tag{2.49}$$

with $k=\sqrt{\frac{2\mu E_{c.m.}}{\hbar^2}}$, and μ as the reduced mass. Here, P_ℓ is the transmission coefficient for each ℓ which describes the penetration of barrier is given by,

$$V_T^\ell(R,E_{c.m.},\theta_i)=V_N(R,A_i,\beta_{\lambda i},T,\theta_i)+V_C(R,Z_i,\beta_{\lambda i},T,\theta_i)+V_\ell(R,A_i,\beta_{\lambda i},T,\theta_i), \tag{2.50}$$

Using Hill-Wheeler [72] approximation of assimilating the shape of the interaction barrier $V_\ell(R,E_{c.m.},\theta_i)$ through an inverted harmonic oscillator $[V_T^\ell(R,E_{c.m.},\theta_i)=V_B^\ell(E_{c.m.},\theta_i)-\frac{1}{2}\mu\omega^2(R-R_B^\ell)^2]$, the penetrability P_ℓ, in terms of its barrier height $V_B^\ell(E_{c.m.},\theta_i)$ and curvature $\hbar\omega_\ell(E_{c.m.},\theta_i)$, is

$$P_\ell=\left[1+\exp\left(\frac{2\pi(V_B^\ell(E_{c.m.},\theta_i)-E_{c.m.})}{\hbar\omega_\ell(E_{c.m.},\theta_i)}\right)\right]^{-1}, \tag{2.51}$$

with $\hbar\omega_\ell(E_{c.m.},\theta_i)$, evaluated at the barrier position $R=R_B^\ell$ corresponding to the maximum barrier height $V_B^\ell(E_{c.m.},\theta_i)$, given as

$$\hbar\omega_\ell(E_{c.m.},\theta_i)=\hbar\left[|d^2V^\ell(R)/dR^2|_{R=R_B^\ell}/\mu\right]^{1/2}, \tag{2.52}$$

and, the R_B^ℓ obtained from the condition

$$|dV_T^\ell(R)/dR|_{R=R_B^\ell}=0 \tag{2.53}$$

Using Eqs. 2.52 and 2.53, Wong calculated $\hbar\omega_\ell$ and R_B^ℓ for the case of ^{16}O + ^{238}U using a diffuse well with the parameters of Viola and Sikkeland [73] and found that $\hbar\omega_\ell$ and R_B^ℓ are rather insensitive to ℓ. This result justifies the following parameterization in the region of ℓ=0:

(i) $\hbar\omega_\ell \approx \hbar\omega_0$, and (ii) $V_B^\ell \approx V_B^0 + \frac{\hbar^2\ell(\ell+1)}{2\mu {R_B^0}^2}$,

which means to assume $R_B^\ell \approx R_B^0$ also. In other words, both V_B^ℓ and $\hbar\omega_\ell$ are obtained in terms of its ℓ=0 values, with V_B^0 given as the sum of nuclear proximity potential V_P and Coulomb potential V_C at $R = R_B^0$,

$$V_B^0 = V_P(R = R_B^0, A_i, \beta_{\lambda i}, E_{c.m.}, \theta_i) + V_C(R = R_B^0, Z_i, \beta_{\lambda i}, E_{c.m.}, \theta_i) \tag{2.54}$$

where $\beta_{\lambda i}$, λ=2,3,4 are the static quadrupole, octupole and hexadecapole deformations.

Using the above two approximations, and replacing the ℓ-summation in Eq. (2.49) by an integral, gives the fusion cross-section [52]

$$\sigma(E_{c.m.}, \theta_i) = \frac{{R_B^0}^2\hbar\omega_0}{2E_{c.m.}} \ln\left[1 + \exp\left(\frac{2\pi}{\hbar\omega_0}(E_{c.m.} - V_B^0)\right)\right], \tag{2.55}$$

Here, one may use the interaction between two deformed nuclei of radii R_i with deformation parameters $\beta_{\lambda i}$ and making orientation angles θ_i with respect to the collision axis(as shown in Fig. 2.3). Hence, the fusion cross-section integrated over the angles θ_i is obtained as

$$\sigma(E_{c.m.}) = \int_{\theta_i=0}^{\pi/2} \sigma(E_{c.m.}, \theta_i) sin\theta_1 d\theta_1 sin\theta_2 d\theta_2. \tag{2.56}$$

It is important to remind here that the characteristics of only the ℓ=0 barrier play role in Wong formula (2.55).

2.3.2 Extended Wong Model

In 2009, Gupta and collaborators [11] calculated the barrier characteristics (the barrier height, position as well as the oscillator frequency) for the case ^{48}Ca + ^{238}U (^{48}Ca being a spherical nucleus, only the deformations of ^{238}U comes into play) at various ℓ- values and noticed that angular momentum plays an important role in changing barrier characteristics as shown in Fig. 2 of Ref. [11]. Hence, the ℓ-summation is carried out in expression (2.49) explicitly, for the ℓ_{max} determined empirically for a best fit to the measured cross-section. In Wong formula, all the ℓ values are considered (however the barrier characteristics are considered for s-wave) and hence the cross-section may overestimate the experimental data particularly at higher incident energies. Therefore, one may opt to put an upper limit on ℓ-values so as to have reasonable addressal of data. The ℓ-dependent interaction potential V(R,T,ℓ) also denoted as V_T^ℓ, entering Eq. 2.51 via V_B^ℓ, $\hbar\omega_\ell$ and R_B^ℓ is given by Eq. 2.50, with moment of inertia in non-sticking limit. This procedure of explicit ℓ-summation works very well at above barrier energies where the fusion cross-section σ_{fus} is measured whereas it fails to reproduce the data at sub-barrier energies and, as in Misicu and Esbensen [74] for M3Y potential, demands modification of the barrier, which carry out here by various ways :

(i) keeping the curvature $\hbar\omega_\ell$ same and modifying the barrier height V_B^ℓ defined as

$$V_B^\ell(modified) = V_B^\ell + \Delta V_B^{emp},$$

(ii) keeping the barrier height V_B^ℓ same and modify the curvature $\hbar\omega_\ell$ as

$$\hbar\omega_\ell(modified) = \hbar\omega_\ell + \Delta\hbar\omega^{emp}.$$

(iii)either with the use of different Skyrme forces, giving different barrier characteristics in Semiclassical extended Thomas-Fermi (SEDF) approach or by using different proximity potentials. In this thesis, various versions of nuclear interaction potentials are used to modify the barrier for the best fit of fusion cross-section at below barrier region.

The main point of difference in the two models (DCM and Wong formula) is that in Wong formula, the pre-formation probability P_0=1 and penetrability is calculated by the Hill-Wheeler approximation [72] and the same in DCM is obtained by WKB integral. On the other hand preformation probability P_0 is used to address the formation probability of decaying fragments of CN state in DCM. As σ_{fus}=σ_{ER}+σ_{ff}; hence one may use DCM approach for treating total fusion cross-sections as well. Therefore one may assume that DCM is a generalized form of Wong formula in which we address individual cross-sections of various decay channels as well as the total fusion cross-sections, whereas Wong formula handles only the fusion cross-section.

It is worth noting that ℓ-summed Wong formula may also be named as “parabolic approximation” or “Hill-Wheeler method”. But as ℓ-summed Wong formula or extended-Wong formula notation is used in published articles so in the following chapters we use the same notation for the sake of consistency.

Bibliography

[1] R. K. Gupta, R. Kumar, N. K. Dhiman, M. Balasubraniam, W. Scheid, and C. Beck, Phys. Rev. C **68**, 014610 (2003).

[2] M. Balasubraniam, R. Kumar, R. K. Gupta, C. Beck, and W. Scheid, J. Phys. G **29**, 2703 (2003).

[3] R. K. Gupta, M. Balasubramaniam, R. Kumar, D. Singh, C. Beck, and W. Greiner, Phys. Rev. C **71**, 014601 (2005).

[4] B. B. Singh, M. K. Sharma, and R. K. Gupta, Phys. Rev. C **77**, 054613 (2008).

[5] M. K. Sharma, G. Sawhney, R. K. Gupta, and W. Greiner, J. Phys. G: Nucl. Part. Phys. **38**, 105101 (2011).

[6] M. K. Sharma, S. Kanwar, G. Sawhney, and R. K. Gupta, Phys. Rev. C **85**, 064602 (2012).

[7] M. Kaur, R. Kumar, and M. K. Sharma, Phys. Rev. C **85**, 014609 (2012).

[8] M. Kaur and M. K. Sharma, Phys. Rev. C **85**, 054605 (2012).

[9] K. Sandhu, M. K. Sharma, and R. K. Gupta, Phys. Rev. C **85**, 024604 (2012).

[10] D. Jain, R. Kumar, and M. K. Sharma, Phys. Rev. C **87**, 044612 (2013).

[11] R. Kumar, M. Bansal, S. K. Arun, and R. K. Gupta, Phys. Rev. C **80**, 034618 (2009).

[12] R. Kumar, M. K. Sharma, and R. K. Gupta, Nucl. Phys. A **870-871**, 42 (2011).

[13] D. Jain, R. Kumar, M. K. Sharma, and R. K. Gupta, Phys. Rev. C **85**, 024615 (2012).

[14] J. Maruhn and W. Greiner, Phys. Rev. Lett. **32**, 548 (1974).

[15] R. K. Gupta, W. Scheid and W. Greiner, Phys. Rev. Lett. **35**, 353 (1975).

[16] A. Săndulescu, R. K. Gupta, W. Scheid and W. Greiner, Phys. Lett. **60B**, 225 (1976).

[17] R. K. Gupta, A. Săndulescu and W. Greiner, Phys. Lett. **67B**, 257 (1977); Rev. Roum. Phys. **23**, 51 (1978).

[18] S. Yamaji, W. Scheid, H.J. Fink and W. Greiner, Z. Phys. **A 278**, 69 (1976).

[19] S. Yamaji, W. Scheid, H.J. Fink and W. Greiner, J. Phys. G: Nucl. Phys. **2**, L189 (1976).

[20] S. Yamaji, K. H. Ziegenhain, H.J. Fink, W. Greiner and W. Scheid, J. Phys. G: Nucl. Phys. **3**, 1283 (1977).

[21] R. K. Gupta, A. Săndulescu and W. Greiner, Z. Naturforsch. **32a**, 704 (1977).

[22] R. K. Gupta, C. Pirvulescu, A. Săndulescu and W. Greiner, Z. Phys. **A 283**, 217 (1977); Sovt. J. Nucl. Phys. **28**, 160 (1978).

[23] R. K. Gupta, Z. Physik. **A 281**, 159 (1977).

[24] A. Săndulescu, H. J. Lustig, J. Hahn, and W. Greiner, J. Phys. G: Nucl. Phys. **4**, L279 (1978).

[25] H. J. Lustig, J. A. Maruhn, and W. Greiner, J. Phys. G: Nucl. Phys. **6**, L25 (1980).

[26] H. J. Fink and W. Greiner and R. K. Gupta and S. Liran and J.H. Maruhn and W. Scheid and O. Zohni, in Proceedings of Int. Conf. on Reaction between Complex Nuclei, Nashville, 1974, 21, (Amsterdam: North Holland), pages 2.

[27] R. K. Gupta, IANCAS Bull. (India), **6**, 2 (1990).

[28] V. M. Strutinsky, Nucl. Phys. A **95**, 420 (1967).

[29] K. A. Brueckner, C. A. Levinson, and H. H. Mohmoud, Phys. Rev. **95**, 217 (1954).

[30] K. A. Brueckner, J. L. Gammel, and H. Weitzner, Phys. Rev. **110**, 431 (1958).

[31] K. A. Brueckner, A. M. Lockett, and M. Rotenberg, Phys. Rev. **121** 255 (1961).

[32] K. A. Brueckner, J. R. Buchler, and M. Kelley, Phys. Rev. **173**, 944 (1968).

[33] D. Vautherin and D. M. Brink, Phys. Rev. C **5**, 626 (1972).

[34] T. H. R. Skyrme, Phil. Mag. **1**, 1043 (1956); Nucl. Phys. **9**, 615 (1959).

[35] S. Kumar and R. K. Gupta, Phys. Rev. C **49**, 1922 (1994).

[36] R. K. Gupta, W. Scheid, and W. Greiner, J. Phys. G: Nucl. Part. Phys. **17**, 1731 (1991).

[37] R. K. Gupta, in *Heavy Elements and Related New Phenomena*, edited by W. Greiner and R.K. Gupta (World Scientific, Singapore, 1999), Vol. **II**, p. 730.

[38] B. B. Singh, M. K. Sharma, and R. K. Gupta, Phys. Rev. C **77**, 054613 (2008), and earlier references there in it.

[39] R. K. Gupta, Lecture Notes in Physics, 818 *Clusters in Nuclei*, ed C. Beck, Vol. I, (Springer Verlag) p 223 (2010).

[40] S. S. Malik and R. K. Gupta, Phys. Rev. C **39**, 1992 (1989).

[41] K. J. LeCouteur and D. W. Lang, Nucl. Phys. **13**, 32 (1959).

[42] M. Balasubraniam, R. Kumar, R. K. Gupta, C. Beck, and W. Scheid, J. Phys. G **29**, 2703 (2003).

[43] R. K. Gupta, R. Kumar, N. K. Dhiman, M. Balasubraniam, W. Scheid, and C. Beck, Phys. Rev. **C 68**, 014610 (2003).

[44] H. Kröger and W. Scheid, J. Phys. G **6**, L85 (1980).

[45] G. Audi and A. H. Wapstra, Nucl. Phys. A **595**, 4 (1995).

[46] P. Möller, J. R. Nix, W. D. Myers, and W. J. Swiatecki, At. Data Nucl. Data Tables **59**, 185 (1995).

[47] N. J. Davidson, S.S. Hsiao, J. Markram, H. G. Miller, and Y. Tzeng, Nucl. Phys. A **570**, 61c (1994).

[48] P. A. Seeger, Nucl. Phys. **25**, 1 (1961).

[49] R. K. Gupta, M. Balasubramaniam, R. Kumar, N. Singh, M. Manhas and W. Greiner, J. Phys. G: Nucl. Part. Phys. **31**, 631 (2005).

[50] M. Münchow, D. Hahn and W. Scheid, Nucl. Phys. **A388**, 381 (1982).

[51] M. J. Rhoades-Brown, V. E. Oberacker, M. Seiwert and W. Greiner, Z. Phys. **A310**, 287 (1983)

[52] C. Y. Wong, Phys. Rev. Lett. **31**, 766 (1973).

[53] J. Blocki, J. Randrup, W.J. Swiatecki, and C. F. Tsang, Ann. Phys. (N.Y.) **105**, 427 (1977).

[54] Deryagin, Kolloid Z. **69**, 155 (1934).

[55] R. K. Gupta, N. Singh, and M. Manhas, Phys. Rev. C **70**, 034608 (2004).

[56] G. Royer and J. Mignen, J. Phys. G: Nucl. Part. Phys. **18**, 1781 (1992).

[57] P. Möller and J. R. Nix, Nucl. Phys. A **361**, 117 (1981).

[58] W. Reisdorf, J. Phys. G: Nucl. Part. Phys. **20**, 1297 (1994).

[59] V. Y. Denisov, Phys. Lett. B **526**, 315 (2002).

[60] I. Dutt, and R. K. Puri, Phys. Rev. C **81**, 064609 (2010); *ibid* **81**, 064608 (2010).

[61] G. Royer and R. Rousseau, Eur. Phys. J. A **42**, 541 (2009).

[62] D. Jain, R. Kumar and M. K. Sharma, Nucl. Phys. A **915**, 106-124 (2013).

[63] B. K. Agrawal, S. Shlomo, and V. Kim Au, Phys. Rev. C **72**, 014310 (2005).

[64] B. K. Agrawal, S. K. Dhiman, and R. Kumar, Phys. Rev. C. **73**, 034319 (2006).

[65] M. Brack, C. Guet, and H.-B. Hakansson, Phys. Rep. **123**, 275 (1985).

[66] J. Friedrich and P.-G. Reinhardt, Phys. Rev. C **33**, 335 (1986).

[67] J. Bartel and K. Bencheikh, Eur. Phys. J. A. **14**, 179 (2002).

[68] J. Bartel, M. Brack and M. Durang, Nucl. Phys. A **445**, 263 (1985).

[69] L. R. B. Elton, *Nuclear Sizes* (Oxford University Press, London, 1961).

[70] H. de Vries, C. W. de Jager, and C. de Vries, At. Data Nucl. Data Tables **36**, 495 (1987).

[71] S. Shlomo and J. B. Natowitz, Phys. Rev. C **44**, 2878 (1991).

[72] D. L. Hill and J. A. Wheeler, Phys. Rev. **89**, 1102 (1953); T. D. Thomas, Phys. Rev. **116**, 703 (1959).

[73] V. E. Viola and T. Sikkeland, Phys. Rev. **128**, 767 (1962).

[74] S. Misicu and H. Esbensen, Phys. Rev. Lett. **96**, 112701 (2006).

Chapter 3

Use of various Skyrme forces in fusion- fission dynamics

3.1 Introduction:

In this Chapter, the role of different Skyrme forces is investigated in reference to fusion-fission dynamics by employing dynamical cluster-decay model (DCM) and the ℓ-summed Wong model, where the nuclear proximity potential is obtained by using the semiclassical extended Thomas Fermi (ETF) approach in Skyrme Energy Density Formalism (SEDF) under Frozen density approximation. Application of both these models with explicit angular momentum and barrier modification effects is made to fit the fusion excitation function for ^{132}Sn+^{64}Ni$\rightarrow$^{196}Pt*$\rightarrow$$A_1$+$A_2$ reaction. In addition to this, the comparative study of pocket formula due to Blocki *et al.* potential with Skyrme forces are also studied in the decay pattern of Pt* isotopes.

The formation and decay of a compound nucleus (CN) has been a topic of great interest for several decades as it provides useful information regarding fusion cross-section and its variation with incident center-of-mass energy $E_{c.m.}$, the fusion excitation functions. The compound nucleus, depending on its mass, disintegrates by emitting multiple light particles (the evaporation residues ER), followed by fission (the fusion-fission). Equivalently one may also experience the competing non-compound processes such as quasi-fission (qf) or deep inelastic collision (DIC) etc where the projectile- and target-like fragments are seen in the decay channel without proper equilibration at CN stage. Thus, for a compound nucleus reaction, the fusion cross-section is defined as the sum of the fusion-evaporation cross-section σ_{ER}, the fission cross-section σ_{fiss}, and the quasi-fission cross-section σ_{qf}. In 2008, an experiment was performed for producing the neutron-rich compound nucleus ^{196}Pt* by bombarding radioactive ^{132}Sn beam on ^{64}Ni, and the σ_{ER} and σ_{fiss} were measured [1]. Interestingly, *at sub-barrier energies*, only the ER cross-section is measured since fission data of ^{196}Pt* nuclear system was not reported. On the other hand, at the above-barrier energies, the qf component in fission cross-sections could not be separated because of the inverse kinematics of ^{132}Sn+^{64}Ni reaction and beam intensity being several orders of magnitude lower than that of the stable ^{112,118,124}Sn-beams. In view of the known unexpected behavior of the fusion-evaporation cross-sections at energies far below the Coulomb barrier, i.e., the fusion hindrance seen in the coupled channel calculations (ccc) [2,3], for some other Ni-induced reactions (^{58,64}Ni+^{58,64}Ni and ^{64}Ni+^{100}Mo), the experimental data on ^{132}Sn+^{64}Ni reaction [1] offered an interesting opportunity to study the fusion and fusion-fission dynamics with different theoretical models. Here, in the following, we carry out such a study by using the dynamical cluster-decay (DCM) of preformed clusters [4–8] and the ℓ-summed extended-Wong model [9, 10]. Further importance of this work is that it involves the neutron-rich radioactive beam and the nuclear structure effects, of the incoming nuclei and/ or decay products, are shown to influence the fusion cross-sections at near- and below-barrier energies.

In the present study, the use of different Skyrme forces in DCM is introduced for the first time via the nuclear proximity potential obtained [11] from semiclassical extended Thomas Fermi (ETF) approach in Skyrme energy density formalism (SEDF) [12–14] under frozen density approximation [15]. Compared to the nuclear proximity potential due to Blocki *et al.* [16], with fixed barrier height, position and curvature, the nuclear proximity potential derived from SEDF has the advantage of allowing the use of different Skyrme forces, having different barrier characteristics, for introducing "barrier modification" effect for the best fit to data via different Skyrme forces. In other words, Skyrme forces provide the flexibility for a better comparison of data, since a large number of them are available that fit different ground-state properties of nuclei from different mass regions.

More recently, the above said nuclear proximity potential [11], derived from SEDF-based ETF approach [10], has also been used in the ℓ-summed extended-Wong model [9], at above as well as below barrier energies, for studying the ER and capture cross-section of Ni- and Ca-induced reactions, respectively. The ℓ-summed extended-Wong model [9] is an extended version of Wong formula [17] where the angular momentum effects are explicitly included and is found to contain the barrier modification effects due to ℓ-dependent barriers. The barrier-modification or no barrier-modification at sub-barrier energies in ℓ-summed extended-Wong model is shown to depend not only on the choice of Skyrme force but also on the type of reaction under investigation. The σ_{ER} of the considered Ni-based reactions (^{58,64}Ni+^{5864}Ni and ^{64}Ni+^{100}Mo) at sub-barrier energies required different Skyrme forces for the best fit to data. In view of above discussion the ^{132}Sn+^{64}Ni$\rightarrow$^{196}Pt* reaction is also investigated via ℓ-summed extended-Wong model [9] using the Skyrme-force-based nuclear proximity potential [11].

In this Chapter, the comparative analysis of three Skyrme forces, namely SIII, GSkI and SSk is explored by investigating ^{132}Sn+^{64}Ni reaction on DCM and ℓ-summed Wong model. The effect of using different Skyrme forces on "barrier lowering" at sub-barrier energies in ER data is studied using DCM approach. Beside this, the qf contribution in fission data is predicted at higher center-of-mass energies $E_{c.m.}$, which increases with decrease in barrier height due to different Skyrme forces. Furthermore, the extended-Wong Model is applied to ^{132}Sn+^{64}Ni reaction showing different nature of fits for different Skyrme forces, i.e., just as for other Ni-based reactions (^{58,64}Ni+^{58,64}Ni and ^{64}Ni+^{100}Mo) [10], whereas the GSkI and SSk forces fit the data without any barrier adjustment, the force SIII needs the same for the best fit at below-barrier energies.

One question which may come in mind that why do we have so many Skyrme forces and whether some of them are better than the others including interaction like that of Blocki *et al.*. Since stronger isospin effects are needed for tackling the steep fall of the cross-sections at below Coulomb barrier energies [18], the recent parameterizations GSkI and SSk provide the appropriate isospin effects, whereas the older SIII parameterization and Blocki *et al.* potential are less sensitive towards neutron-proton asymmetry and isospin effects. Also the old Skyrme force parameterization SIII differs from the very recent GSkI and SSk forces in their containing the tensor coupling with spin and the gradient terms. In addition, the GSkI force also includes the three density-dependent interactions, discussed in the next section.

The chapter is organized as follows. The calculations and discussion of results are presented in Section 3.2. The calculations are done by considering nuclei to be in the same plane, and deformations are included up to hexadecapole deformations (β_2-β_4) with optimum orientations $\theta^{opt.}$ [19] in DCM, but the same integrated in the case of extended-Wong Model [10]. Note that $\theta^{opt.}$ are only for quadrupole deformations (β_4=0). Finally, conclusions are given in Section 3.3.

3.2 Calculations and discussion of the results

The calculations have been done for the fusion-evaporation residues and fusion-fission of ^{196}Pt* compound nucleus using the DCM, and the total fusion cross-section using the ℓ-summed extended-Wong model, with nuclear proximity potential obtained from SEDF-based ETF method for three illustrative Skyrme forces GSkI, SSk and SIII, and compared with Blocki *et al.* potential [5]. These forces cover a large range of the barrier characteristics (V_B, R_B and $\hbar\omega$). The effects of orientations

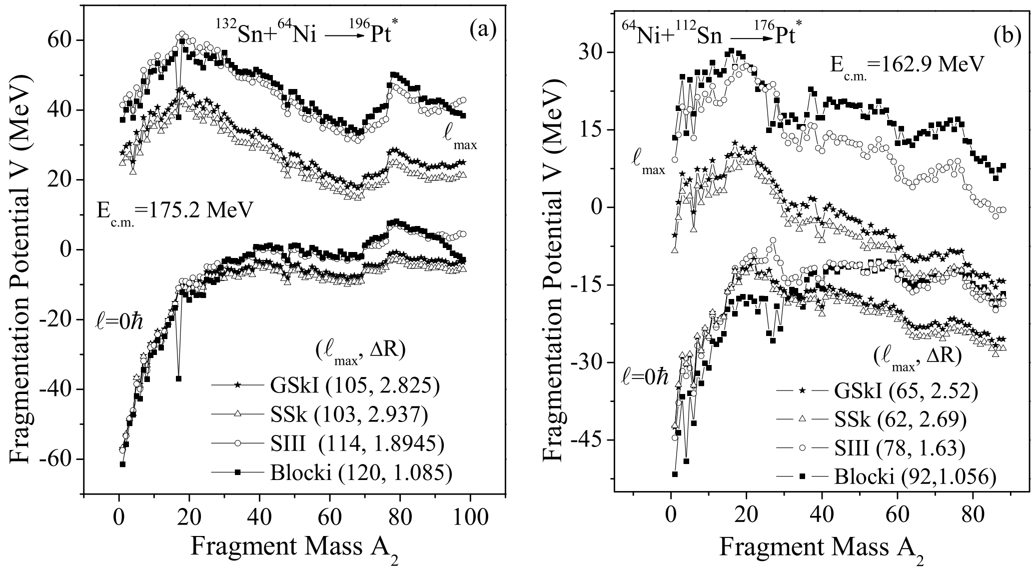

Figure 3.1: (a) Fragmentation potential $V(A_2)$ for the decay of compound nucleus ^{196}Pt*, plotted at $\ell = 0$ and ℓ_{max} values, using different Skyrme forces and compared with Blocki *et al.* interaction from [5]. (b) Same as for (a) but for the compound nucleus ^{176}Pt*.

and deformations are included, as mentioned in the Introduction.

3.2.1 Decay of ^{196}Pt* using the DCM

First of all, the fragmentation potentials $V(A_2)$ for the three Skyrme forces, compared with the potential due to Blocki *et al.*, plotted in Fig. 3.1(a) for $\ell = 0$ and ℓ_{max} cases. It is to be noticed that the forces GSkI (solid line with star) and SSk (solid line with hollow triangle) behave nearly alike since, for both the forces, same fragments contribute to the decay processes. Also ℓ_{max} values are close to each other (see columns 3 and 4 in Table 6.1), and the potential energy minima are stronger at the asymmetric fragments rather than the symmetric fragments. The same is true for SIII (solid line with hollow circle) and Blocki *et al.* (solid line with rectangle) potential, except that the later one also favors a contribution from symmetric mass distribution (the minimum at A/2 is relatively deeper). The contribution of asymmetric fragments for SIII force is similar to other two Skyrme forces (GSkI and SSk), the difference being only in the magnitude. In other words, for all the four cases, the potential energy minima are stronger at the asymmetric fragments rather

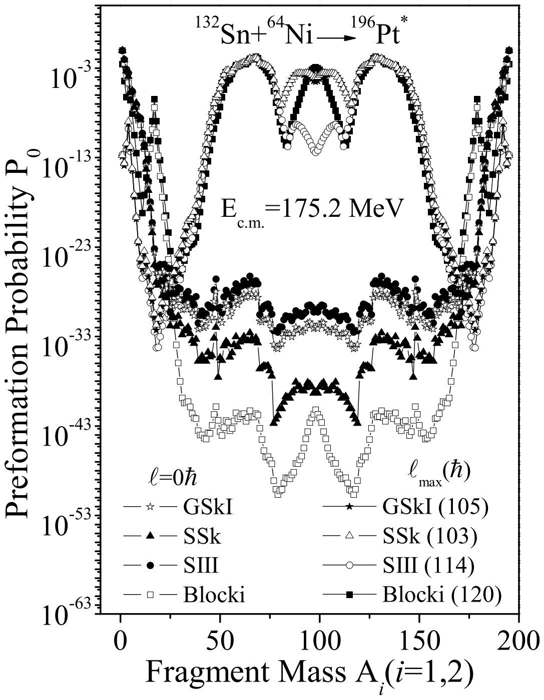

Figure 3.2: Preformation probability P_0 as a function of fragment mass A_i corresponding to the fragmentation potential in Fig. 3.1(a).

than the symmetric fragments. One may also notice that at $\ell = 0$, for all the four interactions, the contribution of ER is more prominent as compared to the symmetric or asymmetric fission fragments, whereas at $\ell = \ell_{max}$, the fission fragments start competing with ER, the lighter fragments.

After that the role of changing the radioactive ^{132}Sn beam to a stable ^{112}Sn beam have been tested by calculating the fragmentation potential for ^{176}Pt*, using all the three Skyrme forces and Blocki *et al.* potential, as shown in Fig. 3.1(b). The interesting result is that there is a noticeable change in the structure of $V(A_2)$ by adding/ subtracting 20 neutrons, i.e., the predominantly asymmetric fission distribution for ^{196}Pt* changes to a predominantly symmetric one for ^{176}Pt*, independent of the choice of nuclear interaction potential. Such a change in fission mass distribution provides the possibility to study the fine-/ or sub-structure in fission products of Pt* isotopes. The isospin analysis in Pt* nuclei is worked out in Chapter 4.

The above results from fragmentation potentials can be better understood in terms of preformation factor P_0, plotted in Fig. 3.2 as a function of A_2. We notice

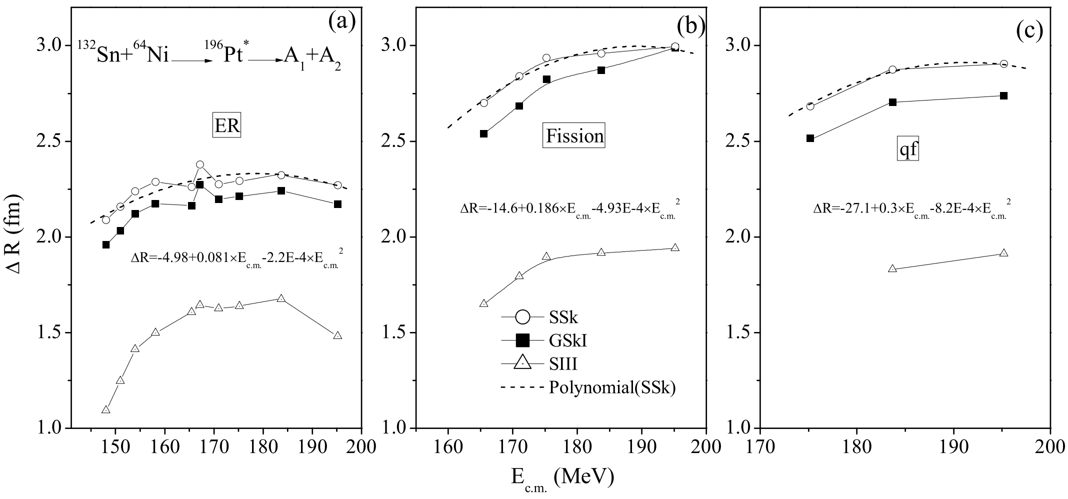

Figure 3.3: The neck-length parameter ΔR plotted as a function of $E_{c.m.}$ for (a) ER, (b) fission, and (c) qf process, using the Skyrme forces SSk (solid line with hollow circle), GSkI (solid line with rectangle) and SIII (solid line with hollow triangle).

from Fig. 3.2 that, in the decay of ^{196}Pt* at $\ell = \ell_{max}$, the contribution of asymmetric fragment (AF) component is predominant for all the four interactions considered. The preformation factors for GSkI (solid line with star) and SSk (solid line with hollow triangle) forces are overlapping with each other, indicating the preformation of the same (asymmetric and symmetric) fragments for the two forces. Interestingly for all the interactions, the AF component is nearly the same. The calculations are made within the fitting of one parameter, the "neck length" parameter ΔR, for each chosen force, given in Table 6.1 and Fig. 3.3 for all the three processes of ER, fission and qf. The use of neck-length parameter assimilates the effects of both deformations of decaying fragments and neck formation between them. This method of introducing the neck length parameter ΔR is also used in the scission-point [20] and saddle-point [21] (statistical) fission models for decay of a hot and rotating compound nucleus. Generally the different ΔR values for competing decay channels are associated with the time scale of emission of a particular channel. The ΔR in a way modifies the first turning point of barrier penetration, referring to the actually used

Table 3.1: The ER and fission cross-sections for ^{196}Pt* system, calculated on the DCM at different $E_{c.m.}$'s for various Skyrme forces, compared with the experimental data [1]. The upper-limit of ER cross-section at $E_{c.m.}$=142.5 MeV, included in Fig. 3.8, is not included here. The quasi-fission (qf) contribution in fission is also calculated, wherever required.

$E_{c.m.}$	T	$\ell_{max}(\hbar)$			ΔR (fm)			σ (mb)			
(MeV)	(MeV)								DCM		Expt.
		SSk	GSkI	SIII	SSk	GSkI	SIII	SSk	GSkI	SIII	
					Evaporation Residue (ER)						
195.2	1.9944	108	110	120	2.271	2.173	1.481	259	259	260	259
183.7	1.8556	102	104	113	2.322	2.24	1.6753	253	251	257	251.4
175.2	1.7458	103	105	114	2.293	2.213	1.637	265	265	265	264.8
171	1.6889	101	103	113	2.275	2.197	1.625	218	219	218	218
167.2	1.6357	92	96	111	2.3794	2.274	1.643	235	235	234	234
165.5	1.6113	100	102	111	2.261	2.163	1.607	184	184	183	184
158.1	1.5004	89	92	108	2.288	2.175	1.498	70	70.2	70	70
154	1.4353	86	90	107	2.239	2.12	1.412	31.5	31.3	32	31.5
151	1.3856	82	86	106	2.159	2.033	1.247	5.08	5.03	4.87	5±1
148.1	1.3359	77	82	105	2.089	1.96	1.093	0.7	0.7	0.67	0.7±0.2
					Fission and predicted Quasi-fission (qf)						
195.2	1.9944	108	110	120	2.996	2.989	1.94	189.4	224	224	544
					2.904	2.739	1.876	352^1	321^1	318^1	
183.7	1.8556	102	104	113	2.959	2.871	1.94	177.6	200	230	371
					2.875	2.704	1.83	194^1	171^1	140^1	
175.2	1.7458	103	105	114	2.937	2.825	1.8945	208	212	230	232.9
					2.682	2.515		25.2^1	21.2^1		
171	1.6889	101	103	113	2.8403	2.685	1.793	142.8	141.2	139.4	138
165.5	1.6113	100	102	111	2.701	2.539	1.649	31	31.4	31.4	31.2

^{1}symbolizes quasi-fission (qf) contribution.

barrier height and consequently introduces the concept of barrier modification which helps us to account for the fusion hindrance effect at sub-barrier energies, something similar to coupled channel calculations. In other words, the DCM approach is used to address the hindrance phenomenon in terms of the 'modified shape of potential barrier' at sub-barrier energies in a simple way via its fitting of the neck-length parameter. The dependence of ΔR is shown in Fig. 3.3 which follows the second order polynomial as a function of $E_{c.m.}$ for SSk force and the similar trend is followed by other forces (not shown in graph).

Fig. 3.4 shows the comparison of experimental data [1] on σ_{ER} and σ_{fiss} with DCM based calculations for the three Skyrme forces (a) GSkI, (b) SSk, and (c) SIII,

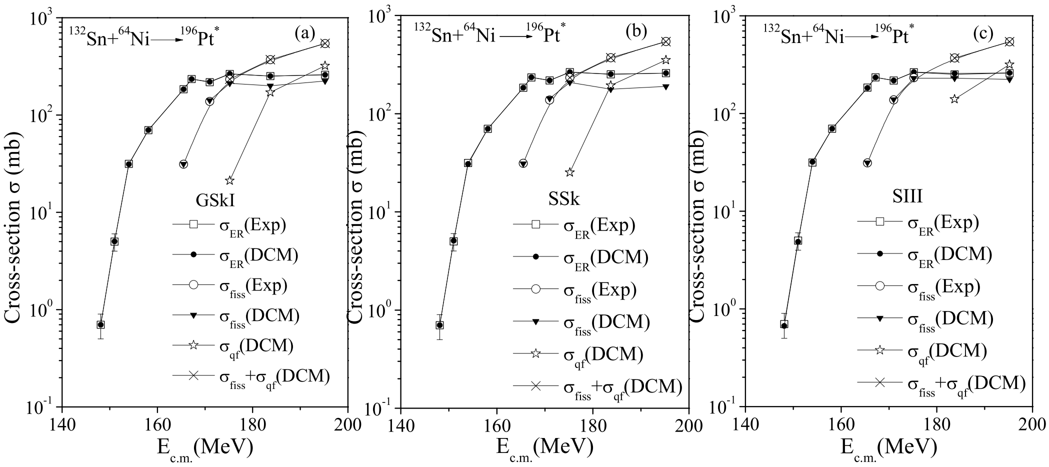

Figure 3.4: Comparison of experimental evaporation residue σ_{ER} and fission cross-section σ_{fiss} for ^{132}Sn+^{64}Ni reaction [1] with calculations made in DCM, using the three Skyrme forces (a) GSkI, (b) SSk, and (c) SIII.

for the neck length parameter ΔR obtained in each case as plotted in Fig. 3.3. Apparently the fits obtained are good for σ_{ER}, but the fission data at the highest two/ or three center of mass energies $E_{c.m.}$ did not fit for either of the Skyrme force. At these higher $E_{c.m.}$ values, the qf process seems to compete with the fission and the sum of these two, i.e. $\sigma_{fiss} + \sigma_{qf}$, fits the available data nicely. It is to be noticed that for GSkI and SSk forces, qf content appears at highest three $E_{c.m.}$ values whereas, similar to Blocki *et al.* potential [5], for SIII force, it comes into picture only at the two highest energies. In other words, for each Skyrme force, the DCM stresses the presence of a non-compound, qf-content in fission cross-sections at above-barrier energies.

Fig. 3.5 shows the variation of "barrier lowering" parameter ΔV_B as a function of $E_{c.m.}$ for the chosen three Skyrme forces, in case of $\ell = \ell_{max}$ for mass one particle, i.e. (A_2=1). It is clear from Fig. 3.5 that ΔV_B increases (i.e. becomes more negative) for below-barrier energies and its contribution increases for the force with a higher barrier. Fig. 3.6 shows that the barrier is highest for SIII force (solid line), and hence in Fig. 3.5 the "barrier lowering" ΔV_B at sub-barrier energies is largest for SIII force. In fact, ΔV_B is another representation of the neck-length parameter ΔR. It may be relevant to note that the hump in the values of ΔR for ER at $E_{c.m.}$=167.2

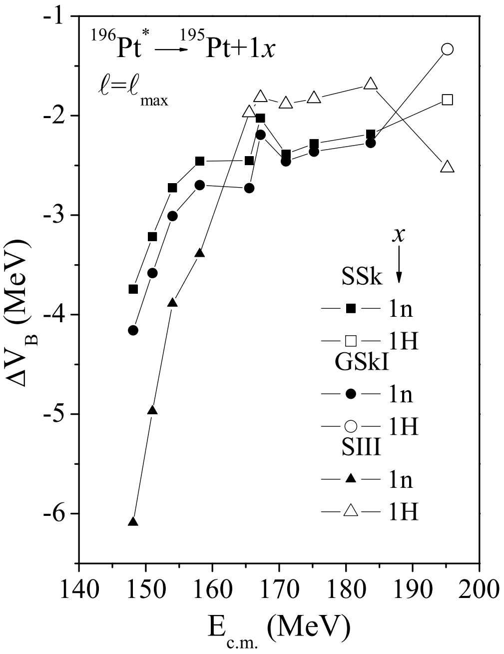

Figure 3.5: Barrier-lowering parameter ΔV_B as a function of $E_{c.m.}$ for mass one particle at $\ell = \ell_{max}$ for SSk, GSkI, and SIII Skyrme forces.

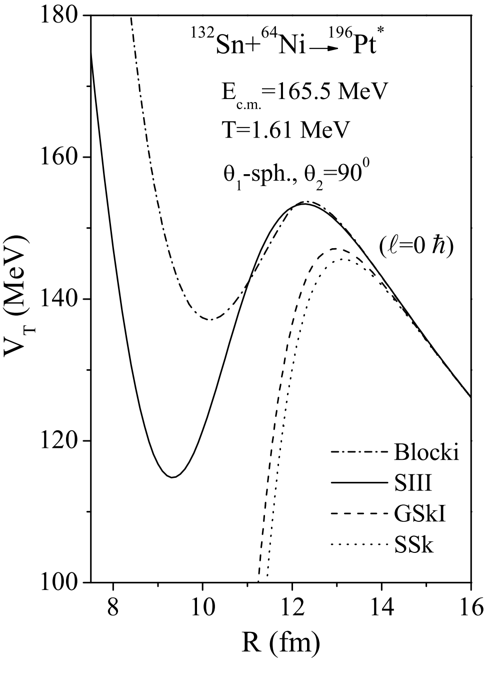

Figure 3.6: Interaction potentials $V(R)$ of ^{132}Sn+^{64}Ni for the three Skyrme forces and Blocki *et al.* potential at fixed $E_{c.m.}$ and θ_i values for co-planar nuclei (Φ=0^0).

MeV in both the Figs. 3.3(a) and 3.5 represents the absence of data point in fission at this energy.

3.2.2 Fusion cross-sections for ^{196}Pt* using ℓ-summed extended-Wong model

The fusion cross-section is the sum of ER and fission cross-sections, to which the extended-Wong model is applicable for a best fit to determine the ℓ_{max} value. The barrier characteristics (V_B^ℓ, R_B^ℓ and $\hbar\omega_\ell$), that are extracted from the scattering potentials at all the angles (co-planer in present study) and ℓ-values up to ℓ_{max}, are the main inputs in the Wong model. Fig. 3.6 shows the total interaction potential for ^{132}Sn+^{64}Ni→^{196}Pt* at fixed $E_{c.m.}$ and θ_i's for ℓ=0 case. Fig. 3.7 shows the variation of barrier height V_B with $E_{c.m.}$ for ℓ=0 case of the same reaction, using all the potentials calculated in Fig. 3.6. It is clear from Figs. 3.6 and 3.7 that the barrier characteristics of the SIII parameterization and that of Blocki *et al.* are similar, and hence the results associated with these interactions are also close to each other. Similarly, the barrier characteristics of GSkI and SSk parameterizations are also close to each other, and, hence, so also are their results.

Fig. 3.8(a) shows the fusion excitation function, i.e., the calculated fusion cross-section as a function of center-of-mass energy $E_{c.m.}$ for ^{132}Sn+^{64}Ni reaction using the three illustrated Skyrme forces in extended-Wong model, compared with the experimental data [1]. Apparently, the extended-Wong model calculations for GSkI and SSk forces fit the data nicely at both above- as well as below-barrier energies, but the SIII force does not fit the data for below-barrier energies, and hence needs the “barrier modifications” to be included in order to fit the data. The corresponding deduced ℓ_{max} values, for the best possible fits of fusion cross-sections with the three Skyrme forces used in Fig. 3.8(a), are presented in Fig. 3.8(b). Notice that ℓ_{max} as a function of $E_{c.m.}$ vary smoothly for best fitted GSkI and SSk forces, but for the SIII force, where the fit is not so good at sub-barrier energies, the $\ell_{max}(E_{c.m.})$

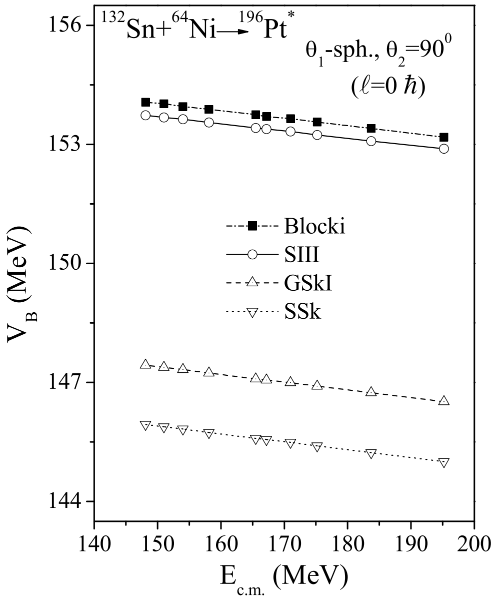

Figure 3.7: Barrier height V_B as a function of $E_{c.m.}$ for ^{132}Sn+^{64}Ni, using the three Skyrme forces SIII (solid line), GSkI (dashed line) and SSk (dotted line), and the Blocki *et al.* (dashed-dot line) potential at fixed θ_i values for co-planar nuclei (Φ=0^0).

varies erratically which could certainly be smoothed by adding appropriate "barrier lowering" or "barrier narrowing" empirically.

It may be noted that the significant difference between the predications of the older (SIII) and the modern forces (GSkI and SSk), arises due to the different barrier characteristics. As shown in Fig. 3.7, the $E_{c.m.}$ dependence of the barrier height V_B for recent forces is ∼7 MeV lower as compared to the older SIII or Blocki *et al.* force. Similar behavior is presented by the other two barrier properties (R_B and $\hbar\omega$) of these forces (not shown here). Since these barrier properties are the main ingredient of the Wong model, so the comparison in the data is better for new Skyrme forces with lower barriers.

3.3 Conclusions

The decay pattern of CN ^{196}Pt* formed in ^{132}Sn+^{64}Ni reaction is investigated using DCM where temperature, deformation and orientation effects are dully incorporated. The fusion cross-sections are also calculated independently by using the ℓ-summed

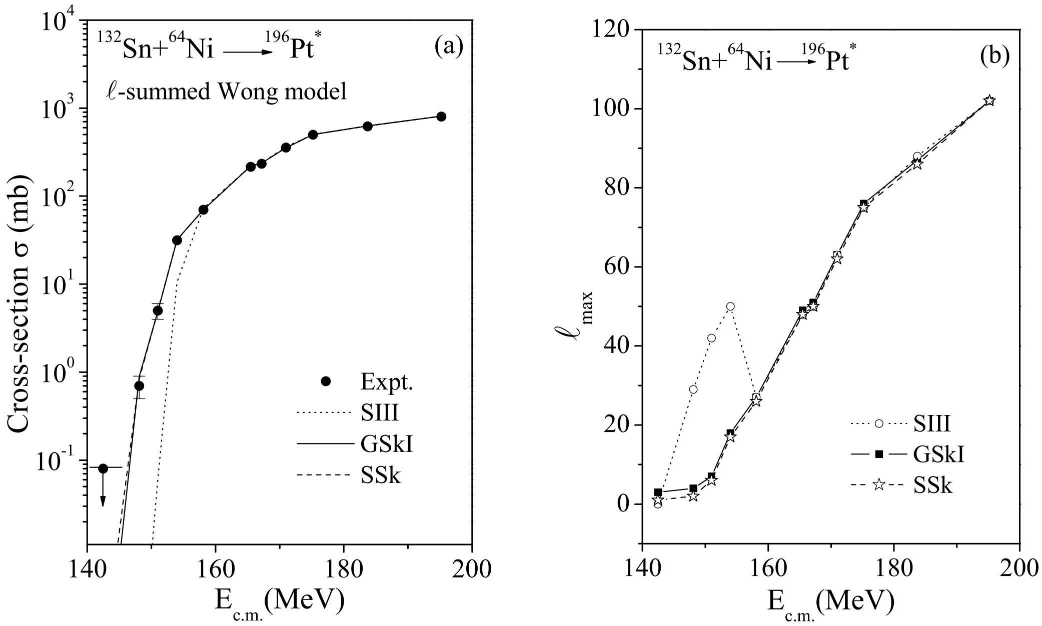

Figure 3.8: (a) Fusion excitation functions of ^{132}Sn+^{64}Ni→^{196}Pt* using the extended-Wong model, and (b) deduced ℓ_{max} values *vs.* $E_{c.m.}$, using the Skyrme forces SIII (dotted line), GSkI (solid line) and SSk (dashed line).

extended-Wong Model. Both the model calculations use the nuclear proximity potential derived from SEDF-based semiclassical ETF method with densities added under frozen-density approximation.

Within the DCM, it is found that for the chosen three Skyrme forces GSkI, SSk and SIII, the decay process presents the same pattern for the fragmentation potential as well as the pre-formation probability, indicating that the asymmetric fission contributes more than the symmetric fission. For all the Skyrme forces, the ER process contributes more at lower ℓ values, whereas the fission fragments starts competing with ER as the ℓ value increases. However, the predominantly asymmetric pattern changes to the symmetric one with decrease of N/Z ratio of the CN, leading to the possibility to address the isospin effects in Pt* nuclei. The reversal of behavior of fission fragments, i.e. from asymmetric to symmetric, with decrease in N/Z ratio holds good for a variety of nuclear interaction potentials used for studying the reaction dynamics of Pt-isotopes. Another interesting result is that "barrier lowering" is required for ER cross-sections at sub-barrier energies, and the fission cross-sections show the necessity of qf contribution at the highest two/ three energies, depending on the Skyrme force used.

The ℓ-summed extended-Wong model fits the total fusion cross-section (sum of ER and fission cross-sections) for the Skyrme forces GSkI and SSk, with proper dependence of deduced ℓ_{max} on $E_{c.m.}$, not requiring any additional "barrier lowering" or "barrier narrowing" for a best fit to data. However, the force SIII demands barrier modification as the corresponding deduced ℓ_{max} in this case varies erratically or unphysically with $E_{c.m.}$. Interestingly, the ℓ-summed extended-Wong model fits the high energy fusion cross-section data nicely, without any explicit knowledge of qf component, whereas the same can be worked out exactly in the framework of the DCM. Note that qf component could not be separated out experimentally in this reaction, and the prediction of qf at the highest two/ three energies calls for a further experimental verification.

Concluding, as the reaction under study involves the neutron-rich radioactive ^{132}Sn beam, the old Skyrme force SIII and Blocki *et al.* potential require barrier modification, because in the fitting of parameters of the SIII force, the isospin effect was not taken into the account and also Blocki *et al.* potential is less sensitive towards the isospin. However, the Skyrme forces GSkI and SSk are improved with respect to the recent experimental data, and the parameters of these forces are determined by fitting several properties of some normal and isospin rich nuclei. Therefore, the GSkI and SSk forces are expected to perform better for the isospin rich colliding nuclei, like the one under investigation. In other words, the dynamics of a system can be explained by using the appropriate Skyrme force whose parameters are fitted for the region to which it belongs. In the next chapter we intend to explore the isotopic dependance of Pt* nuclei using stable and radioactive Sn beams in order to have further understanding regarding dynamics of Sn based nuclear reactions.

Bibliography

[1] J. F. Liang *et al.*, Phys. Rev C **75**, 054607 (2007); J. F. Liang *et al.*, *ibid.* **78**, 047601 (2008).

[2] C. L. Jiang *et al.*, Phys. Rev C **71**, 044613 (2005); C. L. Jiang *et al.*, Phys. Rev Lett. **93**, 012701 (2004).

[3] S. Misicu and H. Esbensen, Phys. Rev. Lett. **96**, 112701 (2006); Phys. Rev. C **75**, 034606 (2007).

[4] R. K. Gupta, Lecture Notes in Physics 818, *Clusters in Nuclei*, ed C. Beck, Vol. I, (Springer Verlag, 2010) p 223.

[5] M. K. Sharma, S. Kanwar, G. Sawhney, R. K. Gupta, and W. Greiner, J. Phys. G: Nucl. Part. Phys. **38**, 055104 (2011).

[6] S. K. Arun, R. Kumar, and R. K. Gupta, J. Phys. G: Nucl. Part. Phys. **36**, 085105 (2009).

[7] R. K. Gupta, S. K. Arun, R. Kumar, and M. Bansal, Nucl. Phys. A **834**, 176c (2010).

[8] R. K. Gupta and M. Bansal, Int. Rev. Phys. (IREPHY) **5**, 74 (2011).

[9] R. Kumar, M. Bansal, S. K. Arun, and R. K. Gupta, Phys. Rev. C **80**, 034618 (2009).

[10] R. Kumar, M. K. Sharma, and R. K. Gupta, Nucl. Phys. A **870-871**, 42 (2011); R. Kumar and R. K. Gupta, J. Phys.: Conf. Ser. **312**, 082025 (2011).

[11] R. K. Gupta, D. Singh, R. Kumar, and W. Greiner, J. Phys. G: Nucl. Part. Phys. **36**, 075104 (2009).

[12] B. Grammoticos and A. Voros, Ann. Phys. **123**, 359 (1979); *ibid.* **129**, 153 (1980).

[13] M. Brack, C. Guet, and H. -B. Hakansson, Phys. Rep. **123**, 275 (1985).

[14] J. Bartel and K. Bencheikh, Eur. Phys. J. A **14**, 179 (2002).

[15] G. -Q. Li, J. Phys. G: Nucl. Part. Phys. **17**, 1 (1991).

[16] J. Blocki, J. Randrup, W. J. Swiatecki, and C.F. Tsang, Ann. Phys. (N.Y.) **105**, 427 (1977).

[17] C. Y. Wong, Phys. Rev. Lett. **31**, 766 (1973).

[18] R. Kumar, Phys. Rev. C **84**, 044613 (2011).

[19] R. K. Gupta, M. Balasubramaniam, R. Kumar, N. Singh, M. Manhas, and W. Greiner, J. Phys. G: Nucl. Part. Phys. **31**, 631 (2005).

[20] T. Matsuse, C. Beck, R. Nouiser, and D. Mahboub, Phys. Rev. C **55**, 1380 (1997).

[21] S. J. Janders, Phys. Rev. C **44**, 2676 (1991).

Chapter 4

Isotopic analysis of Pt* nuclei formed using stable and radioactive Sn beams

4.1 Introduction

In previous chapter, the role of Skyrme forces and its comparison with pocket formula has been studied in fusion-fission process. Here in present chapter, the role of various nuclear proximity potentials and level density parameter is investigated in reference to the entrance channel effect of CN ^{190}Pt* formed in ^{132}Sn+^{58}Ni and ^{126}Sn+^{64}Ni reactions with in the framework of DCM. Beside this deformation effects and fusion hindrance phenomenon is also investigated within the framework of DCM [1]- [8] and ℓ-summed Wong model [9]- [11].

In recent years, the low-intensity neutron-rich radioactive ion beams (RIBs) have been used quite extensively to study the reaction dynamics. Due to the excess neutrons in RIBs, neutron transfer reactions are supposed to influence the fusion rate strongly and hence shed light on various ingredients of nuclear reaction dynamics and related phenomena. In recent past numerous experiments have been performed using the RIBs to study the evaporation residue and fusion-fission cross-sections and comparisons are made with the reactions involving stable beams [12,13]. Simultaneously significant amount of information is extracted through theoretical calculations as well. In 2012, experiment was performed using the stable and radioactive beams of different isotopes of Sn [14]. To observe the effect of additional neutrons on fusion probability and fusion hindrance, the ER cross-sections have been measured for chain of neutron-rich radioactive ^{126,127,128}Sn+^{64}Ni and ^{132}Sn+^{58}Ni reactions [14]. The fusion hindrance was shown to decrease with increase of neutron excess in Sn beams.

The main aim of the work presented in this chapter is to study the reaction dynamics of various isotopes of Pt^{*}, formed using stable and radioactive ion beams of Sn with in the framework of DCM. In the process some useful information is extracted in reference to entrance channel, barrier modification, deformations and fusion hindrance etc. The consistency of entrance channel independence is checked, at approximately same center-of-mass energy ($E_{c.m.}$) and same maximum value of angular momentum (ℓ_{max}), using different nuclear proximity potentials i.e. Prox 1977 [15], Prox 1988 [16], mod-Prox 1988 [17], Denisov 2002 [18,19] and level density parameters, a=A/8, A/9, A/10. The barrier characteristics change considerably with the use of proximity potential. Henceforth, for fitting the data, different values of neck-length parameter ΔR are required. The neck length parameter (ΔR) represents the reaction time scale and is the only parameter of DCM which also refers to the actually used barrier height and consequently to the concept of barrier lowering ΔV_B. On changing level density parameter from a=A/8 to A/10, ΔR decreases which means that the barrier-lowering parameter ΔV_B increases, but in all cases same fragments are preborn during the decay process which indicates that CN forgets its history of formation. It is also observed that at ℓ=ℓ_{max} the fission mass distribution, changes from symmetric to asymmetric one and the α- nucleus structure starts vanishing with an increase in the N/Z ratio of the CN. The DCM based calculations reveal that the barrier lowering parameter (ΔV_B) decreases as

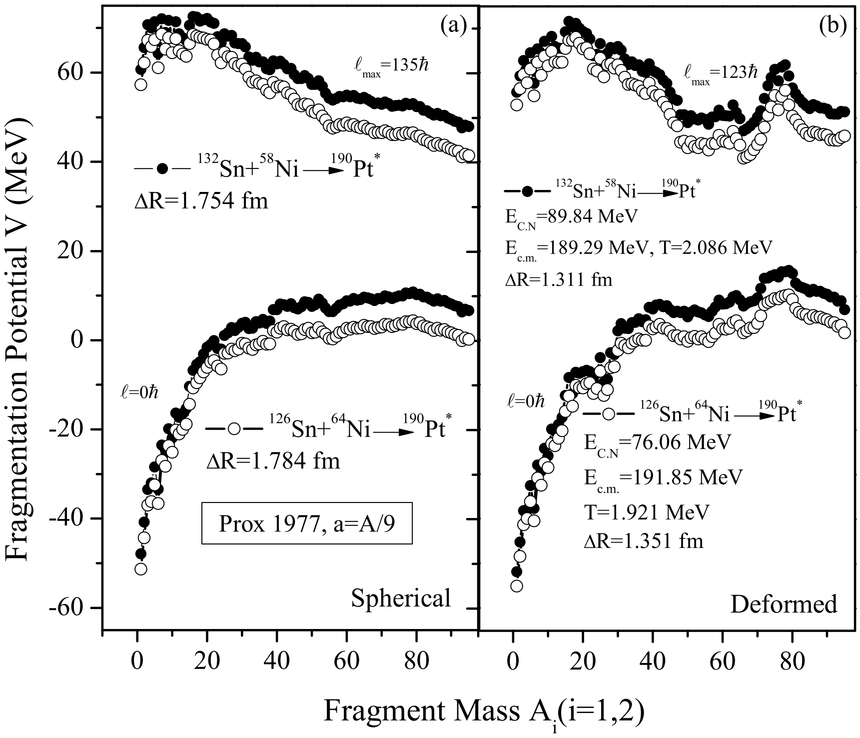

Figure 4.1: Fragmentation potentials V(A_2) for the decay of ^{190}Pt* formed in ^{132}Sn+^{58}Ni and ^{126}Sn+^{64}Ni reaction channel at comparable $E_{c.m.}$ values using (a) spherical and (b) deformation considered.

neutron excess in the projectile/target increases. In other words, fusion hindrance decreases with increasing neutron in CN and is in agreement with the experimental observation of [14].

Alternatively, extended-Wong model [9]- [11] is also used to make a possible comment on the fusion hindrance. The extended-Wong model is an extended version of the Wong formula [20], where the angular momentum effects are explicitly included and are found to contain the barrier modification effects due to ℓ-dependent potential barriers.

The chapter is organized as follows. The calculations and results are presented in Section 4.2. Finally, the conclusions drawn are discussed in Section 4.3.

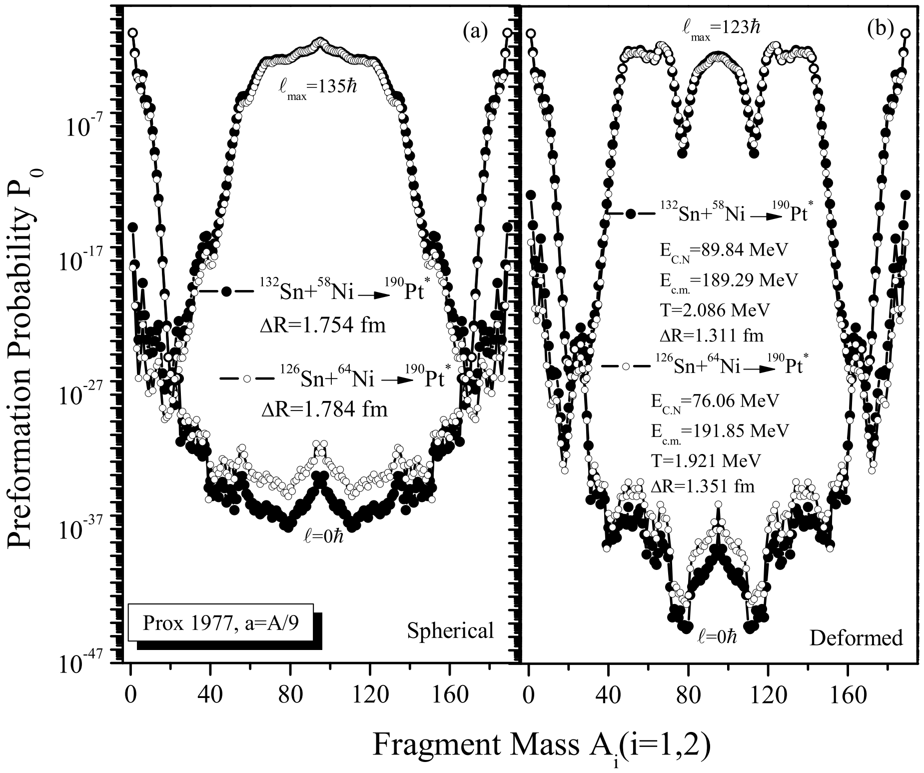

Figure 4.2: Preformation probability P_0 as a function of fragment mass A_i for the decay of ^{190}Pt* formed in ^{132}Sn+^{58}Ni and ^{126}Sn+^{64}Ni reaction channels at approximately same $E_{c.m.}$ values for level density parameters a=A/9 using (a) spherical and (b) deformation considered.

4.2 Calculations and Results

In section 4.2.1, the reaction dynamics of the decay of Pt^* CN, formed with different Sn-beams, is studied using the DCM with spherical and deformed choice of decaying nuclei. Then the effect of entrance channel on ^{190}Pt* compound nucleus formed in ^{126}Sn+^{64}Ni and ^{132}Sn+^{58}Ni reactions is studied where the role of different nuclear proximity potentials and level densities are also tested. Further the effect of increase in N/Z ratio of CN is investigated and consequently the fragmentation behavior and barrier modification effects are analyzed. The role of different proximity potentials with in the ℓ-summed extended Wong model, for the fusion cross-section of ^{132}Sn+^{58}Ni reaction is studied in Sec. 4.2.2. The concept of fusion hindrance is duly addressed in Sec. 4.2.3 in context of barrier characteristics and finally the results are summarized in Sec. 4.3.

Table 4.1: The ER cross-sections and relevant variables for ^{188,190,191,192}Pt* system formed via ^{132}Sn+^{58}Ni and ^{124,126127,128}Sn+^{64}Ni, calculated with the DCM at different $E_{c.m.}$'s for level density parameter a=A/9, compared with the experimental data [14].

								σ_{ER} (mb)	
$E_{c.m.}(MeV)$	E^*_{CN} (MeV)	T (MeV)	$\ell_{max}(\hbar)$	$V_B(\ell=0)$	$R_B(\ell=0)$	ΔR (fm)	ΔV_B (MeV)	DCM	Expt.
			^{124}Sn+^{64}Ni $\rightarrow$ $^{188}Pt^*$ $\rightarrow$ A_1+A_2						
183.60	66.10	1.804	117	158.12	11.886	1.785	-2.8	171	170.90±7
194.03	76.50	1.937	118	157.90	11.89	1.750	-3.015	135	136.80±6
201.29	86.70	2.062	120	157.68	11.912	1.732	-3.145	121	121.75±6
207.62	90.10	2.101	121	157.63	11.915	1.725	-3.19	113	113.80±5
211.00	93.49	2.139	121	157.55	11.921	1.734	-3.141	120	120.80±6
213.78	96.26	2.170	121	157.51	11.925	1.730	-3.178	115	116.30±5
217.87	100.36	2.215	122	157.42	11.929	1.728	-3.196	111	113.50±5
			^{126}Sn+^{64}Ni $\rightarrow$ $^{190}Pt^*$ $\rightarrow$ A_1+A_2						
181.7	65.9	1.792	120	157.62	12.366	1.376	-3.783	182	176.68±9
191.8	76.0	1.921	123	157.45	12.465	1.351	-4.027	178.9	178.4±8
202.0	86.2	2.044	124	157.28	12.538	1.325	-4.294	161.0	161.43±8
205.4	89.6	2.084	125	157.22	12.557	1.317	-4.374	156	157±8
212.1	96.3	2.159	126	157.08	12.59	1.306	-4.505	143.5	144.44±7.5
215.51	99.72	2.197	127	157.03	12.616	1.294	-4.624	134.9	134.42±8
			^{127}Sn+^{64}Ni $\rightarrow$ $^{191}Pt^*$ $\rightarrow$ A_1+A_2						
180.7	65.8	1.785	120	157.07	12.211	1.52	-2.737	181	183.04±9
190.9	76.0	1.916	123	157.08	12.291	1.45	-3.238	191	189.75±8
200.9	86.0	2.037	125	157.04	12.452	1.376	-3.849	161	162.55±7.5
204.3	89.4	2.077	126	156.99	12.519	1.357	-4.014	157	158.9±9
211.1	96.2	2.152	127	156.88	12.560	1.34	-4.189	153	152.85±8.5
214.4	99.5	2.189	128	156.82	12.598	1.318	-4.389	138	136.8±9

Continued 1 .... Table 4.1

$E_{c.m.}(MeV)$	E^{*}_{CN} (MeV)	T (MeV)	$\ell_{max}(\hbar)$	$V_B(\ell=0)$	$R_B(\ell=0)$	ΔR (fm)	ΔV_B (MeV)	σ_{ER} (mb)	
								DCM	Expt.
				^{128}Sn+^{64}Ni $\rightarrow$ $^{192}Pt^{*}$ $\rightarrow$ A_1+A_2					
180.10	65.97	1.782	124	156.9	12.238	1.505	-2.785	249	250.4±11
190.15	76.02	1.911	127	156.96	12.353	1.418	-3.452	202	200.9±9
200.29	86.15	2.033	128	156.84	12.469	1.376	-3.808	201	201.8±10
203.61	89.48	2.071	128	156.782	12.499	1.37	-3.879	182	184.3±8
207.00	92.87	2.109	130	156.74	12.567	1.342	-4.104	176	178.2±9
210.33	96.20	2.147	131	156.69	12.597	1.325	-4.26	164	165.5±8
214.35	100.22	2.190	132	156.62	12.621	1.315	-4.39	162	160.3±10
				^{132}Sn+^{58}Ni $\rightarrow$ $^{190}Pt^{*}$ $\rightarrow$ A_1+A_2					
166.40	66.9	1.805	120	156.57	12.494	1.315	-4.301	115	115.41±4
171.60	72.1	1.872	121	156.45	12.479	1.335	-4.149	146.4	146.18±5
177.20	77.7	1.942	123	156.35	12.502	1.332	-4.184	161.48	161.33±6
189.20	89.8	2.086	123	156.16	12.592	1.311	-4.429	160.62	160±6
194.58	95.1	2.146	126	156.07	12.629	1.305	-4.505	153.94	153.2±7
197.07	97.6	2.174	127	156.02	12.638	1.3055	-4.504	155	157±8

4.2.1 Decay of Pt^* formed using stable and radioactive Sn-beams using DCM

In this section, the variation of fragmentation potential V(η) and preformation probability P_0 is studied in order to see whether the decay of CN ^{190}Pt* is dependent or independent of its mode of formation. The barrier-lowering effect due to fusion hindrance is also studied. Fig. 4.1 shows the calculated fragmentation potentials for the decay of ^{190}Pt*, formed in ^{132}Sn+^{58}Ni and ^{126}Sn+^{64}Ni reaction at the extreme values of angular momentum i.e. at ℓ=0 and ℓ_{max}, with spherical and deformed choice of decaying nuclei. In order to do a comparison between the two incoming channels, the same centre-of-mass energy $E_{c.m.} \approx 190$ MeV is chosen. At ℓ=0$\hbar$, the fragmentation potentials are quite similar for spherical and deformed choices of the fragmentation. However at ℓ_{max}, the structure of potential energy surfaces changes significantly, particularly with the inclusion of deformation and orientation effects i.e. the fragmentation is symmetric for spherical nuclei and becomes asymmetric when deformation effects are included.

It is clear from Fig. 4.1 that the decay pattern of CN $^{190}Pt^*$ remains similar for both the channels, with some difference in magnitude only. It may be noted that at ℓ=0, the contribution of the ER is more prominent than the symmetric or asymmetric fission fragments, which otherwise start appearing at higher ℓ-values. These results are in agreement with the decay of ^{196}Pt* investigated using Skyrme forces and reported in Chapter 3. Fig. 4.2 shows the calculated preformation probability for the decay of $^{190}Pt^*$ at same ℓ_{max} value and comparable $E_{c.m.}$ values for both the channels using spherical and deformed choices of nuclei. At ℓ_{max}, the preformation probability curve changes from symmetric to asymmetric as we go from spherical to deformed fragmentation. On the other hand the preformation factor overlap each other (same fragments pre-born during the decay process) for both the channels, which indicate that the decay is independent of the choice of the entrance channel. This observation holds good for spherical as well as deformed choice of

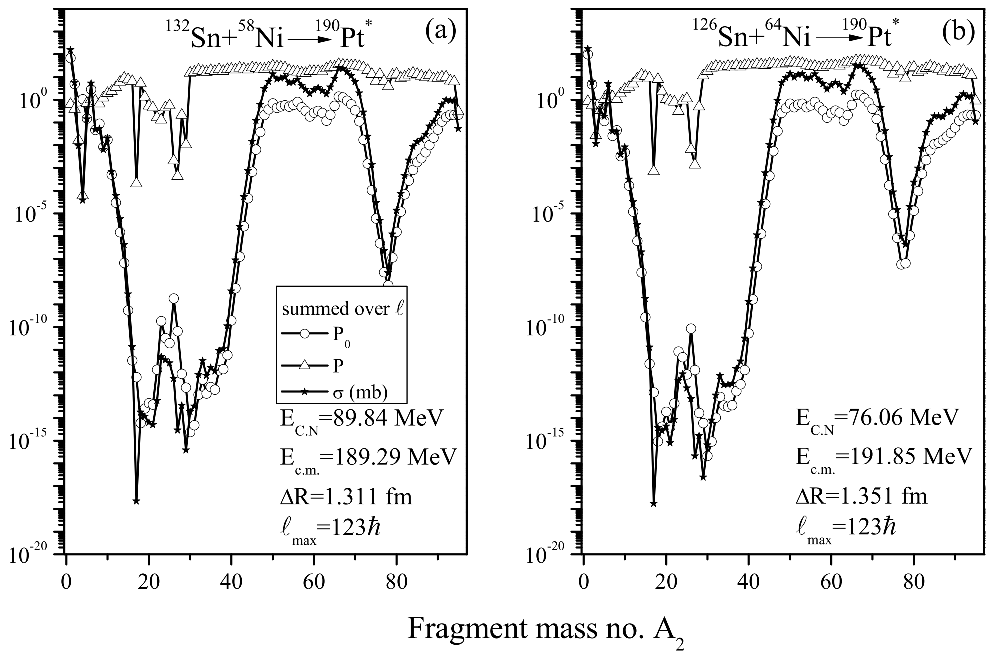

Figure 4.3: The ℓ-summed P_0, P and cross-section (σ) for the decay of $^{190}Pt^*$ as a function of light fragment mass A_2 at approximately similar $E_{c.m.}$ for (a) ^{132}Sn+^{58}Ni and (b) ^{126}Sn+^{64}Ni reactions.

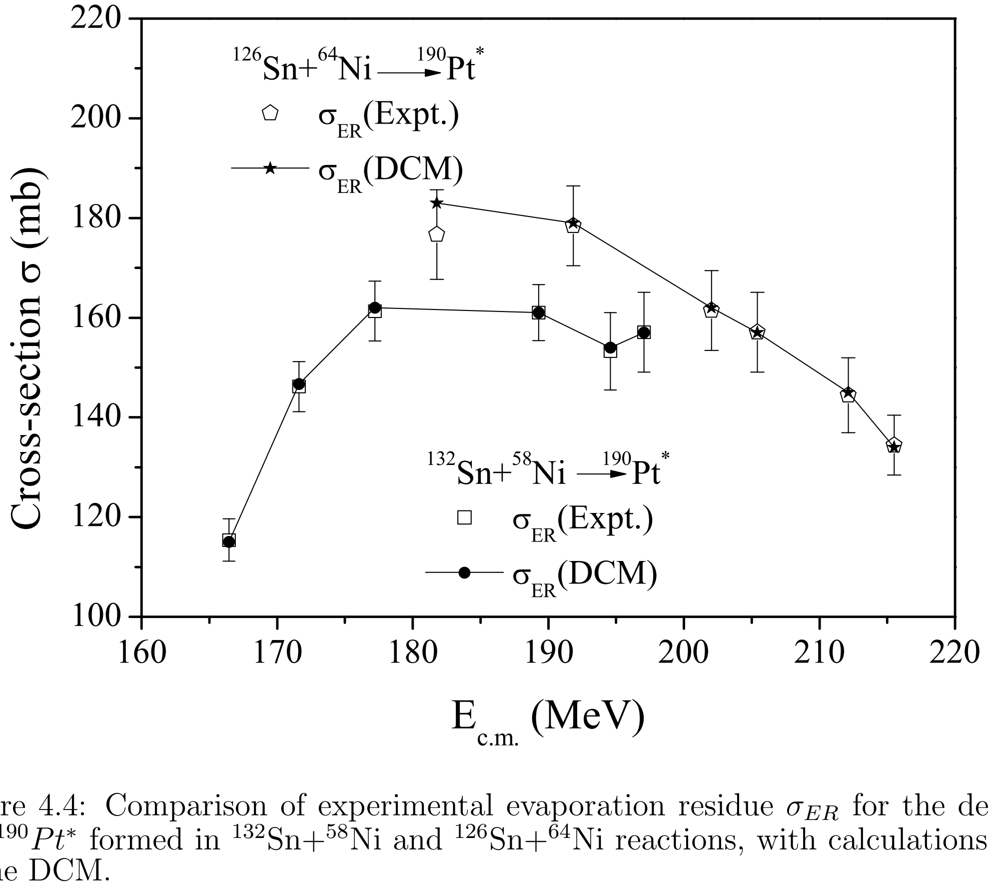

Figure 4.4: Comparison of experimental evaporation residue σ_{ER} for the decay of CN $^{190}Pt^*$ formed in ^{132}Sn+^{58}Ni and ^{126}Sn+^{64}Ni reactions, with calculations made in the DCM.

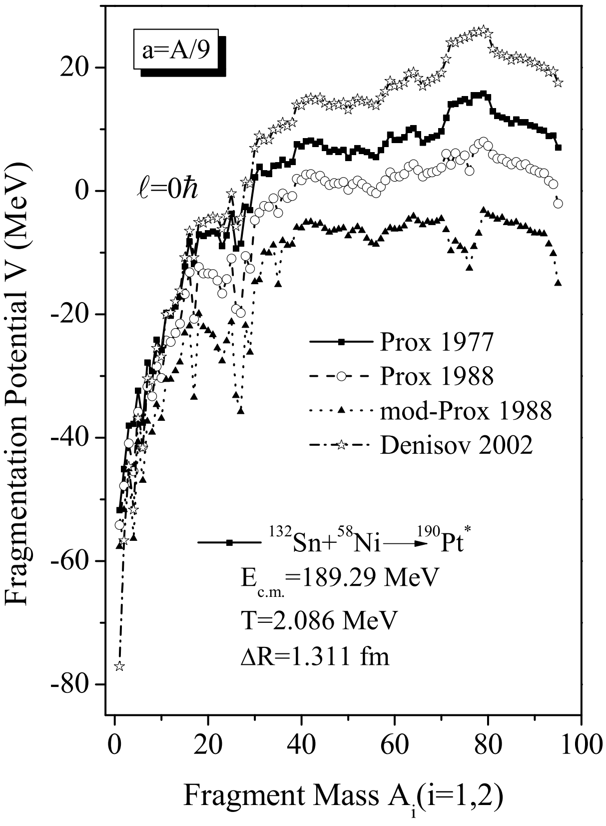

Figure 4.5: Fragmentation potentials V(A_2) for the decay of ^{190}Pt* formed in ^{132}Sn+^{58}Ni reaction channel at a given $E_{c.m.}$. using different proximity potentials considered.

fragmentation. The DCM based calculations indicate that fragmentation behavior of ER, intermediate mass fragments (IMF), heavy mass fragments (HMF) and fission fragments is almost identical i.e. independent of the choice of entrance channel.

Figure 4.3 show the ℓ-summed P_0, P and cross-section (σ), as a function of the fragment mass number A_2 for the ^{126}Sn+^{64}Ni and ^{132}Sn+^{58}Ni channels forming the CN at comparable $E^*_{c.m.}$=191.85 and 189.29 MeV respectively. It is relevant to mention here that in DCM, the decay cross-sections in terms of the ℓ-partial waves are defined as the product of preformation probability (P_0) and penetrability (P) for ℓ-value from 0 to ℓ_{max}. The ℓ-summed P_0 represents the sum of preformation probability of all contributing angular momentum states for a particular fragment that is preborn during the decay process. Similarly the ℓ-summed P means the sum of penetrability of the particular fragment over all the ℓ-values taken into consideration

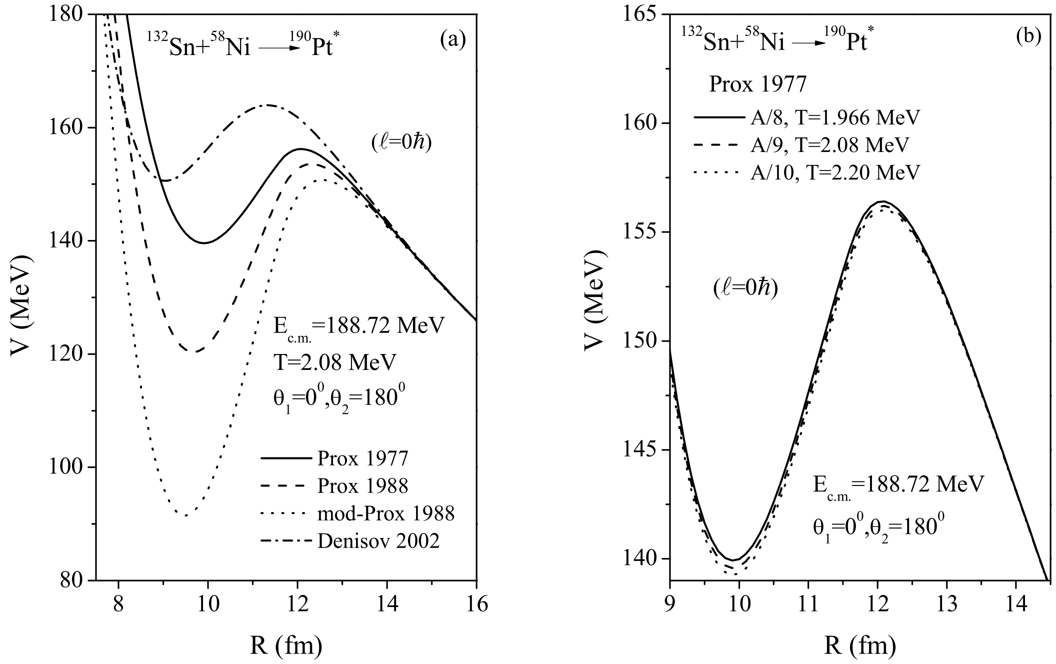

Figure 4.6: Total interaction potentials V(R) of ^{132}Sn+^{58}Ni for (a) the proximity potentials Prox 1977, Prox 1988, mod-Prox 1988 and Denisov 2002 and (b) level density parameters A/8, A/9 and A/10 for the case of Prox 1977, at $E_{c.m.}$=188.72 MeV for ℓ=0 case.

during the decay process. From the Fig. 4.3, it is clear that (i) cross-sections follow the trend of preformation probability P_0, which means that structure effects are contained only in P_0, (ii) P contributes largely to magnitude and almost no structure effects except for IMF and HMF region, (iii) the summed values of P_0, P and σ over ℓ are almost similar for both the reactions which indicates that using Prox 1977 with level density parameter A/9, there is no significant signature of entrance channel effects.

Figure 4.4 illustrates the DCM-calculated ER cross-section (σ_{ER}) for both the reactions, compared with the experimental data [14]. The calculated σ_{ER} fits the data nicely with in one parameter fit of ΔR which is shown in Table 4.1, at all the reported energies. The neck length parameter (ΔR) represents the reaction time scale and is the only parameter of DCM which also refers to the actual used barrier height and consequently to the concept of barrier lowering ΔV_B. The increase in ΔR

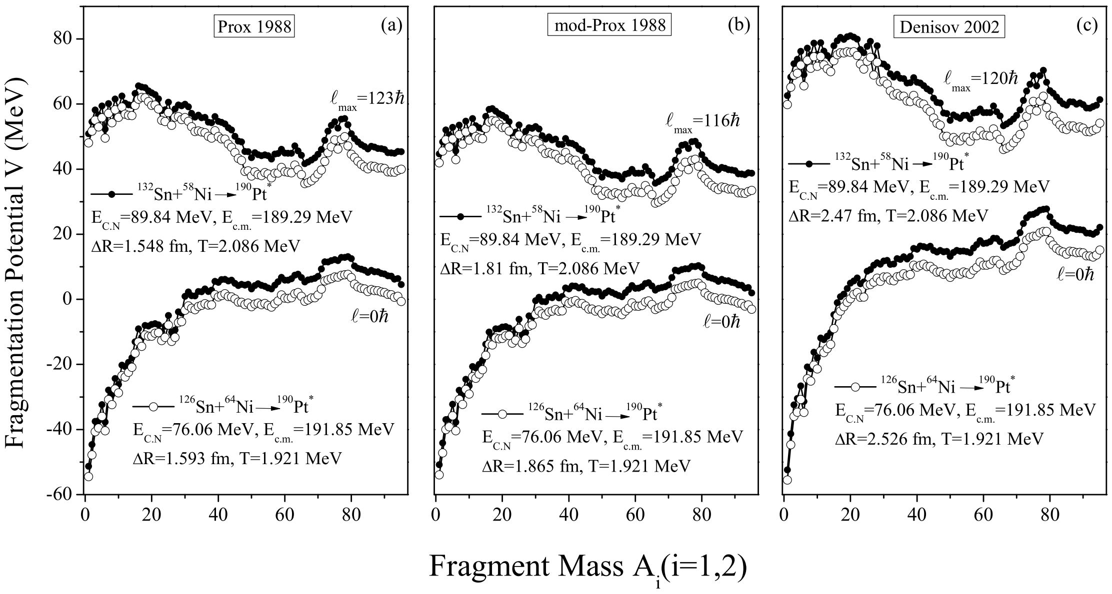

Figure 4.7: Same as Fig. 4.1 but for (a) Proximity 1988, (b) mod-Prox 1988 and (c) Denisov 2002.

means that the reaction time decreases and that, by definition, the barrier-lowering parameter ΔV_B decreases.

The entrance channel independence is further tested with the use of different nuclear proximity potentials Prox 77, Prox 88, mod-Prox 88 and Denisov 2002. The change of level density parameter is also exercised. Fig. 4.5 shows the decay pattern of CN $^{190}Pt^*$ formed using radioactive beam of ^{132}Sn on ^{58}Ni for different proximity potentials at ℓ=0, keeping other variables same. The decay pattern almost remains similar for the considered nuclear proximity potentials except some difference in magnitude and some variation in fission region.

It is to be noted that the both symmetric and asymmetric fragments contribute for the choice of Prox 88 and mod-Prox 88 potentials whereas other considered potentials favor symmetric fragmentation only. Fig. 4.6(a) shows the comparison of scattering potentials for the different nuclear proximity potentials and Fig. 4.6(b) shows the scattering potentials for different level density parameters. It may be noted that the proximity potentials used in Fig. 4.6(a) cover wide range of barrier characteristics. On the other hand change of level density parameter shown in

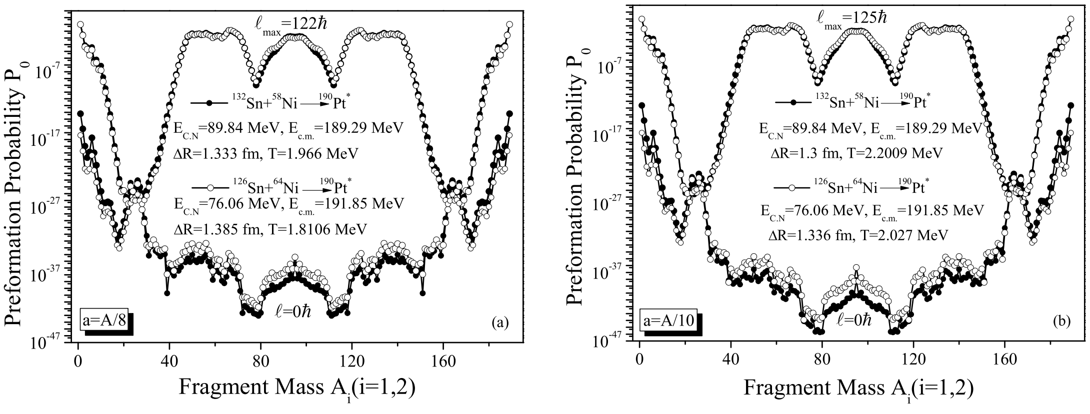

Figure 4.8: Same as Fig. 4.2 but for level density (a) A/8 and (b) A/10.

Fig. 4.6(b) don't influence the barrier characteristics significantly and hence play relatively silent role. It is observed from Fig. 4.7 that the maximum value of angular momentum ℓ_{max} remains same for both the incoming channels. This result sustains despite the use of different nuclear proximity potential, which rules out the angular momentum dependence on entrance channel of $^{190}Pt^*$ nucleus. In other words it is observed that the decay pattern of CN $^{190}Pt^*$ remains similar for both the channels independent of proximity potentials used. The case of Prox 1977 is shown in the Fig. 4.1. Since different nuclear proximity potentials corresponds to different barrier characteristics, so different values of the neck-length parameter (ΔR) are required to fit the ER cross-section. However for both the channels same fragments contribute to the decay process, indicating that the decay is independent of the mode of its formation. This result is clarified further in Fig. 4.8, showing the variation of preformation probability, that on decreasing the level density parameter from A/8 to A/10 for both the channels, temperature increases and hence neck length parameter (ΔR) decreases for ^{132}Sn+^{58}Ni and ^{126}Sn+^{64}Ni channels but decay pattern remains same which shows that even on changing level density parameter the decay of CN is independent of its path of formation. The case of level density of A/9 is shown in Fig. 4.2. It is to be noted here that change in ΔR-value for the cases of different proximity potentials and level density parameters, leads to corresponding change

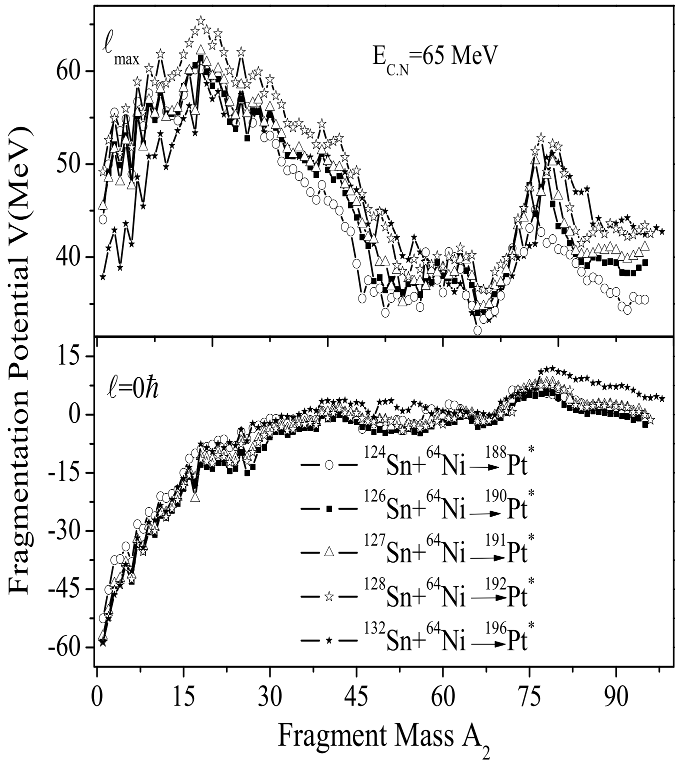

Figure 4.9: Fragmentation potential V(A_2) for the decay of $^{188,190,191,192,196}Pt^*$ nuclei, plotted for ℓ=0ħ (below)and ℓ_{max} (above) values.

in the magnitude of the barrier lowering parameter (ΔV_B) only and overall result remains the same.

Further the ER cross-sections is available for ^{124,126,127,128}Sn + ^{64}Ni reactions [14]. So these reactions are also analyzed systematically for the fission mass distribution with the increase in the iso-spin ratio N/Z of the decaying CN as shown in Fig. 4.9 at two extreme ℓ-values. Since, in Fig. 4.9 we have analyzed the reaction with ^{64}Ni target, so the case of ^{58}Ni with ^{132}Sn is not shown here. Instead, the earlier investigated reaction ^{132}Sn + ^{64}Ni [21], is shown for the sake of comparison and analysis of isotopic dependance of Pt nuclei. It is to be noted here that all the beams are radioactive except ^{124}Sn, which is stable. It is evident from Fig. 4.9 that the fragmentation potential V(A_2) at ℓ=ℓ_{max}, in the decay of $^{188}Pt^*$ formed from stable beam ^{124}Sn, both symmetric and asymmetric fission fragments do contribute. However on moving from the stable beam ^{124}Sn case to the radioactive beam ^{132}Sn, the prominent contribution is from the asymmetric fission only. Such variation towards

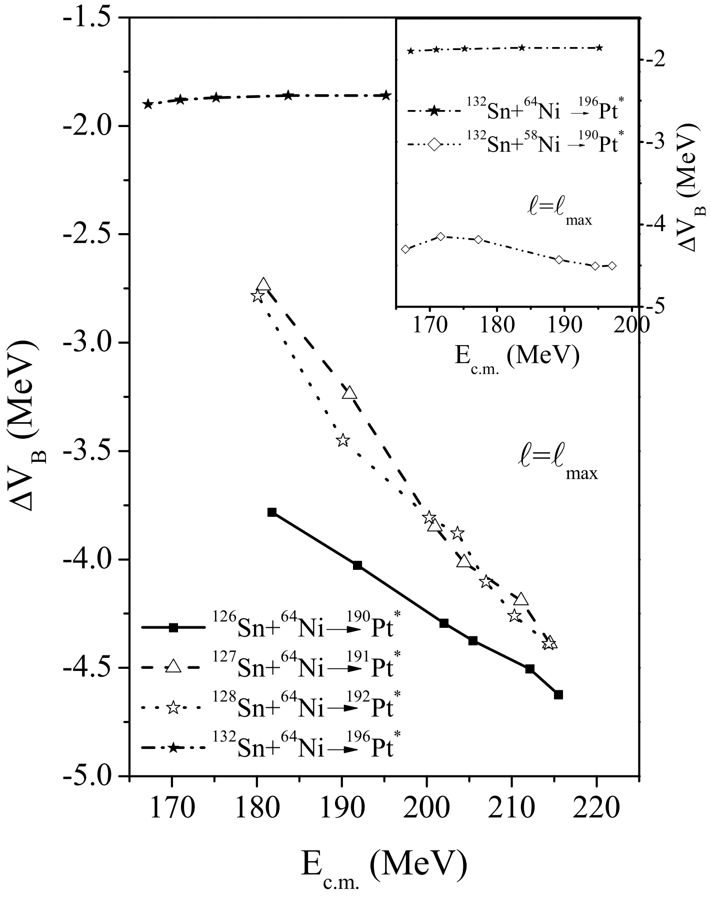

Figure 4.10: Barrier-lowering parameter ΔV_B as a function of $E_{c.m.}$ for the decay of $^{190,191,192,196}Pt^*$ nuclei at ℓ=ℓ_{max}. Inset shows the barrier modification for the reaction of ^{132}Sn with ^{58,64}Ni targets.

asymmetric fragmentation with increase in neutrons in Sn beam is visible only at higher ℓ- values, and the fragmentation profile at ℓ=0 do not change much. Such a change in fission mass distribution at higher ℓ- values, provides the possibility of studying the fine- or sub- structure in fission products of Pt^* isotopes. The knowledge of such sub-structuring of fission fragments is of huge interest as fragments contributing towards fission cross-sections are being identified in some recent experiments. The fitted ER cross-section and relevant variables are listed in Table 4.1 along with the experimental data [14].

Figure 4.10 shows the variation of the barrier lowering ΔV_B as a function of $E_{c.m.}$ for the decay of $^{190,191,192,196}Pt^*$ formed using radioactive Sn-beams and target of ^{64}Ni. Inset of the Fig. 4.10 shows the same but for the beam of ^{132}Sn with targets of ^{58,64}Ni. As the neutrons are increased either in radioactive projectile beam (Sn) or in target Ni, barrier lowering parameter ΔV_B decreases. This observation is explored in context of fusion hindrance phenomena in Sec. 4.2.3. In order to see the trend of barrier modification for radioactive beams, the CN formed using stable Sn beam i.e. the ^{188}Pt* is not included in the discussion of Fig. 4.10. Moreover, for ER consideration, the energetically favoured fragment is $1n$ in case of $^{188}Pt^*$ and ^1H for remaining cases dealt using radioactive beams.

4.2.2 Fusion cross-sections for ^{190}Pt* using ℓ-summed extended-Wong model

Experimentally, the fusion excitation functions for radioactive ^{132}Sn+^{58}Ni were measured [22] at energies across the Coulomb barrier which offers an opportunity to study the fusion hindrance phenomenon by using different proximity potentials with in ℓ-summed extended-Wong model. It is to be noted that out of all the other reaction under study, the total fusion cross-section for ^{132}Sn+^{58}Ni is available, so this reaction is studied using ℓ-summed extended-Wong model. Different proximity potentials have different barrier characteristics, which are extracted from the scattering potentials. Fig. 4.6(a) shows the total interaction potential for ^{132}Sn+^{58}Ni at $E_{c.m.}$=188.72 MeV for the ℓ=0 case, using various versions of nuclear proximity potentials. Fig. 4.11 shows the variation of barrier height V_B with $E_{c.m.}$ for the ℓ=0 case of the same reaction, using four potentials used in Fig. 4.6(a) It is clear from the Fig. 4.6(a) that the barrier characteristics, i.e., barrier height (V_B), position (R_B), and frequency ($\hbar\omega$), change considerably for the use of different proximity interactions. These potentials are considered here as they cover a wide range of barrier characteristics. The mod-Prox 1988, having stronger isospin effects, is also tested here. This potential corresponds to the most attractive potential, and hence the lowest barrier, out of the four considered here.

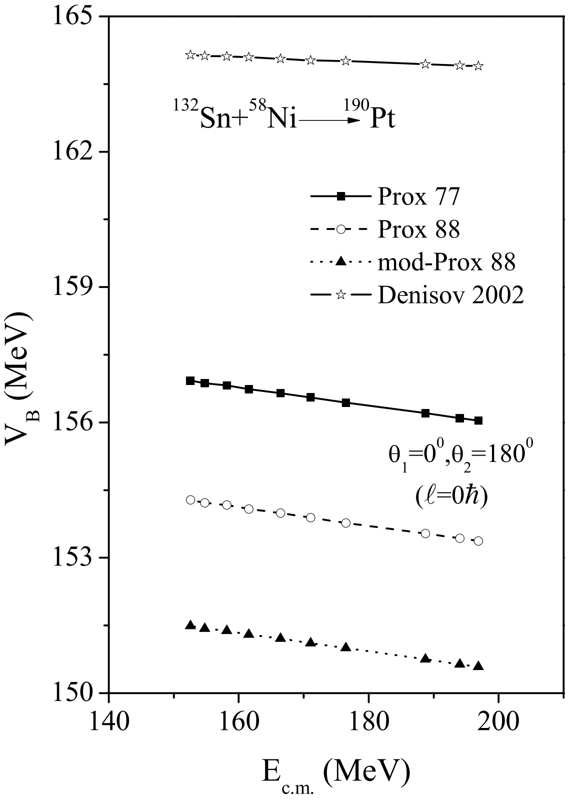

Figure 4.11: Barrier height V_B as a function of $E_{c.m.}$ for ^{132}Sn+^{58}Ni, using illustrated proximity potentials.

Figure 4.12(a) shows the fusion excitation function, i.e., the calculated fusion cross-section as a function of center-of-mass energy $E_{c.m.}$ for the ^{132}Sn+^{58}Ni reaction using the four illustrated proximity potentials in the extended Wong model, and are compared with the experimental data of [22]. The Wong model calculations for mod-Prox 1988 fit the data nicely at above as well as below the Coulomb barrier energies. The nuclear proximity potential Prox 1977 underestimates the data at lowest two values. The Prox 1988 potential, having comparatively stronger dependence on the isospin and asymmetry of the reacting nuclei as compare to Prox 1977 even then fail to fit the data at lowest point. The Denisov 2002 potential having, highest barrier, do underestimate the experimental data at all reported energies. Figure 4.12(b) shows the variation of deduced ℓ_{max} with $E_{c.m.}$. It is to be noted here that at above barrier energies the ℓ_{max} is almost same for all the proximity potential considered.

The variation of ℓ_{max} at lower energies is not smooth; rather, there is sudden

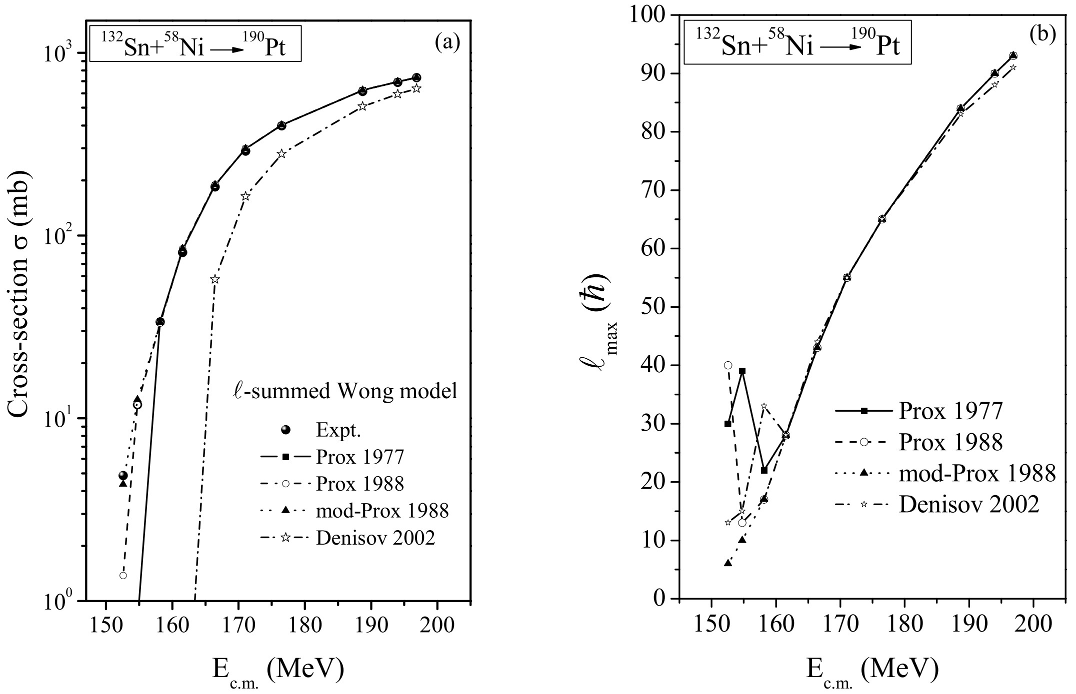

Figure 4.12: (a) Fusion excitation functions of ^{132}Sn+^{58}Ni→^{190}Pt* using the extended- Wong model, and (b) deduced ℓ_{max} values *vs.* $E_{c.m.}$, using four proximity potentials i.e. Prox 77, Prox 88, mod-Prox 88 and Denisov 2002.

increase in ℓ_{max} values at lower energies for Denisov 2002, Prox 77 and Prox 88. This behavior can be smoothed by introducing the appropriate empirical barrier modification in these potential, which is taken care in mod-Prox 1988 with the adequate isospin effect and asymmetry of colliding nuclei. It is relevant to mention here that experimental data was nicely expressed with in DCM for all proximity considered, as the barrier modification gets introduced in natural way due to use of neck length parameter ΔR. It is noted that the use of different proximity potentials in DCM, lead to change in magnitude of neck-length parameter and hence barrier modification, as consequence of this the fragmentation potential and preformation probability gets modified. However, the Wong model is very sensitive to barrier characteristics, since these interactions enter in the fusion cross-section formula directly, so the modification of fusion cross-section due to the change in the nuclear proximity potential is clearly visible with in the Wong model.

4.2.3 Fusion hindrance in Sn-induced reactions

Fusion hindrance is the unexpected behavior or steep fall of fusion cross-sections at deep sub-barrier energies. This phenomenon in heavy- ion reactions is extensively investigated on theoretical as well as experimental front. Recently, Misicu and Greiner [23] showed that M3Y potential, with an additional repulsive core, nicely describe the capture cross-sections of ^{48}Ca- induced reactions with in Coupled channel calculations and Wong formula. Later on, Misicu and Esbensen [24] used the same recipe of M3Y+repulsion for fusion- evaporation cross-section of Ni-induced symmetric (^{58}Ni+^{58}Ni, ^{64}Ni+^{64}Ni) and asymmetric (^{64}Ni+^{100}Mo) reactions. These Ni- induced reactions show clear signature of fusion hindrance phenomenon. The repulsive core is used to modify the shape of inner part of potential in terms of thicker barrier and shallower pocket. Thus the barrier characteristics were shown to influence the fusion hindrance process significantly. In the present work, we have addressed the fusion hindrance in Sn- induced reactions by (i) modifying the barrier characteristics using the neck-length parameter (ΔR) in the DCM in context of barrier lowering (ΔV_B), and (ii) using a variety of proximity interactions (having different characteristics) with in extended Wong model. This study is further important as the radioactive beams are involved which correspond to higher N/Z ratio. In the framework of DCM, it is observed that as the neutron numbers are increased either in radioactive projectile beam (Sn) or in target Ni, the barrier lowering parameter ΔV_B decreases i.e. become less negative (see Fig. 4.10). This suggests that the fusion probability increases with increase in neutrons in the compound nucleus. This observation is in agreement with the experimental result of Ref. [14], and could be useful for overall understanding of reaction dynamics involving stable and radioactive ion beams. Beside this, an application of different barrier characteristics corresponding to different nuclear proximity potentials is made with in the extended Wong model, to study the fusion hindrance in ^{132}Sn+^{58}Ni at sub-barrier energies. It is observed in Fig. 4.12 (a) that the mod-Prox 1988 potential, having strong isospin dependence, explains the fusion cross-sections better than other choices of nuclear proximity interactions. Fig. 4.12 (b) shows that at above barrier energies, all the chosen nuclear proximity potentials yield approximately same value of ℓ_{max}. As higher angular momentum states contribute above the Coulomb barrier, so the corresponding magnitude of centrifugal potential is comparable to that of nuclear proximity potential. On the contrary at deep sub-barrier energies, the variation of ℓ_{max} is not smooth and relatively lower ℓ-states contribute, so the magnitude of centrifugal potential is small as compare to the nuclear potential. Thus the nuclear proximity potentials, which depend on the isospin and asymmetry of colliding nuclei, play a significant role in explaining fusion hindrance at sub-barrier energies. The above results emphasize the fact that appropriate barrier characteristics are required in any model calculation for explaining the concept of fusion hindrance and related phenomena.

4.3 Conclusions

In this chapter, the decay of Pt^* isotopes formed using the neutron-rich radioactive beams of Sn is studied using the DCM. The effect of deformations and orientation are included and the entrance channel effects in the decay of $^{190}Pt^*$ are investigated using two different radioactive beams ^{126}Sn+^{64}Ni and ^{132}Sn+^{58}Ni. On comparing the results of calculations for the two reaction channels at approximately similar center-of-mass energy $E_{c.m.} \sim 190$ MeV, it is observed that CN formation is independent of the different entrance channel and it persists even with the use of different nuclear proximity potentials and level density parameter. The fission mass distribution of Pt isotopes formed in ^{124,126,127,128,132}Sn+^{64}Ni$\rightarrow^{188,190,191,192,196}$Pt* reactions is also studied. It is observed that the mass distribution becomes more asymmetric with increase in the N/Z ratio of the compound nucleus. With the neutron excess in the projectile/target, the barrier lowering (ΔV_B) decreases (less negative), hence fusion hindrance also decreases in agreement with experimental observation.

Alternatively the fusion hindrance phenomena is also dealt with in the framework of extended Wong model. The fusion excitation function have been studied for ^{132}Sn+^{58}Ni reaction at above and below the Coulomb barrier using different proximity potentials (Prox 1977, Prox 1988, mod-Prox1988 and Denisov 2002). It is found that mod-Prox 1988, having strong dependence of isospin and asymmetry of colliding nuclei, describes the experimental data very well at above, and especially at below the Coulomb barrier energies with smooth variation of $\ell_{max}(E_{c.m.})$. Since the potentials considered here differ mainly in the dependence of isospin and asymmetry of colliding nuclei, so it is concluded that this dependence play significant role in explaining the fusion hindrance phenomena. After detailed description of dynamics of Pt nuclei using stable and radioactive Sn beams in Chapter 3 and 4, a large number of heavy ion reactions were investigated to explore the effect of deformations and orientations on interaction barrier and fusion cross-sections by employing a variety of proximity interactions. The results are discussed in Chapter 5.

Bibliography

[1] B. B. Singh, M. K. Sharma, and R. K. Gupta, Phys. Rev. C. **77**, 054613 (2008).

[2] R. Kumar, and R. K. Gupta, Phys. Rev. C. **79**, 034602 (2010).

[3] R. K. Gupta, in *Cluster in Nuclei*, Lecture Notes in Physics 818, Vol. I, edited by C. Beck (Springer-Verlag, Berlin, 2010), p. 223.

[4] R. K. Gupta, S. K. Arun, R. Kumar, and M. Bansal, Nucl. Phys. A **834**, 176c (2010).

[5] D. Jain, R. Kumar, M. K. Sharma and R. K. Gupta, Phys. Rev. C. **85**, 2155 (2012).

[6] M. Kaur, R. Kumar, and M. K. Sharma, Phys. Rev. C. **85**, 014609 (2012).

[7] M. Kaur, and M. K. Sharma, Phys. Rev. C. **85**, 054605 (2012).

[8] K. Sandhu, M. K. Sharma and R. K. Gupta, Phys. Rev. C. **85**, 024604 (2012).

[9] R. Kumar, M. Bansal, S. K. Arun, and R. K. Gupta, Phys. Rev. C **80**, 034618 (2009).

[10] E. F. Aguilera and J. J. Kolata, Phys. Rev. C **85**, 014603 (2012).

[11] R. Kumar, M. K. Sharma, and R. K. Gupta, Nucl. Phys. A **870-871**, 42-57 (2011).

[12] W. S. Freeman *et al.*, Phys. Rev. Lett. **50**, 1563 (1983).

[13] K. T. Lesko *et al.*, Phys. Rev. C. **34**, 2155 (1986), J. F. Liang *et al.*, *ibid.* **75**, 054607 (2007) *ibid.* **78**, 047601 (2008).

[14] J. F. Liang *et al.*, Phys. Rev. C. **85**, 031601(R) (2012).

[15] J. Blocki, J. Randrup, W. J. Swiatecki, and C. F. Tsang, Ann. Phys. (N.Y.) **105**, 427 (1977).

[16] P. Möller and J. R. Nix, Nucl. Phys. A **361**, 117 (1981).

[17] R. Kumar, Phys. Rev. C. **84**, 044613 (2011).

[18] W. D. Myers and W. J. Światecki, Phys. Rev. C **62**, 044610 (2000).

[19] V. Y. Denisov, Phys. Lett. B **526**, 315 (2002).

[20] C. Y. Wong, Phys. Rev. Lett. **31**, 766 (1973).

[21] M. K. Sharma, S. Kanwar, G. Sawhney, R. K. Gupta and W. Greiner, J. Phys. G: Nucl. Part. Phys. **38**, 055104 (2011).

[22] Z. Kohley *et al.*, Phys. Rev. Lett. **107**, 202701 (2011).

[23] S. Misicu and W. Greiner, Phys. Rev. C **69**, 054601 (2004).

[24] S. Misicu and H. Esbensen, Phys. Rev. Lett. **96**, 112701 (2006); Phys. Rev. C **75**, 034606 (2007).

Chapter 5

Comparative analysis of proximity potentials with deformation effects included

5.1 Introduction

In the low energy heavy-ion collisions, fusion of colliding nuclei and related phenomena has always been of central interest. The collision of two massive nuclei holds a special place in nuclear reaction studies as a large number of nucleons are involved in the interaction process. In this type of reactions the nuclear potential holds key factor in deciding the fate of a colliding pair of any size. It is relevant to mention here that the most of the colliding nuclei are deformed in nature. Hence, deformations and orientation degree of freedom play an important role in explaining the features of fusion dynamics. In previous chapters, role of deformations were investigated in the decay of Pt^* isotopes using DCM and here, the same effect is analyzed for a variety of colliding nuclei on the fusion barrier characteristics which consequently effect the fusion cross-sections with in the framework of Wong formula. In this chapter, the nuclear part is calculated by taking different proximity potentials, based on the proximity force theorem. These proximity potentials are the benchmark and backbone for majority of microscopic/macroscopic fusion models.

Recently a comparative study of fusion barriers was carried out for a number of reactions considering asymmetric colliding nuclei to be spherical and concluded that the potentials Prox 88, Bass 80, AW 95 and Denisov DP can reproduce the empirical barrier heights within $\sim \pm 5\%$ whereas others need $\pm 10\%$ to produce the same result [1]. The comparison of different proximity potentials was carried out by considering colliding nuclei to be spherical and the fusion cross-sections of selected reactions were explained by Bass 80, AW 95 and Denisov DP potentials at above barrier energies. It is relevant to mention here that the deformation effects were not included in Ref. [1], although many of chosen reactions involve deformed target/projectile combinations.

In the work reported in this chapter, the effect of deformation and orientations are included for all deformed systems and have seen its influence on barrier characteristics which in turn modify the fusion cross-sections. Here, 52 heavy ion reactions are considered with asymmetry ($A_S = \frac{N-Z}{N+Z}$) lying in the range 0.02 and 0.23 and mass asymmetry η_A between 0.0 and 0.96. The effect of deformations and "optimum" orientation is studied on the barrier characteristics and it is observed that the fusion barrier heights get improved and compare nicely with the empirical barriers (with in $\sim \pm 5\%$ except for Prox 00). The static deformations are taken from [2] along with optimum orientations from Ref. [3]. For coplanar nuclei, the orientations are optimized (uniquely fixed) for each pair of quadrupole deformed (prolate or oblate) or quadrupole deformed + spherical colliding nuclei leading to cold or hot fusion configurations. Here, the barrier characteristics are obtained for hot configuration at optamized angles taken from Ref. [3] as the same can not be calculated for arbitrary choice of orientations. There are various methods for introducing barrier modification effect i.e. changing barrier characteristics (barrier height, barrier position and curvature) which in turn modify fusion cross-sections: (i) with the use different Skyrme forces, since a different Skyrme forces, give different barrier characteristics in Semiclassical extended Thomas-Fermi (SETF) approach [4, 5], (ii) with incorporation of ℓ dependent barriers [6], (iii) with the inclusion of deformation and orientation [6, 7]. It is worth noting here that the Prox 77 potential was extensively used to address the above mentioned methods. Therefore the aim of present study is to investigate the effect of deformations up to β_2 and "optimum" orientation [3] on the barrier characteristics of a variety of heavy ion reactions using various nuclear proximity potentials i.e. Prox 77, Prox 88, Prox 00, Bass 80 and Denisov DP [1]. Further the application of these deformed potentials is exercised in context of fusion excitation functions. In order to understand the systematic behavior of proximity potentials we consider some illustrative ^{16}O, ^{48}Ca and ^{64}Ni-based reactions (known for fusion hindrance phenomena in coupled-channel calculations [8]), i.e. ^{16}O+^{92}Zr, ^{16}O+^{112}Sn, ^{16}O+^{186}W, ^{48}Ca+^{154}Cm, ^{48}Ca+ ^{96}Zr, ^{46}Ti+^{64}Ni, ^{64}Ni+^{64}Ni, ^{64}Ni+^{74}Ge, ^{64}Ni+^{100}Mo, and ^{132}Sn+^{64}Ni in medium mass region where the experimental data are available on both side of Coulomb barrier. The main interest was to see, how the different proximity potentials behave for different reactions.

It is to be noted here that out of eight reactions investigated for fusion cross-section in Ref. [1], only two reactions i.e. ^{16}O+^{112}Sn and ^{48}Ca+ ^{96}Zr are considered here, as in other reactions the target and projectile are spherical. From calculations it is clear that with inclusion of deformations the barrier characteristics get modified and consequently the fusion cross-sections are improved for majority of nuclear interaction potentials particularly at below barrier energies. It is observe that for O- and Ca- based reactions, Prox 77 fits the experimental data nicely at sub-barrier energies. For Ni-based reactions Prox 88 seems better at below the Coulomb barrier as it includes strong isospin effects. In every case Prox 88 overestimates the experimental data at above barrier energies as its barrier height is lowest among the all interaction potentials. In general Bass 80 and Denisov DP compete each other to give better comparison with the experimental data for above barrier energies. It means at above barrier energies one may choose Bass 80 or Denisov DP whereas at sub-barrier energies Prox 88 in case of Ni-based reactions and Prox 77 in case of O and Ca-based reactions. It is relevant to mention here that Wong made few approximations in order to derive the formula for cross-section. In 2009, Gupta and collaborators removed these approximations and carried out the actual summation over ℓ-values and denoted it as extended-Wong model [6]. It was observed that the cross-section calculated using extended-Wong model approaches the Wong formula as the maximum value of ℓ in former approaches infinity i.e.

$$\sigma_{fus}(extended - Wongmodel) \rightarrow \sigma_{fus}(Wongformula),$$

as $\ell_{max} \rightarrow \infty$. Recently, Aguilera and Kolata [9] also used the extended Wong model for fusion of halo and weakly bound systems. Now in context to the present calculations if one uses the extended-Wong model, then Prox 88 and other interactions can provide better fit to the data at all energies with smooth variation of maximum value of angular momentum ℓ_{max} (for more details see Ref. [6]). But for the sake of comparison of cross section calculated using various proximity potentials, we restrict ourself to Wong formula only.

The chapter is organized as follows. The calculations are presented in Sec. 5.2. The calculations are done by considering various versions of proximity potentials using Wong formula [10], with effects of deformations included and orientation degrees of freedom integrated for the co-planer [11] configuration of nuclei. The discussion of results and conclusions are described in Sec. 5.3.

5.2 Calculations and Results

In this section, firstly the effect of deformation and orientations on fusion barrier characteristics are studied using various nuclear proximity potentials and then an application of these deformation dependent barriers calculated using deformed proximity potentials is made in calculation of fusion cross-sections using Wong formula

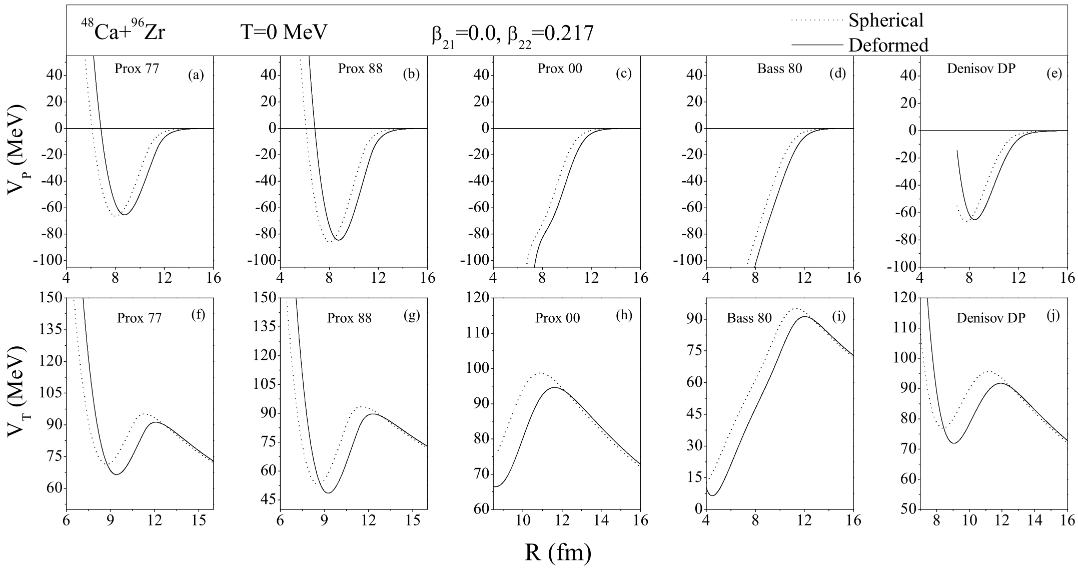

Figure 5.1: The nuclear interaction potential is shown in (a) to (e) and corresponding total interaction potential in (f) to (j) using Prox 77, Prox 88, Prox 00, Bass 80 and Denisov DP, for ^{48}Ca+^{96}Zr reaction as a function of internuclear distance R (fm) at T=0 MeV for both deformed and spherical choice of nuclei.

for illustrative O-, Ca- and Ni-induced reactions in order to see the possible effect of the deformation and orientation of the nuclei.

5.2.1 Effect of deformation and orientations on barrier characteristics

Fig. 5.1 (a)-(e) show the nuclear proximity potential (V_P) for ^{48}Ca+^{96}Zr reaction at T=0 MeV for both spherical and deformed choice of nuclei using illustrated nuclear potentials Prox 77, Prox 88, Prox 00, Bass 80 and Denisov DP. All these considered nuclear potentials have different isospin and asymmetry dependence. It is clear from upper panel of Fig. 5.1 that the nuclear proximity potential is attractive for all the proximity potentials used and gets considerably modified with the inclusion of deformations of nuclei. One may see from Fig. 5.1 (c) and (d) that Prox 00 and Bass 80 do not have a repulsive core at a shorter distance whereas all other proximity potentials are attractive at long distances followed by repulsive core at shorter internuclear distances. For the proximity with repulsive core, Prox 88 gives

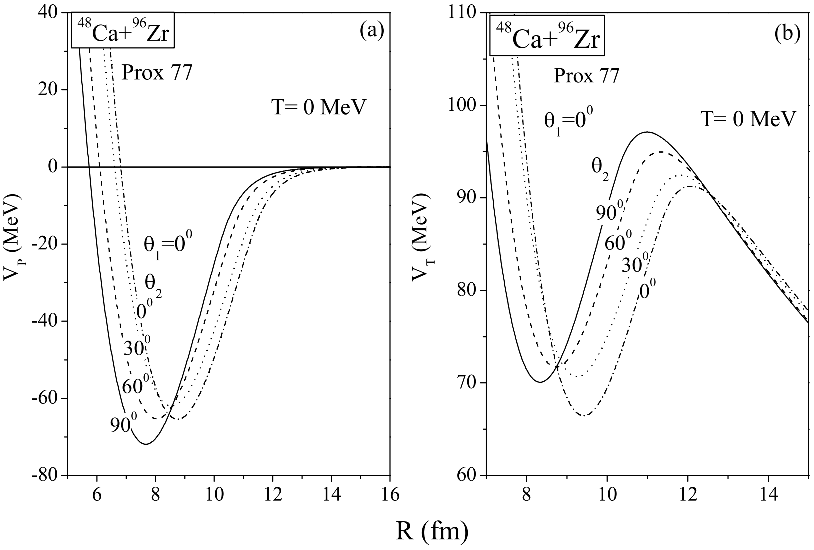

Figure 5.2: (a) Nuclear interaction potential and (b) total interaction potential for ^{48}Ca+^{96}Zr system at different θ_2 values keeping $\theta_1 = 0^0$ fixed at T=0 MeV.

stronger and deeper pocket followed by Prox 77 and Denisov DP.

Now in order to obtain the fusion barrier height (V_B), barrier position (R_B) and oscillator frequency ($\hbar\omega$), the Coulomb potential is added to the nuclear potential that gives the total interaction potential. Fig. 5.1 (f)-(j) show the total interaction potentials (V_T) which is calculated by adding Coulomb interaction to respective proximity interactions represented in Fig. 5.1 (a)-(e). It is clear from the lower panel of Fig. 5.1 that the barrier characteristics change significantly when the effect of deformation is taken into account for all the proximity potentials considered in present study. An application of these modified barrier characteristics is worked out using Wong formula [10] in reference to available experimental data on fusion cross-sections. Note that the pocket does not play much role and only the barrier characteristics are important in context of Wong model calculations of fusion cross-section. Detailed description of those results is given in Sec. 5.2.2.

The orientation θ degree of freedom also modifies the barrier parameters strongly, as is illustrated in Fig. 5.2. It shows the variation of nuclear proximity potential (Fig. 5.2 (a)) and corresponding total interaction potential (Fig. 5.2 (b)) for ^{48}Ca+^{96}Zr

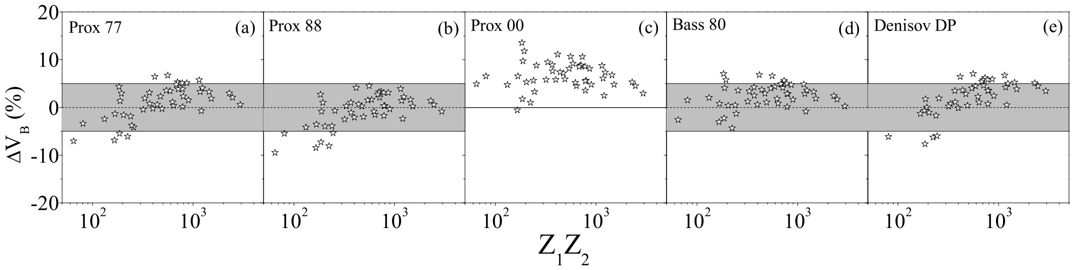

Figure 5.3: The percentage deviation of barrier height as a function of the product of charges Z_1Z_2 using different versions of the proximity potential, taking deformations up to β_2 at "optimum" orientations [3].

reaction at different values of θ_2 while keeping θ_1 fixed at 0^0 at T=0 MeV for the case of Prox 77 only. It is clear from this figure that with the change of orientation the depth of nuclear proximity potential as well as barrier characteristics change significantly. Thus deformation and orientation degree of freedom automatically takes care of barrier modification effect [4–6], which can play significant role at near- and sub-barrier energies.

After that the extensive comparative study of fusion barrier characteristics for 52 colliding nuclei with mass asymmetry in range of 0-0.96 is carried out. The reactions are arranged in ascending order of Z_1Z_2 in the Table 5.1 and Table 5.2 for different proximity potentials. Except few cases, we have mainly confined to those reactions which involves either target or projectile or both as deformed nuclei reported in Ref. [1]. Fig. 5.3 display the percentage difference of the fusion barrier heights $\Delta V_B(\%)$ as a function of the product of charges Z_1Z_2. The percentage difference of the fusion barrier heights $\Delta V_B(\%)$ defined as

$$\Delta V_B(\%) = \frac{{V_B}^{theor} - {V_B}^{expt}}{V_B^{expt}} \times 100. \tag{5.1}$$

These barrier heights are calculated by taking deformations up to β_2, with "optimum" orientation degree of freedom. It may be noted that the position and height of the Coulomb barrier could not be measured directly in an experiment. Therefore the average fusion excitation functions are obtained by fitting the experimental data

Table 5.1: Fusion barrier heights V_B and positions R_B with inclusion of deformation up to β_2 and “optimum” orientations [3] for the use of different proximity potentials for 52 asymmetric systems in increasing order of $Z_P Z_T$.

Reaction	β_{21}	β_{22}	$\theta^{opt.}_{1,2}$	Prox 77		Prox 88		Prox 00	
				V_B	R_B	V_B	R_B	V_B	R_B
^{11}B+^{27}Al	-0.086	-0.448	0,180	10.4	8.25	10.13	8.5	11.75	7.22
^{6}Li+^{59}Co	-0.099	0.143	0,90	11.59	9.38	11.33	9.62	12.79	8.43
^{4}He+^{164}Dy	0.125	0.292	90,90	16.72	10.54	16.41	10.76	17.95	9.77
^{4}He+^{209}Bi	0.125	-0.008	90,180	19.52	11.13	19.19	11.62	20.85	10.79
^{26}Mg+^{30}Si	-0.310	0	0,180	24.46	9.96	23.89	9.32	26.42	8.38
^{6}He+^{238}U	-0.078	0.215	0,90	21.16	11.68	20.82	11.89	23.03	10.68
^{6}Li+^{144}Sm	-0.099	0	0,180	23.28	10.79	22.84	11.02	25.08	9.98
^{14}N+^{59}Co	-0.019	0.143	0,90	26.48	9.49	25.89	9.73	28.66	9.25
^{7}Li+^{159}Tb	-0.086	0.271	0,90	24.5	10.59	24.05	10.82	26.6	9.71
^{24}Mg+^{35}Cl	0.374	-0.252	90,180	30.19	8.84	29.47	9.08	32.33	8.24
^{18}O+^{64}Ni	0.021	-0.087	90,180	30.49	9.78	29.85	10.01	32.83	9.05
^{12}C+^{92}Zr	0.01	0.053	90,90	31.69	10.14	31.04	10.37	34.12	9.38
^{6}Li+^{208}Pb	-0.099	0	0,180	28.94	11.52	28.45	11.73	31.07	10.7
^{16}O+^{72}Ge	0	-0.224	0,180	35.9	9.38	35.12	9.62	38.53	8.71
^{16}O+^{92}Zr	0	0.053	0,90	41.8	10.23	40.95	10.48	44.45	9.62
^{10}Be+^{209}Bi	-0.1	-0.008	0,180	38.32	11.71	37.69	11.93	41.15	10.88
^{19}F+^{93}Nb	0.275	0.053	90,90	48.03	10.25	47.05	10.48	50.76	9.68
^{12}C+^{152}Sm	0.01	0.243	90,90	46.75	10.57	45.88	10.8	49.92	9.86
^{18}O+^{124}Sn	0.021	0	90,180	49.16	10.93	48.26	11.18	52.19	9.97
^{16}O+^{112}Sn	0	0.018	0,90	50.8	10.57	49.8	10.8	53.8	9.95
^{27}Al+^{70}Ge	-0.448	-0.241	0,180	58.65	9.23	57.37	9.46	61.22	8.85
^{35}Cl+^{54}Fe	-0.252	0	0,180	58.93	10.01	58.97	9.45	62.92	9.54
^{37}Cl+^{64}Ni	0	-0.087	0,180	61.98	10.24	60.73	10.47	64.93	9.76
^{12}C+^{204}Pb	0.01	-0.008	0,180	57.38	11.58	56.4	11.79	60.96	10.86
^{37}Cl+^{73}Ge	0	-0.224	0,180	71.67	10.04	70.22	10.27	74.82	9.6
^{28}Si+^{92}Zr	-0.478	0.053	0,90	75.71	9.77	74.13	10.00	78.48	9.43
^{16}O+^{186}W	0	0.23	0,90	71.22	11.07	69.98	11.28	75.17	10.45
^{46}Ti+^{64}Ni	0	-0.087	0,180	78.96	10.4	77.39	10.64	82.03	10.00
^{32}S+^{89}Y	0	0.035	0,90	78.63	10.64	77.08	10.87	81.79	10.2
^{36}S+^{90}Zr	0	0.035	0,90	79.29	10.84	77.77	11.07	82.55	10.39
^{35}Cl+^{92}Zr	-0.252	0.053	0,90	86.9	10.39	85.19	10.63	89.98	10.04
^{28}Si+^{120}Sn	-0.478	0	0,180	90.45	10.29	88.67	10.52	93.45	9.97
^{19}F+^{197}Au	0.275	-0.131	90,180	84.74	11.13	83.29	11.34	88.78	10.6
^{16}O+^{238}U	0	0.215	0,90	84.87	11.57	83.5	11.78	89.42	10.93
^{35}Cl+^{106}Pd	-0.252	0.171	0,90	99.13	10.43	97.21	10.66	102.37	10.11
^{64}Ni+^{64}Ni	-0.087	-0.087	0,180	98.21	10.6	96.34	10.84	101.54	10.26
^{58}Ni+^{60}Ni	0	0.027	0,90	99.65	10.49	96.3	10.94	101.27	10.36
^{48}Ca+^{96}Zr	0	0.217	0,90	97.1	11.01	95.36	11.23	100.7	10.59
^{40}Ca+^{90}Zr	0	0.035	0,90	99.1	10.84	97.18	11.07	102.33	10.37
^{28}Si+^{144}Sm	-0.478	0	0,180	109.23	10.59	107.12	10.82	112.33	10.31
^{64}Ni+^{74}Ge	-0.087	0.224	0,180	112.96	10.47	110.82	10.69	116.43	10.16
^{50}Ti+^{93}Nb	0	0.053	0,90	108.49	11.17	106.49	11.4	111.99	10.79
^{28}Si+^{208}Pb	-0.478	0	0,180	135.37	11.36	133.05	11.58	139.22	11.06
^{64}Ni+^{100}Mo	-0.087	0.244	0,90	140.93	11.09	138.42	11.32	144.76	10.78
^{40}Ar+^{165}Ho	0	0.293	0,90	140.34	11.45	137.96	11.67	144.89	11.05
^{48}Ca+^{154}Sm	0	0.27	0,90	142.5	11.63	140.15	11.84	147.07	11.22
^{132}Sn+^{64}Ni	0	-0.087	0,180	157.78	11.95	155.25	12.16	162.16	11.58
^{32}S+^{232}Th	0	0.207	0,90	160.82	11.98	158.26	12.19	166.21	11.51

Table 1 continued...

Reaction	β_{21}	β_{22}	$\theta_{1,2}^{opt.}$	Prox 77		Prox 88		Prox 00	
				V_B	R_B	V_B	R_B	V_B	R_B
^{40}Ca+^{192}Os	0	0.155	0,90	171.21	11.91	168.4	12.13	176.07	11.49
^{64}Ni+^{208}Pb	-0.087	0	0,180	242.94	12.78	239.25	12.99	248.74	12.37
^{70}Zn+^{208}Pb	0.045	0	90,180	255.71	13.06	251.91	13.27	261.92	12.6
^{86}Kr+^{208}Pb	0.053	0	90,180	300.88	13.33	296.52	13.54	307.86	12.83

with the single-barrier penetration model of Wong and the relevant parameters i.e. the barrier radius, curvature, and barrier height are extracted accordingly. There is an improvement in the fusion barrier heights as compared to the spherical choice of nuclei [1]. Prox 77, Prox 88, Bass 80 and Denisov DP reproduce the empirical barrier heights with in ±5% approximately whereas Prox 00 comes in the approximate range of ±10%. This shows that barriers calculated using Prox 77, Prox 88, Bass 80 and Denisov DP has accuracy up to ~95%. More precise values of fusion barrier heights V_B (in MeV) and its position R_B (in fm) and corresponding "optimum" orientations are shown in Table 5.1 and Table 5.2.

The effect of deformation on barrier characteristics incorporated through the use of different proximity potentials provide an interesting input to understand the formation process in a variety of nuclear reactions and this information regarding modification of barrier characteristics could be of extreme importance for overall understanding of heavy ion reaction mechanism.

5.2.2 Application of various deformed proximity interactions in the calculations of fusion cross-sections

It is observed in Section 5.2.1 that with the inclusion of deformation and orientations, the barrier characteristics get modified which consequently effect the fusion cross-sections. It is relevant to mention here that the barrier characteristics in Section 5.2.1 are shown only up to β_2-deformations with in optimum orientation approach, as one needs to keep the orientation angles same to draw comparison of different

Table 5.2: Same as Table 5.1 but for Bass 80 and Denisov DP along with empirical values.

Reaction	Bass 80		Denisov DP		Empirical		
	V_B	R_B	V_B	R_B	V_B	R_B	Ref.
^{11}B+^{27}Al	10.9	7.9	10.23	7.75	11.27	7.69	[12]
^{6}Li+^{59}Co	12.19	8.92	11.25	9.65	12	7.6	[13]
^{4}He+^{164}Dy	17.49	10.06	15.75	11.21	17.14	10.32	[14]
^{4}He+^{209}Bi	20.32	11.09	18.49	12.17	20.98	10.04	[15]
^{26}Mg+^{30}Si	24.99	8.93	24.46	9.05	24.8	9.05	[16]
^{6}He+^{238}U	21.7	11.42	20.13	12.19	20.28	12.5	[17]
^{6}Li+^{144}Sm	24.08	10.43	22.73	11.02	24.65	10.2	[18]
^{14}N+^{59}Co	27.19	9.25	26.58	9.42	26.13	9.6	[19]
^{7}Li+^{159}Tb	25.18	10.32	23.81	10.86	23.81	11.03	[14]
^{24}Mg+^{35}Cl	30.81	8.72	30.36	8.8	30.7	8.84	[20]
^{18}O+^{64}Ni	31.05	9.61	30.45	9.74	32.5	9.04	[21]
^{12}C+^{92}Zr	32.45	9.9	31.75	10.08	32.31	9.68	[22]
^{6}Li+^{208}Pb	29.7	11.22	28.29	11.74	30.1	11.00	[23]
^{16}O+^{72}Ge	36.64	9.2	36.07	9.3	35.4	9.7	[24]
^{16}O+^{92}Zr	42.52	10.06	42.08	10.13	42.00		[25]
^{10}Be+^{209}Bi	38.86	11.29	37.89	11.78	37.6	13.5	[26]
^{19}F+^{93}Nb	48.57	10.14	48.21	10.16	46.6	9.2	[27]
^{12}C+^{152}Sm	47.52	10.38	46.91	10.5	46.39	10.77	[14]
^{18}O+^{124}Sn	49.6	10.85	49.24	10.89	49.3	10.98	[28]
^{16}O+^{112}Sn	51.61	10.37	49.8	10.8	51.35	10.27	[29]
^{27}Al+^{70}Ge	58.9	9.26	58.67	9.27	55.1	10.2	[30]
^{35}Cl+^{54}Fe	60.76	9.64	60.7	9.59	58.59	10.14	[31]
^{37}Cl+^{64}Ni	62.38	10.15	62.32	10.12	60.6	10.59	[32]
^{12}C+^{204}Pb	58.15	11.39	57.76	11.45	57.55	11.34	[22]
^{37}Cl+^{73}Ge	71.98	9.98	72.03	9.92	69.2	10.6	[33]
^{28}Si+^{92}Zr	75.68	9.79	75.95	9.68	70.93	10.19	[22]
^{16}O+^{186}W	71.84	70.93	71.93	10.9	68.87	11.12	[22]
^{46}Ti+^{64}Ni	79.33	10.318	79.59	10.25	76.9	9.7	[27]
^{32}S+^{89}Y	79.17	10.51	79.5	10.45	77.77	10.3	[22]
^{36}S+^{90}Zr	79.65	10.74	79.85	10.68	79.00	10.64	[34]
^{35}Cl+^{92}Zr	87.01	10.38	87.46	10.25	82.94	10.20	[22]
^{28}Si+^{120}Sn	90.13	10.34	90.87	10.17	85.89	11.04	[35]
^{19}F+^{197}Au	84.96	11.09	85.41	10.97	81.61	11.32	[22]
^{16}O+^{238}U	85.4	11.45	85.88	11.37	80.81	11.45	[22]
^{35}Cl+^{106}Pd	99.12	10.44	99.85	10.27	94.3	11.27	[36]
^{64}Ni+^{64}Ni	98.18	10.58	98.8	10.46	98.1		[37]
^{58}Ni+^{60}Ni	98.74	10.56	99.32	10.48	96	10.26	[22]
^{48}Ca+^{96}Zr	96.94	10.99	95.36	11.23	95.9	11.21	[38]
^{40}Ca+^{90}Zr	99.59	10.69	100.32	10.59	96.88	10.53	[22]
^{28}Si+^{144}Sm	108.79	10.63	110.06	10.42	103.89	10.93	[22]
^{64}Ni+^{74}Ge	112.64	10.55	113.6	10.31	105.1	8.2	[39]
^{50}Ti+^{93}Nb	108.61	11.08	109.44	11.02	106.9		[40]
^{28}Si+^{208}Pb	134.24	11.45	136.76	11.13	128.07	11.45	[22]
^{64}Ni+^{100}Mo	140.4	11.07	142.23	10.85	136.5		[41]
^{40}Ar+^{165}Ho	140.07	11.38	142.05	11.16	141.38	11.48	[14]
^{48}Ca+^{154}Sm	141.89	11.6	143.94	11.35	137		[42]
^{132}Sn+^{64}Ni	156.74	11.94	159.51	11.63	156.0		[43]

Table 2 continued...

Reaction	Bass 80		Denisov DP		Empirical		
	V_B	R_B	V_B	R_B	V_B	R_B	Ref.
^{32}S+^{232}Th	160.76	11.85	163.93	11.55	155.73	11.18	[22]
^{40}Ca+^{192}Os	171.12	11.76	174.48	11.45	168.07	11.05	[22]
^{64}Ni+^{208}Pb	241.74	12.65	248.14	12.15	236.0		[44]
^{70}Zn+^{208}Pb	254.71	12.87	261.77	12.27	250.6		[44]
^{86}Kr+^{208}Pb	299.72	13.08	309.46	12.16	299.2		[44]

proximity interactions. However in this section to explore the effect of deformations in reference to available experimental data on fusion cross-sections, the deformation effects up to β_4 (hexadecapole) have been incorporated, subsequently integrated over all orientations for calculating fusion cross-sections. It is to be noted that the β_4 values for majority of chosen reactions are quite small, so this analysis should not differ much from that of β_2- considerations discussed in section 5.2.1. In this section the sub- barrier data (or equivalently the role of coupling) is addressed by employing a variety of nuclear interaction potentials in one dimensional barrier penetration model (Wong formula). In Wong's work [10], the coupling effects are included to some extent by taking the barrier parameters from Ref. [45] which are associated with relevant effective potential.

The scattering potential calculated for ^{48}Ca+^{96}Zr reaction at T=0 MeV and optimum orientations $\theta_1^{opt.}$=0^0 and $\theta_2^{opt.}$=90^0 is shown in Fig. 2.4, using various version of nuclear proximity potentials i.e. Prox 77, Prox 88, Prox 00, Bass 80, Denisov DP, CW 76 and BW 91. Here, only Prox 77, Prox 88, Denisov DP and Bass 80 are chosen for the calculations of fusion cross-section as these nuclear proximity potentials cover a wide range of barrier characteristics. The barrier characteristics of Prox 77 and BW 91 are approximately similar so the results are shown only for Prox 77. In other words it is expected that the cross-sections calculated using BW 91 should not differ much from the one for Prox 77. The barrier characteristics, and hence the corresponding fusion cross-section, of CW 76 lies in between to those of Prox 77 and Prox 88. Since Prox 00 is giving the maximum barrier height and

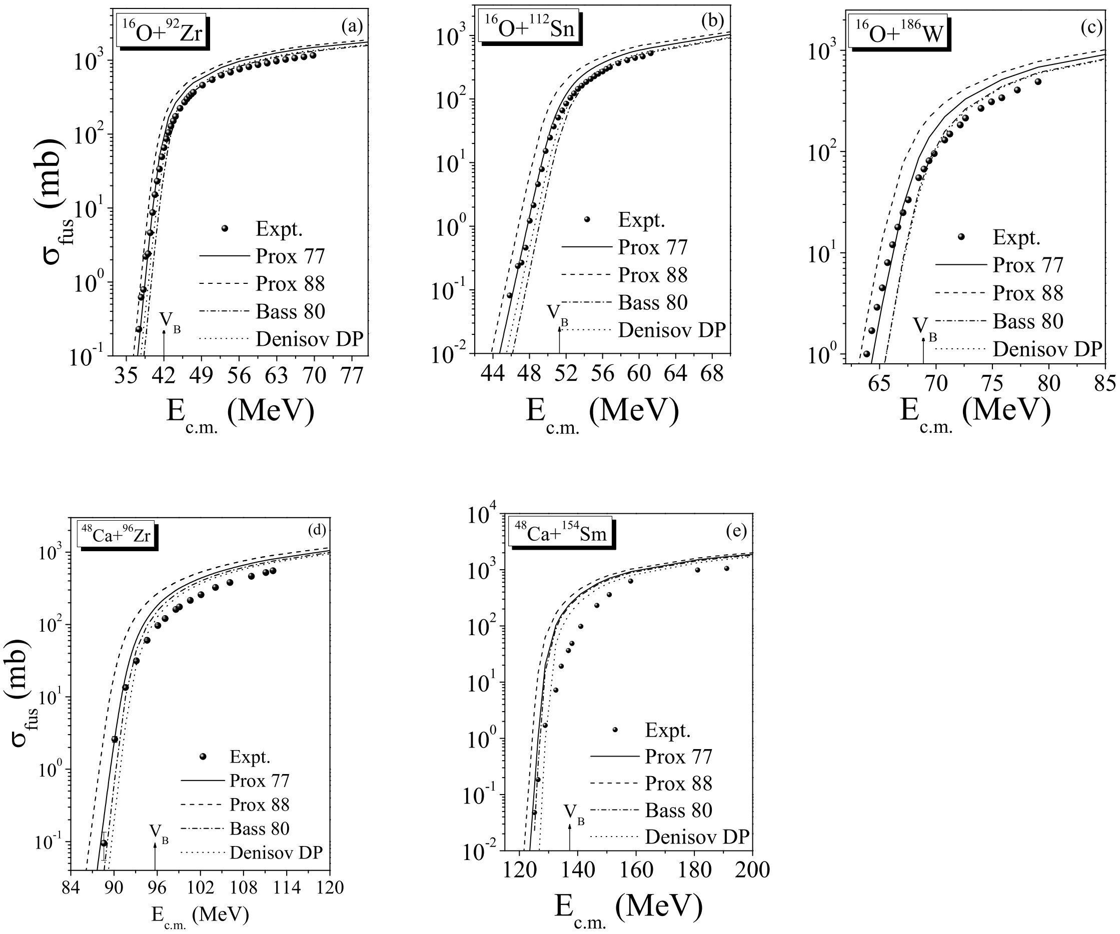

Figure 5.4: Comparison of fusion cross-sections calculated using various nuclear proximity potentials with in the Wong formula, integrated over θ_i, and the experimental data for (a) ^{16}O+^{92}Zr [25] (b) ^{16}O+^{112}Sn [29] (c) ^{16}O+^{186}W [22] (d) ^{48}Ca+^{96}Zr [38] (e) ^{48}Ca+^{154}Sm [42] reactions, as a function of $E_{c.m.}$. The upward arrow point out the Coulomb barrier of the reaction.

fusion cross-section is inversely proportional to barrier height, henceforth the Prox 00 underestimates the experimental data to a large extent. Therefore, cross-sections calculations for Prox 00 are not included in the discussion. It is also clear from Fig. 5.3 that $\Delta V_B\%$ is bad for Prox 00 when compared with other chosen proximity interactions. A large amount of experimental data are available for different reactions however we consider illustrative ^{16}O, ^{48}Ca and ^{64}Ni-based reactions from intermediate mass region to work out the comparison of different proximity interactions. The ^{64}Ni-based reactions are taken into considerations here as they are well known for fusion hindrance phenomena in coupled-channel calculations.

Fig. 5.4 (a), Fig. 5.4(b) and Fig. 5.4(c) show the fusion cross-section of the ^{16}O-based reactions i.e. ^{16}O+^{92}Zr, ^{16}O+^{112}Sn and ^{16}O+^{186}W, using nuclear interaction potentials Prox 77, Prox 88, Bass 80 and Denisov DP, with in the Wong formula. The Coulomb barrier energies for above reactions are indicated by the upward arrows in Fig. 5.4. With the inclusion of deformation and orientations effects the comparison of experimental data of fusion cross-sections and calculated one improves for majority of proximity potentials used, specially at below Coulomb barrier energies.

It is to be noted here that ^{16}O+^{112}Sn reaction was also considered in Fig. 8 of Ref. [1], and its comparison with Fig. 5.4 (b) improves significantly for all the considered proximity potentials. In general the fusion cross-section increases with inclusion of deformations and hence the comparison with experimental data improves particularly at below barrier region. More specifically, Prox 77 seems to give better results at below barrier energies and Denisov DP and Bass 80 compete with each other at above barrier energies giving better comparison with available data and Prox 88 having lowest barrier height, overestimates the data at all energies. The BW 91 (not shown here) is expected to behave similar to Prox 77 and Prox 00 is not included in this comparative analysis in view of very large barrier height observed for this case.

Fig. 5.4 (d) and Fig. 5.4 (e) show the comparison of calculated fusion cross-sections for Ca-based reactions with experimental data for all the proximity potentials considered. For these reactions experimental data is available for above as well as below the Coulomb barrier. Prox 77, Bass 80 and Denisov DP explain the experimental data nicely at below barrier energies. It is clear from the comparison of Fig. 5.4(d) for ^{48}Ca+^{96}Zr reaction with the one shown in Fig. 7 of Ref. [1], that the comparison with available data improves at below barrier energies with the inclusion of deformation and orientation effects. Thus from the above cases of O- and Ca-based reaction, the fusion cross-sections are largely affected with the deformations and orientations at below barrier energies. So these deformed proximities

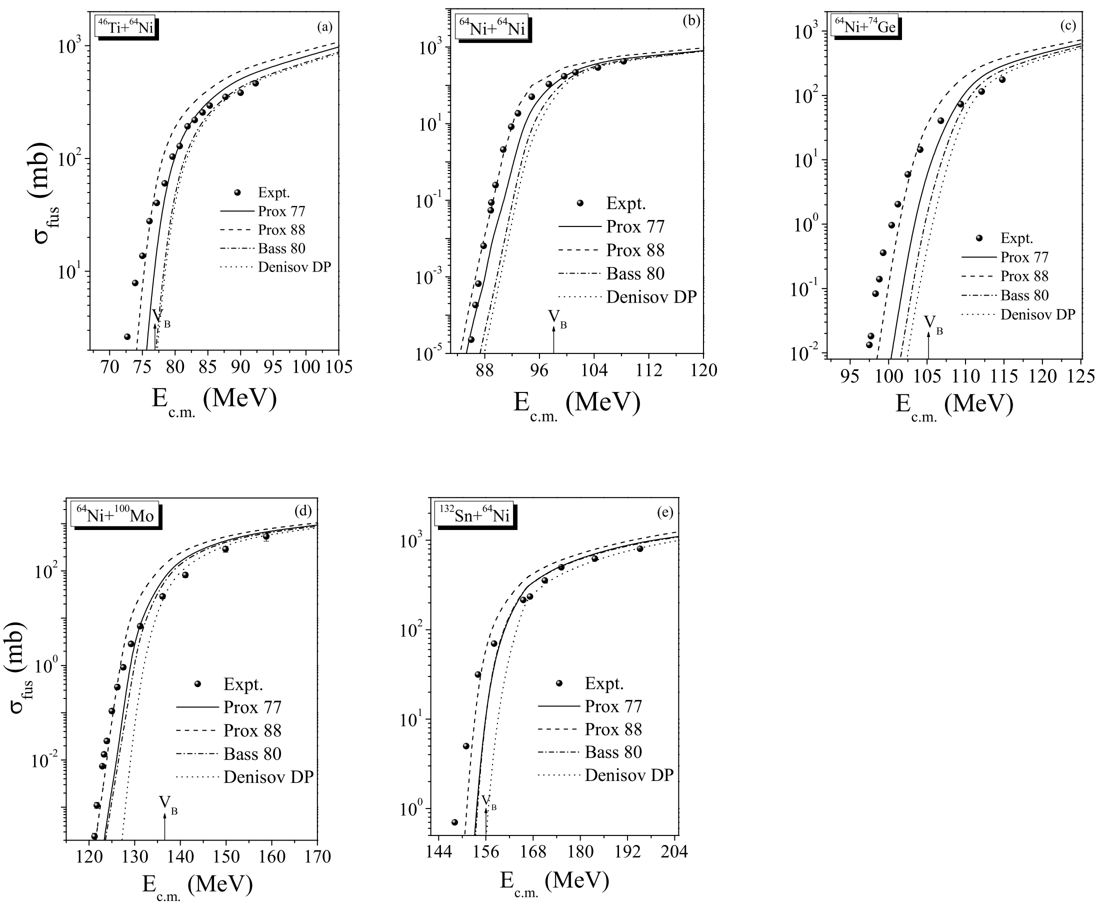

Figure 5.5: Same as Fig. 5.4 except that this shows comparison for (a) ^{46}Ti+^{64}Ni [27] (b) ^{64}Ni+^{64}Ni [37] (c) ^{64}Ni+^{74}Ge [39] (d) ^{64}Ni+^{100}Mo [41] and (e) ^{132}Sn+^{64}Ni [43] reactions.

are further tested for Ni-based reactions.

Fig. 5.5 shows the comparison of calculated fusion cross-section with experimental data for Ni-based reactions. Fusion cross-section is calculated at above and below the Coulomb barrier for ^{46}Ti+^{64}Ni (Fig. 5.5 (a)), ^{64}Ni+^{64}Ni (Fig. 5.5 (b)), ^{64}Ni+^{74}Ge (Fig. 5.5 (c)), ^{64}Ni+^{100}Mo (Fig. 5.5 (d)), and ^{132}Sn+^{64}Ni (Fig. 5.5 (d)) reactions. It is clear from this figure that at below barrier energies, fusion cross-section calculated using Prox 88 is close to the experimental data with effect of deformation included, whereas at above barrier energies, the chosen proximity interactions explain the data reasonably well. It is important to note here that the Ni-based reactions behave differently from O- and Ca-based reactions at below Coulomb barrier region. For Ni-based reactions Prox 88 seems to perform better as compared to Prox 77 or Denisov DP, which are good for the cases of O- or Ca- based

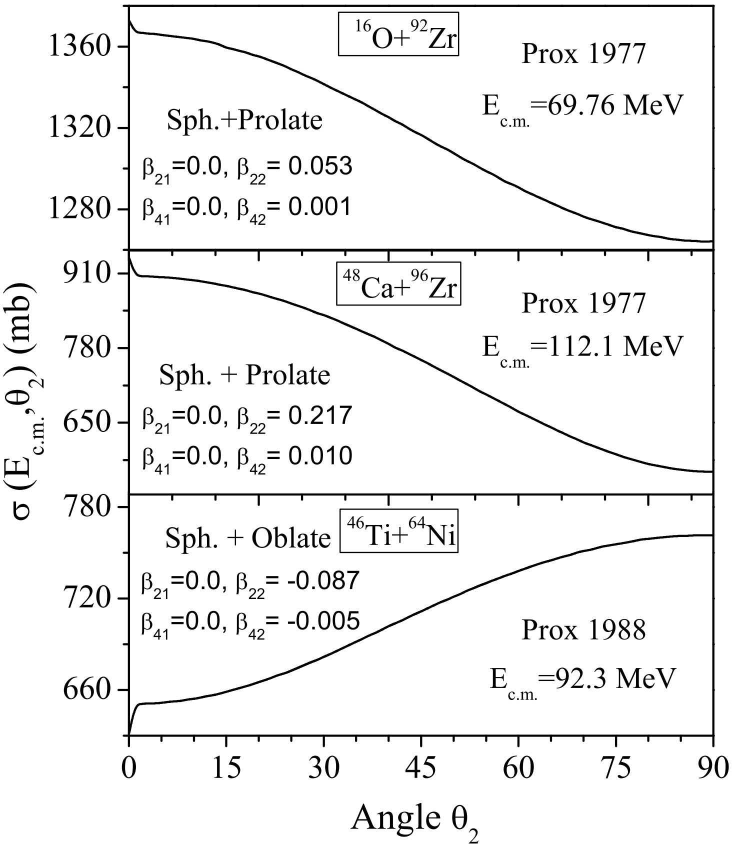

Figure 5.6: Cross section at each angle for ^{16}O+^{92}Zr, ^{48}Ca+^{96}Zr reaction using Prox 1977 and ^{46}Ti+^{64}Ni reaction using Prox 1988 at respective highest experimental $E_{c.m.}$ values.

reactions at below barrier energies. Thus, below the Coulomb barrier a stronger nuclear interaction like Prox 88 is preferred. It is so because the stronger isospin effects are included in this proximity potential, which along with deformation and orientation effect, lead to the required barrier characteristics. Another point of interest here is that for almost all the reactions considered for the study of fusion cross-section, theoretical calculations slightly over estimate the data for above barrier energies independent of choice of proximity potential. The problem of over estimation at higher energies can be resolved with the use of extended-Wong model [6, 9].

It would be of further interest to study the angular dependence of fusion cross-section of spherical/deformed target-projectile combinations. For this purpose, one reaction each from ^{16}O, ^{48}Ca and ^{64}Ni- based projectiles is chosen. As Prox 77 performs better for ^{16}O and ^{48}Ca based reactions and Prox 88 responds well for ^{64}Ni induced reactions, so the calculations are performed using relevant proximity interactions. Fig. 5.6 shows the variation of cross-section at each angle for ^{16}O+^{92}Zr, ^{48}Ca+^{96}Zr reaction using Prox 1977 and ^{46}Ti+^{64}Ni reaction using Prox 1988 at their highest experimental center-of-mass energies. These reactions have spherical projectile and deformed target (prolate or oblate). It is worth noting that the cross-section is maximum at θ_2=0^0 for prolate (β_2 positive) and θ_2=90^0 for oblate nuclei (β_2 negative). For in between configurations the fusion cross-sections vary smoothly as a function of orientation angle. Therefore, one may conclude that orientation degree of freedom plays a significant role in the fusion-fission dynamics of heavy ion reactions.

5.3 Conclusions

Effects of deformations and "optimum" orientations are studied for 52 heavy ion reactions having mass asymmetry η between 0.0 to 0.96 using various nuclear proximity potentials. It is observed that barrier height and barrier position get modified considerably with the inclusion of deformations for all the nuclear proximity potential considered. The fusion barrier heights get improved (with in $\sim \pm 5\%$ except for Prox 00) and hence come closer to the empirical barriers. As an application, these deformation dependent nuclear potentials are used for calculating fusion cross-sections of O-, Ca- and Ni-based reactions in medium mass region. The deformations up to hexadecapole (β_4) are used and cross-sections are integrated over all orientations for the co-planer nuclei. The results reveal that the inclusion of deformations and orientation degree of freedom improves the comparison with experimental data at below barrier energies. For Ni- based reactions Prox 88 comes close to the experimental data at below barrier energies as it includes strong isospin effects whereas for O and Ca- based reactions, Prox 77 seems a better option. At above barrier energies Bass 80 and Denisov DP compete each other and are comparable with the experimental data. It will be of further interest to test extended-Wong model for such reactions using various nuclear proximity potentials. It is anticipated that the overestimation of experimental data can be resolved by using extended-Wong model. After a comprehensive analysis of nuclear deformations using EDF based and proximity based nuclear interactions discussed in Chapter 3, 4 and 5. It will be of further interest to explore the exclusive effect of deformations and excitation energies, particularly on spin saturated and spin unsaturated nuclear interaction potential. The corresponding work is carried out by analysing the dynamics of $^{156-172}$Yb* isotopes formed via symmetric as well as asymmetric heavy ion reactions. The results are discussed in Chapter 6.

Bibliography

[1] I. Dutt, and R. K. Puri, Phys. Rev. C **81**, (2010) 064609; *ibid* **81**, (2010) 064608.

[2] P. Mӧller, J. R. Nix, W. D. Myers, and W. J. Swiatecki, At. Data Nucl. Data Tables **59**, (1995) 85.

[3] R. K. Gupta, M. Balasubramaniam, R. Kumar, N. Singh, M. Manhas, and W. Greiner, J. Phys. G: Nucl. Part. Phys. **31**, (2005) 631.

[4] R. Kumar, M. K. Sharma, and R. K. Gupta, Nucl. Phys. A **870**, (2011) 42.

[5] D. Jain, R. Kumar, M. K. Sharma, and R. K. Gupta, Phys. Rev. C **85**, (2012) 024615.

[6] R. Kumar, M. Bansal, S. K. Arun, and R. K. Gupta, Phys. Rev. C **80**, (2009) 034618.

[7] R. Kumar, Phys. Rev. C **84**, (2011) 044613.

[8] S. Misicu and W. Greiner, Phys. Rev. C **69**, (2004) 054601; S. Misicu and H. Esbensen, Phys. Rev. Lett. **96**, (2006) 112701; Phys. Rev. C **75**, (2007) 034606.

[9] E. F. Aguilera and J. J. Kolata, Phys. Rev. C **85**, (2012) 014603.

[10] C. Y. Wong, Phys. Rev. Lett. **31**, (1973) 766.

[11] R. K. Gupta, N. Singh, and M. Manhas, Phys. Rev. C **70**, (2004) 034608.

[12] I. Padron *et al.*, Phys. Rev. C **66**, (2002) 044608.

[13] C. Beck *et al.*, Phys. Rev. C **67**, (2003) 054602.

[14] L. C. Vaz, J. M. Alexander, and G. R. Satchler, Phys. Rep. **69**, (1981) 373.

[15] J. J. Kolata *et al.*, Phys. Rev. Lett. **81**, (1998) 4580.

[16] A. Morsad, J. J. Kolata, R. J. Tighe, X. J. Kong, E. F. Aguilera, and J. J. Vega, Phys. Rev. C **41**, (1990) 988.

[17] M. Trotta *et al.*, Phys. Rev. Lett. **84**, (2000) 2342.

[18] P. K. Rath *et al.*, Phys. Rev. C **79**, (2009)051601(R).

[19] P. R. S. Gomes *et al.*, Nucl. Phys. A **534**, (1991) 429.

[20] S. Cavallaro *et al.*, Nucl. Phys. A **513**, (1990) 174.

[21] C. P. Silva, D. Pereira, L. C. Chamon, E. S. Rossi, G. Ramirez, A. M. Borges, and C. E. Aguiar, Phys. Rev. C **55**, (1997) 3155.

[22] J. O. Newton, R. D. Butt, M. Dasgupta, D. J. Hinde, I. I. Gontchar,C.R.Morton, andK. Hagino, Phys.Rev.C **70**, (2004) 024605.

[23] Z. H. Liu *et al.*, Eur. Phys. J. A **26**, (2005) 73.

[24] E. F. Aguilera, J. J. Kolata, and R. J. Tighe, Phys. Rev. C **52**, (1995) 3103.

[25] J. O. Newton *et al.*, Phys. Rev. C **64**, (2001) 064608.

[26] J. J. Kolata *et al.*, Phys. Rev. C **69**, (2004) 047601.

[27] N. V. S. V. Prasad *et al.*, Nucl. Phys. A **603**, (1996) 176.

[28] S. Sinha, M. R. Pahlavani, R. Varma, R. K. Choudhury, B. K. Nayak, and A. Saxena, Phys. Rev. C **64**, (2001) 024607.

[29] V. Tripathi *et al.*, Phys. Rev. C **65**, (2001) 014614.

[30] E. F. Aguilera, J. J. Vega, J. J. Kolata, A. Morsad, R. G. Tighe, and X. J. Kong, Phys. Rev. C **41**, (1990) 910.

[31] E. M. Szanto *et al.*, Phys. Rev. C **41**, (1990) 2164.

[32] J. J. Vega, E. F. Aguilera, G. Murillo, J. J. Kolata, A. Morsad, and X. J. Kong, Phys. Rev. C **42**, (1990) 947.

[33] E. M. Martnez-Quiroz, E. F. Aguilera, J. J. Kolata, and M. Zahar, Phys. Rev. C **63**, (2001) 054611.

[34] A. M. Stefanini *et al.*, Phys. Rev. C **62**, (2000) 014601.

[35] L. T. Baby *et al.*, Phys. Rev. C **62**, (2000) 014603.

[36] O. A. Capurro *et al.*, Phys. Rev. C **65**, (2002) 064617.

[37] C. L. Jiang *et al.*, Phys. Rev. Lett. **93**, (2004) 12701.

[38] A. M. Stefanini *et al.*, Phys. Rev. c **73**, (2006) 034606.

[39] M. Beckerman, *et al.*, Phys. Rev. c **25**, (1982) 2.

[40] P. H. Stelson, H. J. Kim, M. Beckerman, D. Shapira, and R. L. Robinson, Phys. Rev. C **41**, (1990) 1584.

[41] C. L. Jiang, K. E. Rehm, H. Esbenses, R. V. F. Janssens, B. B. Back, C. N. Davids, J. P. Greene, D. J. Henderson, C. J. Lister, R. C. Pardo, T. Pennington, D. Peterson, D. Seweryniak, B. Shumard, S. Sinha, X. D. Tang, I. Tanihata, S. Zhu, P. Collon, S. Kurtz, and M. Paul, Phys. Rev. C. **71**, (2005) 044613.

[42] G. N. Knyazheva *et al.*, Phys. Rev. C **75**, (2007) 064602; A. M. Stefanini *et al.*, Eur. Phys. J. A **23**, (2005) 473.

[43] J. F. Liang *et al.*, Phys. Rev C **75**, (2007) 054607; J. F. Liang *et. al. ibid* **78**, (2008) 047601.

[44] S. Mitsuoka, H. Ikezoe, K. Nishio, K. Tsuruta, S. C. Jeong, and Y. Watanabe, Phys. Rev. Lett. **99**, (2007) 182701.

[45] V. E. Viola, Jr. and T. Sikkeland, Phys. Rev. **128**, (1962) 767.

Chapter 6

Dynamics of hot Yb* isotopes formed via different reaction channels

6.1 Introduction

In previous chapters, the role of deformation and orientation effects are investigated on nuclear interaction potential based on phenomenological models (i.e. various proximity potentials) and semiclassical interactions based on Skyrme energy density formalism (SEDF), and subsequently the fusion-fission cross-sections of a variety of nuclear reactions are worked out. Here, in this chapter, firstly we study the role of deformations and temperature effect independently on spin-orbit density independent and spin-orbit density dependent part which collectively gives the nuclear interaction potential derived from Skyrme energy density formalism. In addition to this, the effect of various Skyrme forces is also exercised by analyzing the fusion excitation functions of ^{160,164}Yb* nuclear systems formed using different target/projectile combinations (^{60,64}Ni+^{100}Mo and ^{16}O+^{144,148}Sm). Beside this the entrance channel effects in the decay of ^{172}Yb* are investigated by exploring the dynamics of ^{124}Sn+^{48}Ca and ^{132}Sn+^{40}Ca reactions, respectively involving stable and radioactive

Sn beams.

6.2 Role of spin saturated and unsaturated interactions in O- and Ni- based reactions

Several microscopic and analytical nuclear interaction potentials are available [1], where the contribution of spin-orbit density term is neglected by either studying the spin-saturated nuclei or by considering its contribution to be extremely small. Since nuclei with higher N/Z ratio and neutron-rich radioactive ion beams (RIBs) are extensively used in recent experiments, it was of extreme interest to see the role of spin-orbit density part V_J of nuclear interaction potential V_N in the reaction dynamics. The relevant details of spin saturated and spin unsaturated interaction potential can be seen in section 2.2.4 of Chapter 2. It is relevant to mention here that the spin-orbit part of nuclear potential is shown to contribute significantly towards the fusion cross-sections [2].

In this section of present chapter, the nuclear interaction potential is obtained by using Skyrme interaction in the semiclassical extended-Thomas Fermi (ETF) approach based on SEDF [3–5], under frozen density approximation [6]. The Skyrme nucleus-nucleus interaction potential is expressed as the sum of the spin-orbit density independent V_P and the spin-orbit density dependent V_J part of the Hamiltonian density, which in ETF approach of SEDF is a function of nucleon/ nuclear density alone, and completely eliminates the use of single-particle wave functions. The main motive here is to study the variation of spin-orbit density dependent V_J, spin-orbit density independent V_P and the total interaction potential V_N ($=V_P + V_J$) with asymmetry of colliding nuclei, their deformations (β_2), together with the 'optimum' orientations, and temperatures involved, by using different Skyrme forces having different isospin dependence, applied to data on various isotopes of CN Yb* [7–9]. The deformation and orientaton effects give rise to significant changes in barrier characteristics. For the Skyrme force, the old SIII force having a mild spin-orbit dependence and the very new GSkI and KDE0v1 forces of Agarwal *et al.* [10, 11], having strong spin-orbit dependence are used, so we were interested to see the performance of the new forces, as compared to the old established force such as SIII. The temperature effects, in spin-orbit density dependent interaction of semiclassical formalism, is included through the use of two-parameter Fermi density [12]. It may be noted that the spin-orbit interaction potential is independent of the charge of interacting nuclei, and hence the transfer of neutron or proton leads to the same result. Applications of SIII, GSkI and KDE0v1 forces are made to calculate the fusion cross-sections with in the ℓ-summed extended-Wong formula [13].

Experimental data on fusion cross-sections of compound systems ^{160,164}Yb*, formed in colliding near symmetric nuclei ^{60,64}Ni+^{100}Mo [7, 8] and asymmetric colliding nuclei ^{16}O+^{144,148}Sm [9], are obtained over a wide range of center-of-mass energies $E_{c.m.}$, spread across the Coulomb barrier. Thus, the aim is at least two-fold: (i) to study the role of spin-density dependent interaction potential V_J for various isotopes of $^{156-172}$Yb* formed by using different target/projectile combinations $^{56-72}$Ni+^{100}Mo and ^{16}O+$^{140-156}$Sm, with effects of temperature, deformations and orientation included; (ii) use of different Skyrme forces, having different spin-orbit density dependencies, for calculating the fusion excitation function of ^{160,164}Yb*, where data are available [7–9], in order to investigate the performance of these forces, particularly at below-barrier energies where the phenomenon of fusion hindrance come into picture. Furthermore, using the systematics of empirically fitted angular momentum ℓ_{max} for ^{160}Yb* and ^{164}Yb* nuclear systems, fusion cross-sections for ^{156,158,162,166,168}Yb* compound systems are also predicted. As already noted above, fusion cross-sections are calculated with in the ℓ-summed extended-Wong formula [13], knowing that Wong model works well for the near and above barrier energies, and for below barrier energies different Skyrme forces give different qualities of fits, and hence in turn gives a best fit to data without any additional

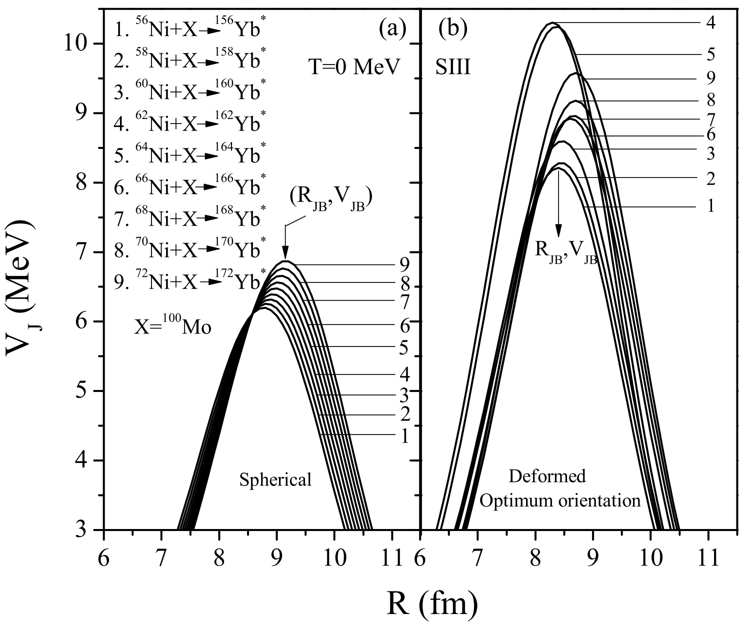

Figure 6.1: The spin-orbit interaction potential $V_J(R)$ at T=0 for increasing neutrons in the projectile/target nucleus, starting from ^{56}Ni+^{100}Mo, using (a) spherical and (b) deformed nuclei, for SIII force.

parameter fitting [14]. The calculations and results are discussed in the following:

6.2.1 Spin-orbit interaction potentials for spherical and deformed choices of nuclei

Fig. 6.1 (a) and Fig. 6.1 (b) show the spin-orbit interaction potential for spherical and deformed choices of nuclei, respectively, calculated by using the semiclassical approach with Skyrme force SIII, for various $^{156-172}$Yb* isotopes, starting with the target-projectile combination ^{56}Ni+^{100}Mo. The isotopes of Yb are formed by taking a fixed ^{100}Mo target and varying the projectile mass number by adding two successive neutrons to ^{56}Ni. It is clear from Fig. 6.1 (a) that, for spherical choice of nuclei, the barrier height V_{JB} increases slowly with increase in number of neutrons of the projectile. However, on allowing deformation effects (β_2 and optimum orientations), as shown in Fig. 6.1 (b), the barrier height V_{JB} increases systematically with enhanced magnitude, compared to spherical case, in going from ^{156}Yb* to ^{172}Yb* nuclear systems, except that for oblate shaped projectiles ^{62,64}Ni (nega-

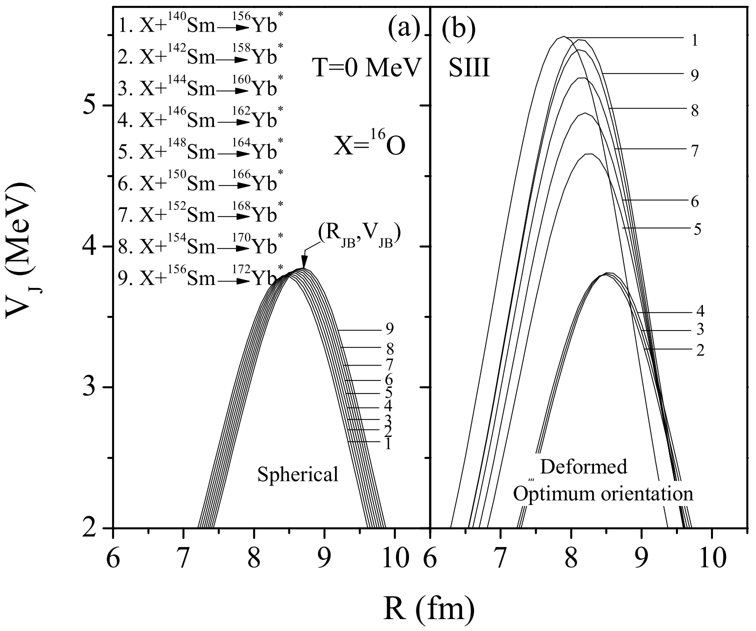

Figure 6.2: The spin-orbit interaction potential $V_J(R)$ at T=0 for increasing neutrons in the target nucleus, starting from ^{16}O+^{140}Sm, using (a) spherical and (b) deformed nuclei, for SIII force. Note the difference in scale *w.r.t.* Fig. 6.1

tive β_2 values), the barrier height and barrier distribution does not follow the usual trend. In other words, for oblate projectiles, the barrier height V_{JB} increases with a relatively larger magnitude and the barrier position R_{JB} shifts towards the smaller interaction radius. In order to generalize this result, in Fig. 6.2, asymmetric O+Sm reactions are considered which give rise to the same isotopes of Yb*. Here, ^{16}O projectile is bombarded on Sm targets by adding two successive neutrons to ^{140}Sm. It is clearly observed from Fig. 6.2 that the trend of variation of V_J remains the same as in Fig. 6.1, both for spherical as well as deformed choices of nuclei, though with a difference in the magnitude of barrier heights. Specifically, spherical spin-orbit interaction potential exhibits lowest barrier height V_{JB}, which systematically increases for prolate-deformed nuclei and subsequently the oblate-shaped nuclei show the highest barrier. There is an important point of difference in both the cases (near-symmetric and asymmetric systems) that the magnitude of barrier height decreases in moving from near-symmetric to asymmetric system, as is clearly evident from the comparison of Fig. 6.1 and Fig. 6.2. The barrier position for an asymmetric case follows the same trend as that of near-symmetric system, i.e., for spherical

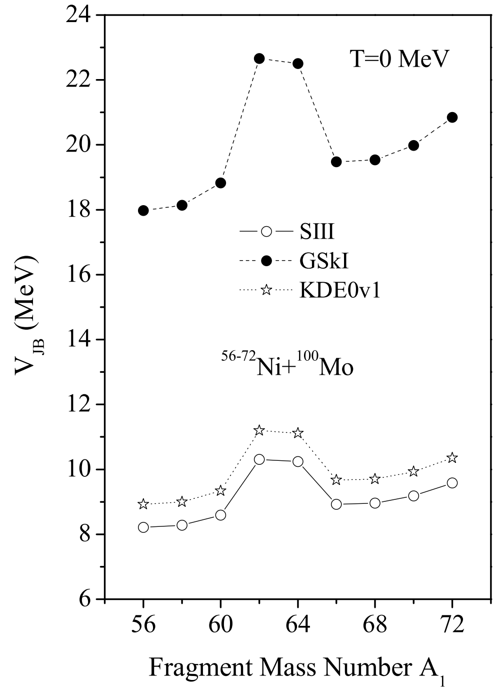

Figure 6.3: Spin-orbit interaction barrier height V_{JB} as a function of the mass number of the projectile nucleus, as the target remains fixed, using semiclassical approach with three forces SIII, GSkI and KDE0v1.

nuclei [Fig. 6.2 (a)], it shifts towards right (larger R_{JB}) with increase in number of neutrons, whereas with the inclusion of deformation effects it shifts towards smaller interaction radius, leading to a more compact configuration.

The above results are independent of the choice of Skyrme forces, as is illustrated in Fig. 6.3 for the Yb* isotopes using SIII, GSkI and KDE0v1 parameter sets. Fig. 6.3 shows the variation of barrier height V_{JB} with fragment mass of the projectile. The trend of variation in each case remains same, except for the change in magnitude. The GSkI and KDE0v1 forces show higher barriers as compared to the SIII force, possibly due to the fact that, in GSkI and KDE0v1 forces, there is an additional term included due to tensor coupling with spin and gradient.

From Eq. (2.36) in Chapter 2, it is clear that the total Skyrme nucleus-nucleus interaction potential $V_N(R)$ is the sum of spin-orbit density independent part $V_P(R)$ (mainly attractive) and the spin-orbit density dependent part $V_J(R)$ (mainly repulsive), illustrated in Fig. 6.4 at temperatures T=0 and 2 MeV for various isotopes of compound system Yb* formed in asymmetric colliding nuclei ^{16}O+$^{140-156}$Sm, using SIII force. It is to be noticed from Fig. 6.4 (a) and (b) that the barrier height V_{JB} decreases with increase of temperature but the pattern of barrier distribution still remains the same. Fig. 6.4 shows that V_J part is always repulsive, independent of temperature effects. Note that ^{140}Sm is oblate deformed, and hence gives the highest barrier. Table 6.1 shows the deformations and orientations of the interacting nuclei. The magnitude of repulsive V_{JB} and attractive V_{NB} at the nuclear potential minimum position R_B are also given in Table 6.1 for SIII and GSkI forces along with the percentage of V_{JB} in V_{NB}. It is clear from Table 6.1 that the magnitude of V_{JB} is comparatively more for GSkI force, whereas the percentage of V_{JB} in V_{NB} is more for SIII Skyrme force. Note, however, that the content of V_J in V_N is only 5-8% at the minimum position in V_N.

The orientation degree of freedom (θ_i) also modifies the barrier parameters strongly, as illustrated in Fig. 6.5 which shows the variation of spin-orbit density dependent barrier height V_{JB} for ^{16}O+^{148}Sm reaction at different values of θ_2, taking θ_1=0^0 at T=0 MeV for SIII, GSkI and KDE0v1 forces. It is clear that the barrier height V_{JB} is maximum at $\theta_2 = 90^0$ for all the three considered forces. For the inbetween configurations, V_{JB} varies smoothly as a function of the orientation angle. Note that a small change in V_{JB} and R_{JB} produce a significant change in the fusion cross section. Therefore, one may conclude that the spin-orbit part of nuclear interaction, along with deformations and orientations degrees of freedom, automatically takes care of the barrier modification effects and hence play the significant role in fusion-fission dynamics of heavy-ion reactions.

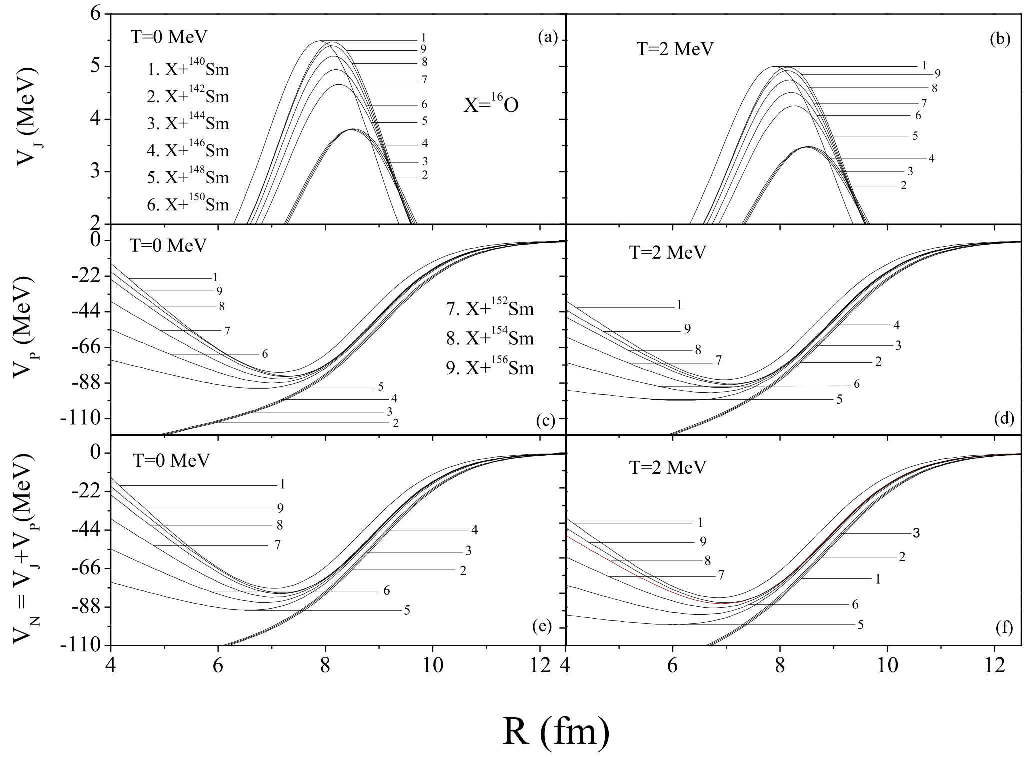

Figure 6.4: (a) and (b): the spin-orbit dependent interaction potentials $V_J(R)$; (c) and (d): the spin-orbit independent interaction potentials $V_P(R)$; and (e) and (f): the total nuclear interaction potentials $V_N(R) = V_P(R) + V_J(R)$, for isotopes of Yb* formed from ^{16}O+^{140,142,144,146,148,150,152,154,156}Sm, for deformed and oriented nuclei, at T=0 and 2 MeV, using Skyrme force SIII.

Table 6.1: The contribution of spin-orbit density dependent part V_J in nuclear interaction potential V_N for various isotopes of Yb* formed from O+Sm reactions, with inclusion of deformation and optimum orientation, using ETF in SEDF approach.

Reaction ^{16}O+^{X}Sm X	β_{21}	β_{22}	$\theta_1^{opt.}$	$\theta_2^{opt.}$	SIII force			GSkI force		
					V_{JB}	$-V_{NB}$	$\lvert\frac{V_{JB}}{V_{NB}}\rvert\times 100$ (%)	V_{JB}	$-V_{NB}$	$\lvert\frac{V_{JB}}{V_{NB}}\rvert\times 100$ (%)
140	0.0	-0.148	0	180	5.491	67.407	8.14	28.117	494.214	5.68
142	0.0	0.000	0	180	3.800	64.557	5.88	19.525	373.441	5.22
144	0.0	0.000	0	180	3.808	65.597	5.80	19.553	383.13	5.10
146	0.0	0.000	0	180	3.814	66.613	5.72	19.531	393.269	4.96
148	0.0	0.161	0	90	4.657	66.524	7.00	23.743	424.875	5.58
150	0.0	0.206	0	90	4.948	68.089	7.26	25.087	459.302	5.46
152	0.0	0.243	0	90	5.196	67.204	7.73	26.261	458.154	5.73
154	0.0	0.270	0	90	5.396	69.173	7.80	27.134	460.064	5.89
156	0.0	0.279	0	90	5.468	69.487	7.86	27.39	468.328	5.84

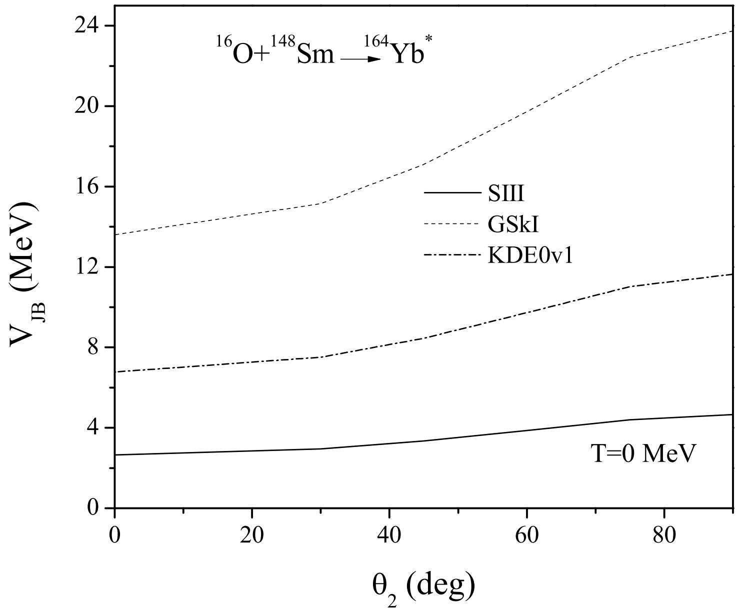

Figure 6.5: Spin-orbit interaction barriers V_{JB} for ^{16}O+^{148}Sm reaction at different θ_2 values, keeping $\theta_1 = 0^0$ fixed, for the three Skyrme forces SIII, GSkI and KDE0v1 at T=0 MeV.

6.2.2 Fusion cross-sections for $^{156-168}$Yb* using different Skyrme forces with in framework of ℓ-summed Wong model

First of all, the effect of using different Skyrme forces for calculating the interaction barriers are studied for the case of ℓ=0 in ^{160}Yb*. Fig. 6.6 (a) shows the spin-orbit density dependent interaction potential $V_J(R)$ for ^{60}Ni + ^{100}Mo → ^{160}Yb* reaction at T=0 with fixed optimum orientations, using various Skyrme forces in frozen density approximation. It is to be noticed that the Skyrme forces GSkI, SSk, KDE0v1 and MSL0, having tensor coupling with spin and gradient term, all give higher spin-orbit interaction barrier V_{JB}, as compared to SIII, SLy4 and SkM* forces where tensor coupling is not included. However, it is clear from Table I that the percentage contribution of V_{JB} in V_{NB} is small for GSkI, as compared to SIII force, reflected in total interaction potential shown in Fig. 6.6 (b) for the same reaction. The interesting result is that the barrier characteristics (height, position and curvature) are strongly influenced with the change in Skyrme forces. Remembering that the

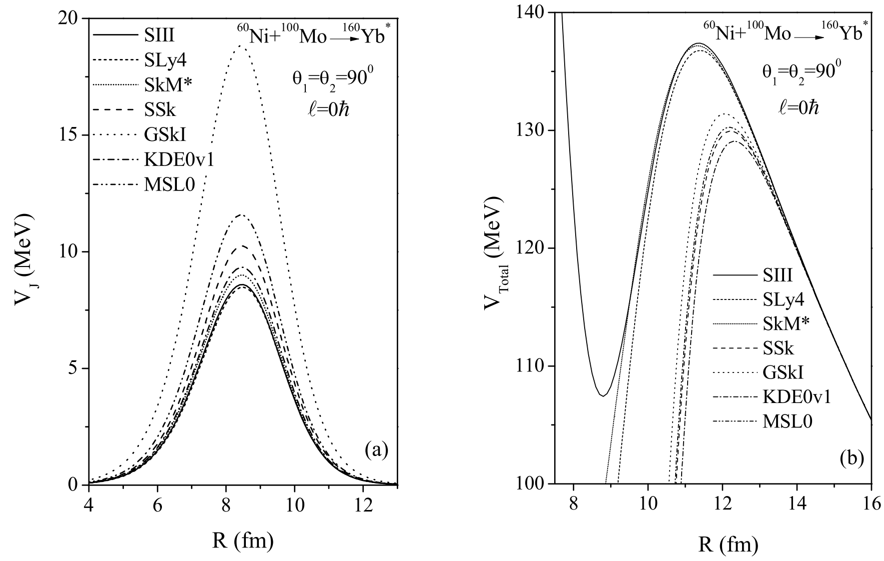

Figure 6.6: (a) Spin-orbit and (b) total interaction potential for ℓ=0 case of ^{60}Ni+^{100}Mo reaction at fixed orientations, using various Skyrme forces.

behavior of nucleus-nucleus interaction potential $V_N(R)$ is attractive, whereas the spin-orbit density dependent potential $V_J(R)$ is repulsive, the barrier height V_B in total interaction potential V_{Total} is largest for SIII, contrary to the corresponding V_{JB} profile. The same result follows for ^{16}O+^{144}Sm→^{160}Yb* reaction. As SIII force has the highest barrier and KDE0v1 has the lowest barrier, we choose SIII, GSkI and KDE0v1 Skyrme forces, all having different barrier characteristics, for calculating the fusion cross sections.

Fig. 6.7 shows the calculated fusion cross sections as a function of center-of-mass energy $E_{c.m.}$ for isotopes of CN ^{160,164}Yb* formed in ^{60,64}Ni+^{100}Mo reactions, using the three illustrated Skyrme forces within the ℓ-summed Wong model, compared with the experimental data. In Fig. 6.7 (a), we compare the fusion cross-section obtained with and without spin-orbit interaction for SIII force. This comparison has been done for SIII force as spin-orbit contribution is more as compared to other forces (see Table 6.1). It is clearly observed that with the addition of spin-orbit part, cross-sections decrease by about 5-8% (specially at below barrier energies). This means that the fusion cross-sections are not significantly affected by the inclu-

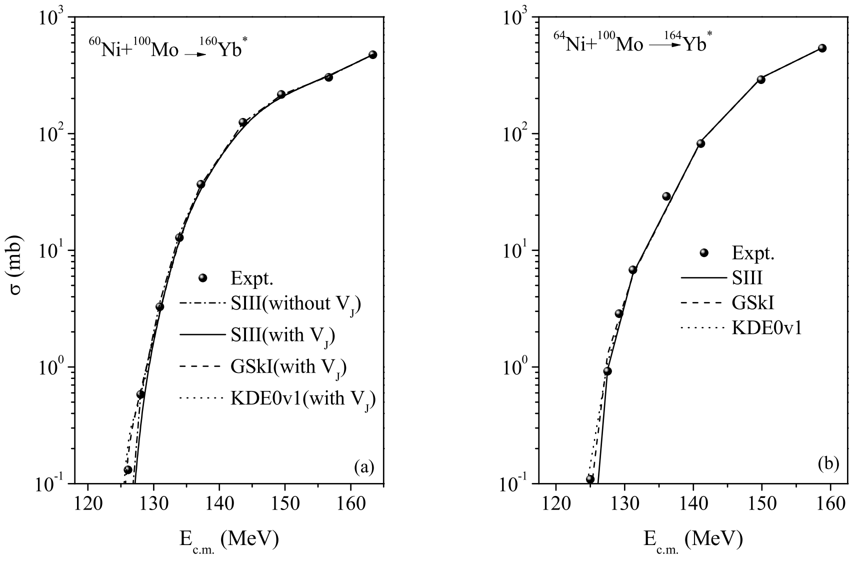

Figure 6.7: Fusion cross section as a function of $E_{c.m.}$, calculated by using the ℓ-summed Wong model, integrated over θ_i, for Skyrme forces SIII, GSkI and KDE0v1, and compared with experimental data for (a) ^{60}Ni+^{100}Mo, and (b) ^{64}Ni+^{100}Mo systems.

sion of spin dependent interaction. It is relevant to mention here that, the further calculations are done with the inclusion of spin-orbit interaction term. Apparently, the extended-Wong model calculations for GSkI and KDE0v1 forces fit the data nicely at both the above- as well as below-barrier energies, but the SIII force shows significant underestimation of cross section at below-barrier energies, and hence needs barrier modifications in order to fit the data. Apparently, one could find another force, with barrier properties similar to that of GSkI or KDE0v1, that would fit the ^{60,64}Ni+^{100}Mo data. For the best fitted GSkI and KDE0v1 forces (GSkI force being better in both the cases, as was also shown earlier for ^{164}Yb [14]), the deduced ℓ_{max} values vary smoothly as a function of $E_{c.m.}$, but for the SIII force where the fit is not so good at sub-barrier energies, $\ell_{max}(E_{c.m.})$ varies erratically, which could be smoothed by adding appropriate barrier lowering empirically, not carried out here (however, see Fig. 6(c) in [14]).

Fig. 6.8 shows the fusion cross-sections for ^{16}O+^{144,148}Sm reactions forming same ^{160,164}Yb* isotopes, calculated by using the ℓ-summed Wong model with the

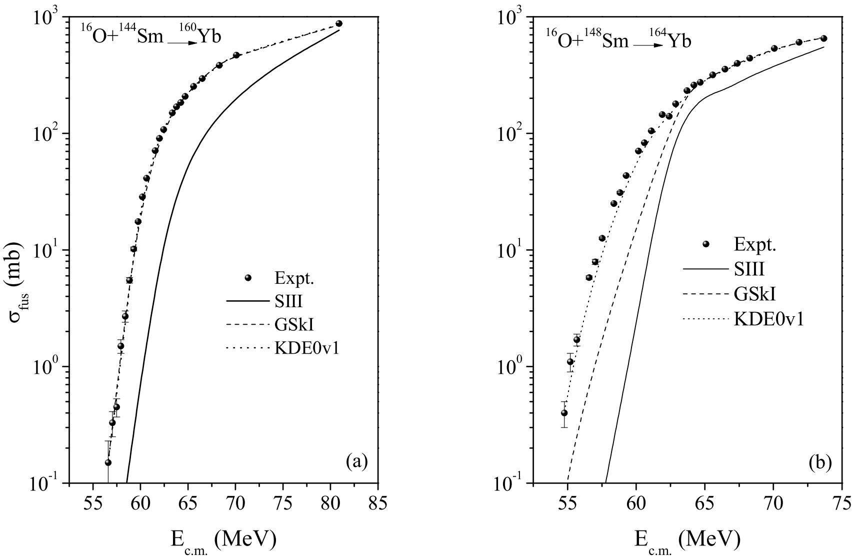

Figure 6.8: Same as Fig. 6.7, but for (a) ^{16}O+^{144}Sm, and (b) ^{16}O+^{148}Sm systems.

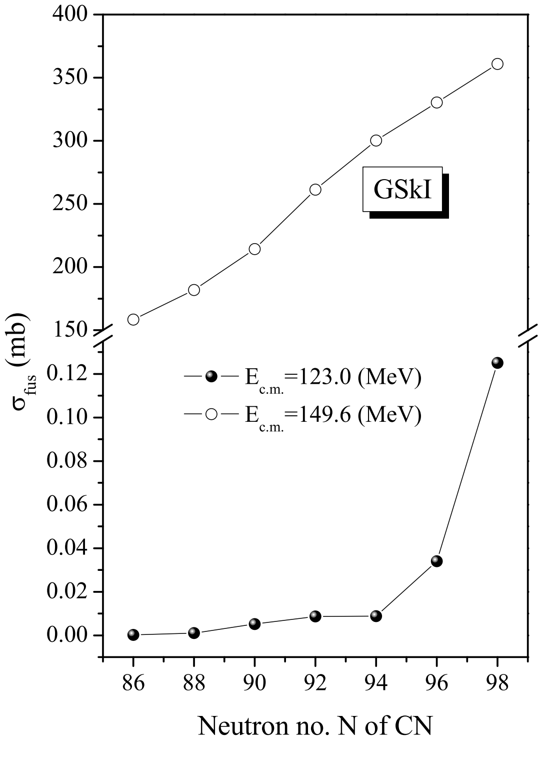

Figure 6.9: Variation of fusion cross-section with increasing neutron number of CN Yb*, formed from Ni+Mo reactions, using the GSkI force, at above- and below-barrier energies.

Table 6.2: Fusion cross-section and the maximum value of angular momentum (ℓ_{max}) used for different Ni-induced reactions with ^{100}Mo, at $E_{c.m.}$ above and below the Coulomb barrier, using Skyrme force GSkI. Note, ℓ_{max} for ^{160}Yb* and ^{164}Yb* are the empirically fitted values.

CN	N	$E_{c.m.}$=123.0 (MeV)		$E_{c.m.}$=149.6 (MeV)	
	(CN)	$\sigma_{fus}(mb)$	ℓ_{max} ($\hbar$)	σ_{fus} (mb)	ℓ_{max} ($\hbar$)
^{156}Yb*	86	0.0002	1	158.37	36
^{158}Yb*	88	0.0011	2	181.83	39
^{160}Yb*	90	0.0051	3	214.32	42
^{162}Yb*	92	0.0087	2	261.36	47
^{164}Yb*	94	0.0088	1	300.30	51
^{166}Yb*	96	0.0340	2	330.27	54
^{168}Yb*	98	0.1250	3	360.95	57

Skyrme forces SIII, GSkI and KDE0v1. The important result presented by this extended-Wong model calculation is that ^{16}O + ^{148}Sm reaction shows stronger fusion-hindrance than the ^{16}O + ^{144}Sm reaction. Furthermore, only the KDE0v1 Skyrme force with lowest barrier height [see Fig. 6.6 (b))] fits the experimental data of ^{16}O+^{148}Sm reaction, and the other two forces need some barrier modification. On the other hand, for ^{16}O+^{144}Sm reaction, both GSkI and KDE0v1 forces have the appropriate barrier characteristics and fit the data nicely, but only SIII force needs the modification of barrier for fitting the data. Note that, since barrier properties are the main ingredient of the Wong model, significant difference between the predications of the older SIII and the new GSkI and KDE0v1 forces arises due to their different barrier characteristics. The comparison of data is better for new Skyrme forces as the new forces have a stronger isospin and asymmetry dependence.

Finally, an effort is made to estimate the fusion cross-sections for ^{162}Yb* and ^{156,158,166,168}Yb*, i.e., the missing isotope in the middle and two isotopes on either side of ^{160}Yb* and ^{164}Yb* whose available experimental data [7, 8] are fitted above.

For the fitting parameter ℓ_{max}, a linear interpolation/ extrapolation is carried out, i.e., for ^{162}Yb* the average of ℓ_{max}-values of ^{160}Yb* and ^{164}Yb* is taken, and for ^{156,158,166,168}Yb* we choose ℓ_{max} with in the range of ±3 units of variation. The ℓ_{max}-values and the corresponding fusion cross-sections for all the considered even mass $^{156-164}$Yb* are listed in Table 6.2 at two $E_{c.m.}$ energies, one above and another below the Coulomb barrier, for use with GSkI force. The GSkI force is chosen to predict the fusion cross-section of selected Yb* isotopes since it is shown in Fig. 6.7 to give a relatively better agreement with data for Ni-induced reactions. The variation of fusion cross-section with neutron number N of Compound nucleus Yb*, formed using various isotopes of Ni with fixed ^{100}Mo target at $E_{c.m.}$=123.0 MeV (below barrier) and 149.6 MeV (above barrier), is shown in Fig. 6.9. Apparently, the cross-sections increase almost exponentially with the increase in neutron number of CN, for incident energies on either side of the Coulomb barrier.

6.3 Entrance channel effect in decay of ^{172}Yb* formed using stable and radioactive beams

A number of experiments have been performed using radio active ion beams (RIBs) to study evaporation residue (ER) and fusion-fission cross sections, and comparisons were made with reactions involving stable beams [15, 16]. Simultaneously, a significant amount of information has been extracted through theoretical calculations as well. Recently ^{172}Yb* compound system was populated by Kolata et al [17] using stable and radioactive Sn-beams on Ca-targets. Fusion excitation functions were measured at energies above and below the Coulomb barrier for ^{124}Sn+^{48}Ca and ^{132}Sn+^{40}Ca reactions. A significant enhancement in ER cross section at below barrier energies was observed for ^{132}Sn+^{40}Ca reaction. It is relevant to mention here that the entrance channel effect is studied in chapter 4, for ^{190}Pt* nucleus formed using two different radioactive beams (i.e. ^{132}Sn+^{58}Ni and ^{126}Sn+^{64}Ni reactions).

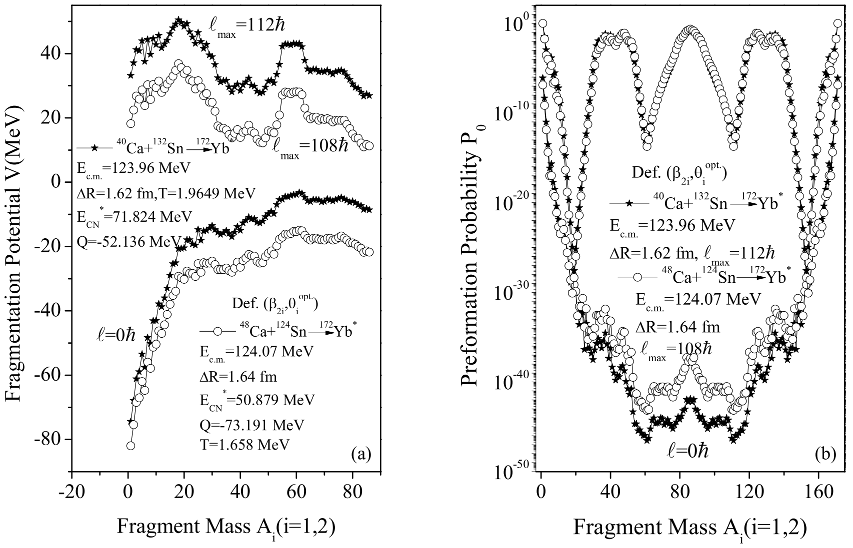

Figure 6.10: (a) Fragmentation potential $V(A_2)$ for the decay of ^{172}Yb*, formed in two different entrance channels ^{124}Sn+^{48}Ca and ^{132}Sn+^{40}Ca are compared at comparable center of mass energy for deformed choice of nuclei at extreme ℓ-values using proximity formula. (b) Same as part (a) but for preformation probability.

Moreover, there was no data at comparable energies for both the entrance channels. However, the experimental works of Kolata [17] offer an opportunity to study the entrance channel effect on the decay of ^{172}Yb* at comparable energies spread across the Coulomb barrier. In this section, the entrance channel dependence in the decay of hot and rotating ^{172}Yb* compound system is analysed using dynamical cluster decay model [18,19], in which nuclear interaction potential is obtained by pocket formula [20]. Beside this, the fusion enhancement is also studied through the available fusion evaporation residue cross section.

Fig. 6.10 (a) shows the fragmentation potential for the decay of $^{172}Yb^*$ compound system formed in two entrance channels ^{124}Sn+^{48}Ca and ^{132}Sn+^{40}Ca at comparable energies (i.e. $E_{c.m.}$=124.07 and 123.96 MeV respectively) around the Coulomb barrier. It is clear from Fig. 6.10 (a) that except the change in magnitude, the potential energy surface (PES) remains the same despite the fact that these reactions have positive and negative Q-value neutron transfer. The maximum angular

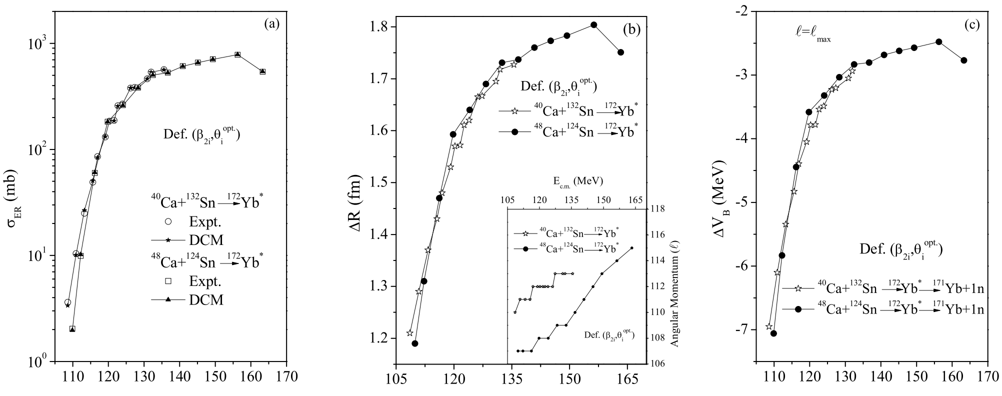

Figure 6.11: (a) Experimental ER cross section [17] is compared with the one calculated using DCM for the decay of ^{172}Yb*, formed in two different entrance channels ^{124}Sn+^{48}Ca and ^{132}Sn+^{40}Ca at comparable $E_{c.m.}$. (b) Neck-length parameter ΔR for the two reaction as in part (a). The deduced maximum value of angular momentum at different energies for two reactions is shown in the inset. (c) Same as part (b) but for deduced values of barrier modification ΔV_B at ℓ_{max}.

momentum (ℓ_{max}) changes only by few units. It is to be noted here the Q-value of these reactions differ by an order of around 20 MeV, and hence the corresponding temperature also differ significantly but still the decay pattern is the same except magnitude. It is clear from Fig. 6.10 (a) that for s-wave (ℓ=0), the light particles are most probable however at higher ℓ-values the HMFs and fission fragments start competing with LP cross section or equivalently ER component. Fig. 6.10 (b) shows the preformation probability at the same energies as in Fig. 6.10 (a). The fragments which are energetically more favorable, i.e. minimum in $V(A_2)$, corresponds to maxima in P_0. Further it is clear that asymmetric and symmetric fission fragments are equally probable. Although there is slight change in the magnitude of preformation probability but the overall trend remains the same. The ER cross-section is the sum of light particle channels cross-section i.e. $\sigma_{ER} = \sum_{A_2=1}^{4} \sigma(A_2)$. For A_2=1, 2, and 3, the energetically favored fragment in our calculations is neutron, however for A_2=4, it comes out to be ^4H.

In order to study the fusion enhancement, ER cross section is fitted for the decay of $^{172}Yb^*$ formed in different entrance channels. Fig. 6.11 (a) shows the comparison of experimental data [17] and the theoretical calculations using DCM. A nice fit to the data is obtained for ^{124}Sn+^{48}Ca and ^{132}Sn+^{40}Ca reactions. The fission cross section is one order of magnitude smaller than the ER cross section at highest energy for maximum allowed ΔR. Fig. 6.11 (b) shows the ΔR obtained by fitting the experimental data as shown in Fig. 6.11 (a). The variation of ℓ_{max} as a function of $E_{c.m.}$ are shown in inset of Fig. 6.11 (b). This figure shows that ΔR is lower for ^{132}Sn+^{40}Ca except at few lowest energies and ℓ_{max}, though do not change in large units, but increases with $E_{c.m.}$. The step like behavior of ℓ_{max} at various energies is due to the fact that ℓ-values are integers. Fig. 6.11 (c) shows the variation of ΔV_B, extracted for $1n$ case, as $1n$ is the major contributor to ER cross section. It is clear that for ^{132}Sn+^{40}Ca reaction, barrier modification ΔV_B (=V_B-$V(R_a)$) decreases in magnitude as compare to that of ^{124}Sn+^{48}Ca. Thus the experimental data demands the first turning point (R_a) to be more close to barrier position (R_B) in order to account for the data. It is to be noted here that at top of the barrier, transmission is maximum and corresponds to maximum cross-section. Increasing ΔR means approaching the top of the barrier i.e. entry and exit points get closer to each other. Thus there is some signature of fusion enhancement when variation of ΔR and ΔV_B are carefully observed in reference to cross-section at lower energies. However, if different ΔR is considered for the different regions of fragments mass (A_2) [21], then increase in ΔR does not always means increase in cross-section due to change in relative preformation probability of various contributing fragments. The relevant details are also listed in Table 6.3. It is also clear from the inset of Fig. 6.11 (b) that ℓ_{max} is few order of magnitude higher for the case of ^{132}Sn+^{40}Ca as compare to ^{124}Sn+^{48}Ca at comparable lower energies. This shows that higher ℓ-values are contributing for ^{132}Sn+^{40}Ca reaction so there is entrance channel dependence which is in agreement with the experimental data in which they observe that the two reactions populate different state of compound system. Hence the entrance channel dependence of compound system depends on the excitation energy if RIB is used in place of stable beam.

The ER cross-section for ^{132}Sn+^{40}Ca reactions are predicted at higher energies using same ΔR as that of ^{124}Sn+^{48}Ca reaction, as the systematics of ΔR shows that they almost coincide with each other at above barrier region. The deduced ℓ_{max} for three reaction at various energies are also listed in Table 6.3 along with fitted and experimental ER cross-section, neck-length parameter and barrier modification.

6.4 Conclusions

An attempt is made to study the isotopic dependence of spin-orbit density interaction potential in the semiclassical ETF approach for Yb* nuclear systems. In addition to this, the entrance channel and fusion enhancement effects are also studied in the decay of ^{172}Yb* with in the framework of dynamical cluster decay model.

Firstly, to study the isotopic effect of spin unsaturated interaction potential, we considered nine even-mass Compound system $^{156-174}$Yb* formed by using the combinations of two different incoming systems $^{56-74}$Ni+^{100}Mo and ^{16}O+$^{140-156}$Sm. It is observed that the spin-orbit density dependent barrier heights are lower for spherical nuclei compared to the deformed case, and that with the increase in number of neutrons in either the projectile or the target, both the barrier height and position increase for spherical systems. In the deformed case, however, the spin-orbit density dependent barrier of the isotope of Yb formed via oblate-shaped nuclei show the highest barrier-height and smallest barrier-position, which for spherical nuclei have the lowest barrier-height and largest barrier-position. On the other hand, the prolate-shaped nuclei show barrier profile in between the spherical and oblate-shaped nuclei. The content of spin-orbit density dependent term is found to be only 5-10% of the spin-orbit density independent potential, and act opposite to each other (one repulsive and another attractive), nearly independent of the inclusion of temperature effects.

Since deformation and orientation degrees of freedom, and the use of differ-

Table 6.3: The ER cross section and relevant variables for ^{124}Sn+^{48}Ca and ^{132}Sn+^{40}Ca, forming the same compound system $^{172}Yb^{*}$ are calculated using DCM at different excitation energies. The experimental data from Ref. [17] is also listed. The predicted ER cross-section for ^{132}Sn+^{40}Ca are also tabulated for above barrier energies. The barrier modification ΔV_B is for $1n$ channel at ℓ=ℓ_{max}.

$E_{c.m.}$ (MeV)	T (MeV)	ℓ_{max} ($\hbar$)	ΔR (fm)	ΔV_B (ℓ=ℓ_{max}) (MeV)	σ_{ER} (=$\sum_{A_2=1}^{4}\sigma(A_2)$) (mb)	
					DCM	Expt.
^{124}Sn+^{48}Ca $\rightarrow$ $^{172}Yb^{*}$ $\rightarrow$ A_1+A_2 (Q_{in}=-73.191 MeV)						
109.90	1.412	107	1.190	-7.059	1.97	2.04
112.23	1.455	107	1.310	-5.833	10.2	9.92
116.20	1.526	107	1.470	-4.445	60.5	60.0
119.80	1.588	108	1.593	-3.580	182	182.36
124.07	1.658	108	1.640	-3.321	260	261.36
128.30	1.724	109	1.690	-3.034	380	382.60
132.49	1.787	109	1.731	-2.833	503	502.50
136.68	1.849	110	1.737	-2.803	528	529.83
140.87	1.908	111	1.760	-2.683	608	609.62
145.10	1.966	112	1.773	-2.619	658	659.99
149.30	2.022	113	1.783	-2.569	707	708.88
156.28	2.114	114	1.804	-2.478	784	781.80
163.29	2.197	115	1.751	-2.769	541	539.74
^{132}Sn+^{40}Ca $\rightarrow$ $^{172}Yb^{*}$ $\rightarrow$ A_1+A_2 (Q_{in}=-52.136 MeV)						
108.59	1.745	110	1.210	-6.952	3.37	3.62
110.90	1.779	111	1.290	-6.103	10.10	10.43
113.28	1.815	111	1.370	-5.345	26.70	25.01
115.62	1.848	111	1.430	-4.829	50.50	49.17
116.94	1.867	112	1.480	-4.396	83.70	85.76
119.14	1.898	112	1.530	-4.050	132	131.12
120.26	1.914	112	1.570	-3.784	185	185.05
121.62	1.933	112	1.572	-3.780	186	187.63
122.65	1.947	112	1.611	-3.537	256	257.88
123.96	1.964	112	1.620	-3.489	267	268.48
126.20	1.995	112	1.665	-3.228	379	379.13
127.34	2.010	113	1.667	-3.202	382	384.36
130.90	2.056	113	1.695	-3.05	463	463.32
132.00	2.070	113	1.718	-2.936	535	536.19
135.59	2.116	113	1.727	-2.907	564	566.23
140.87	2.181	114	1.760	-2.7306	674[1]	-
145.10	2.231	114	1.773	-2.693	694[1]	-
149.30	2.281	114	1.783	-2.663	713[1]	-
156.28	2.360	115	1.804	-2.571	765[1]	-

---

[1] symbolizes predicted ER cross-section.

ent Skyrme forces, change the barrier characteristics significantly, so the effects of including the same is tested in the calculation of fusion excitation function of ^{60,64}Ni+^{100}Mo and ^{16}O+^{144,148}Sm reactions within framework of ℓ-summed Wong model. The interesting result is that the new forces GSkI and KDE0v1 perform better than the old Skyrme SIII force. Use of different Skyrme forces, having different barrier characteristics, suggests that the choice of proper Skyrme force is essential for addressing the data in below-barrier energy region, and hence the associated fusion-hindrance phenomenon. Apparently, for a careful choice of the Skyme force, a stronger isospin and asymmetry dependence is required for data at sub-barrier energies. Finally, fusion cross-sections are predicted for various isotopes of Yb* (with A=156,158,162,166,168), using the systematics of already measured cross-sections for ^{160}Yb* and ^{164}Yb* nuclei.

Further the DCM is used to study the decay of CN $^{172}Yb^*$ formed with stable and radioactive ion beam of Sn in order to investigate the entrance channel effect. The experimental data of evaporation residue (ER) cross section, available at above as well as below barrier energies, is fitted by varying the neck length parameter (ΔR). The deformation is included up to β_2 along with hot optimum orientation. The decay pattern of $^{172}Yb^*$ formed in ^{124}Sn+^{48}Ca and ^{132}Sn+^{40}Ca and corresponding preformation probability, maximum angular momentum (ℓ_{max}), ΔR and barrier modification (ΔV_B) are studied for the entrance channel dependence and fusion enhancement at comparable center-of-mass energy ($E_{c.m.}$). It is also observed that there is decrease in ΔV_B, i.e. increase in fusion probability for ^{132}Sn+^{40}Ca, which lead to fusion enhancement at sub barrier energies. Thus increase in N/Z ratio affect the yield significantly at low energies. The predictions are made for ER cross section for ^{132}Sn+^{40}Ca at above barrier energies.

After having detailed qualitative and quantitative analysis of fusion-fission dynamics using phenomenological (proximity theorem based) and semiclassical (SEDF based) nuclear interactions and their subsequent dependence on nuclear deformations, orientations, angular momentum, excitation energies, spin orbit potential etc. in Chapter 3-6, we summarize and conclude our results in the next chapter. A brief scope for future extension of this work is also described for further progress in the related area of fusion fission dynamics and associated nuclear structure effects.

Bibliography

[1] C. Ngo *et al.*, Nucl. Phys. **A240**, 353 (1975); *ibid.* **A252**, 237 (1975); H. Ngo and C. Ngo, Nucl. Phys. **A348**, 140 (1980); D. M. Brink and Fl. Stancu, Nucl. Phys. **A299**, 321 (1978); Fl. Stancu and D. M. Brink, Nucl. Phys. **A270**, 236 (1976).

[2] R. K. Puri and R. K. Gupta, Phys. Rev. C **45**, 1837 (1992).

[3] B. Grammoticos and A. Voros, Ann. Phys. **123**, 359 (1979); *ibid.* **129**, 153 (1980).

[4] M. Brack, C. Guet, and H. -B. Hakansson, Phys. Rep. **123**, 275 (1985).

[5] J. Bartel and K. Bencheikh, Eur. Phys. J. A **14**, 179 (2002).

[6] G. -Q. Li, J. Phys. G: Nucl. Part. Phys. **17**, 1 (1991).

[7] A. M. Stefanini *et al.*, Eur. Phys. J. A **49**, 63 (2013).

[8] C. L. Jiang *et al.*, Phys. Rev. C. **71**, 044613 (2005).

[9] J. R. Leigh *et al.*, Phys. Rev. C. **6**, 52 (1995).

[10] B. K. Agrawal, S. Shlomo, and V. Kim Au, Phys. Rev. C **72**, 014310 (2005).

[11] B. K. Agrawal, S. K. Dhiman, and R. Kumar, Phys. Rev. C **73**, 034319 (2006).

[12] R. K. Gupta, D. Singh and W. Greiner, Phys. Rev. C **75**, 024603 (2007).

[13] R. Kumar, M. Bansal, S. K. Arun, and R. K. Gupta, Phys. Rev. C **80**, 034618 (2009).

[14] R. Kumar, M. K. Sharma, and R. K. Gupta, Nucl. Phys. A **870-871**, 42 (2011).

[15] W. S. Freeman *et al.*, Phys. Rev. Lett. **50**, 1563 (1983).

[16] K. T. Lesko *et al.*, Phys. Rev. C **34**, 2155 (1986); J. F. Liang *et al.*, ibid. **75**, 054607 (2007); **78**, 047601 (2008).

[17] J. J. Kolata, A. Roberts, A. M. Howard, D. Shapira, J. F. Liang, C. J. Gross, R. L. Varner, Z. Kohley, A. N. Villano, H. Amro, W. Loveland, and E. Chavez, Phys. Rev C **85**, 054603 (2012).

[18] R. K. Gupta, Lecture Notes in Physics 818, *Clusters in Nuclei*, ed C. Beck, Vol. I, (Springer Verlag, 2010) p 223.

[19] R. K. Gupta and M. Bansal, Int. Rev. Phys. (IREPHY) **5**, 74 (2011).

[20] J. Blocki, J. Randrup, W. J. Swiatecki, and C.F. Tsang, Ann. Phys. (N.Y.) **105**, 427 (1977).

[21] R. Kumar and R. K. Gupta, Phys. Rev. C. **79**, 034602 (2009).

Chapter 7

Summary and outlook

In this thesis, the ℓ-summed Wong formula and Dynamical Cluster Decay Model (DCM) have been exploited respectively to address the formation and decay process of heavy ion collisions at low energy region. The DCM is based on well known Quantum Mechanical Fragmentation Theory (QMFT)and has been developed to study the decay of hot and rotating compound nuclei (CN), including the effects of deformation and orientation degree of freedom of outgoing fragments/ nuclei. In DCM, fragments are required to be preformed with certain probability P_0 before penetrating the interaction barrier. Thus, the cluster preformation probabilities contain the structure effects of the CN, which provides the possibility of studying the fine or sub-structure in fission products. The DCM is worked out in terms of only one parameter, the neck-length parameter represents the reaction time scale and also refers to the actual used barrier height and consequently to the concept of barrier lowering ΔV_B which tackles the fusion hindrance/enhancement phenomena. For the fusion reactions, the ℓ-summed Wong formula is shown to be the same as the dynamical cluster-decay (DCM) model expression with a condition of fragment Preformation P_0^ℓ=1 for all the angular momentum ℓ values.

An overview of relevant status of fusion-fission and related aspects have been discussed in Chapter 1. A broad classification of heavy ion reactions and various approaches to handle the nuclear interactions are described in addition to the outline of thesis in this chapter. The details of the methodology used i.e the dynamical cluster decay model and ℓ-summed wong formula is discussed in Chapter 2 with nuclear interaction potential obtained from various proximity potentials as well as from Skyrme energy density formalism. The mothodology has been employed to address the fusion-fission dynamics governed via heavy ion collisions at low energy region.

Understanding of nucleus-nucleus interaction potential is quite crucial in the study of the heavy-ion reactions. For that the various nuclear proximity potentials are used in this thesis to understand the nuclear reaction dynamics. Firstly, in Chapter 3 the use of different Skyrme forces in DCM via the nuclear proximity potential obtained from semiclassical extended Thomas Fermi (ETF) approach in Skyrme energy density formalism (SEDF) under frozen density approximation is applied to study the fusion-fission dynamics of ^{132}Sn+^{64}Ni→^{196}Pt* reaction at below as well as above the Coulomb barrier energies. Within the DCM, it is found that for the chosen three Skyrme forces (GSkI, SSk and SIII) and Blocki *et al.* potential, the decay process presents the similar pattern for the fragmentation potential as well as the pre-formation probability, indicating that the asymmetric fission contributes more than the symmetric fission. The DCM fits the experimental data for σ_{ER}, but the fission data at the highest two/ or three center of mass energies $E_{c.m.}$ could not be addressed for either of the nuclear interaction potential. At these higher $E_{c.m.}$ values, the quasi fission (qf) process seems to compete with the fission and the sum of these two, i.e. $\sigma_{fiss} + \sigma_{qf}$, fits the available data nicely. The role of changing the radioactive ^{132}Sn beam to a stable ^{112}Sn beam is also studied which shows that the asymmetric fission fragments contribute for ^{196}Pt* which changes to a symmetric one for ^{176}Pt*, independent of the choice of nuclear interaction potential. In addition to this, an application of ℓ-summed Wong formula with explicit angular momentum and barrier modification effects, arising due to the use of different Skyrme forces is made to fit the fusion excitation function for above mentioned reaction. It is observed that out of the three illustrated Skyrme forces i.e SIII, GSkI and SSk, the last two forces are able to fit the data with smooth variation of ℓ_{max} with centre of mass energy. However, SIII force gives underestimation of reported data at near and below barrier energies, which calls for barrier modification effects and hence justifies the use of different Skyrme interaction in reference to heavy ion induced reaction dynamics. The deformation and temperature effects and dully incorporated in the formation and decay analysis of ^{196}Pt* nucleus.

In addition to the dynamics of ^{196}Pt* formed in ^{132}Sn + ^{64}Ni reaction via ℓ-summed wong formula and DCM approach by employing nuclear interactions based on SEDF, an attempt is made to analyze the entrance channel effects in ^{190}Pt* CN formed via different target and projectiles in addition to comprehensive study on the dynamics of various isotopes of Pt* produced by stable and radioactive beams. For the purpose various proximity potentials (i.e. Prox 77, Prox 88, mod-Prox 88 and Denisov 2002) and level density parameters are used and the results are discussed in Chapter 4. In order to do a comparison between the two incoming channels, the same centre-of-mass energy $E_{c.m.} \approx 190$ MeV is chosen. It is observed that for both the channels same fragments contribute to the decay process, indicating that the decay is independent of the mode of its formation. This observation holds good for spherical as well as deformed choice of fragmentation and it persists even with the use of different nuclear proximity potentials and level density parameter. Beside this the fission mass distribution of Pt^* isotopes is investigated and consequently the barrier modification is estimated to account for the phenomena of fusion hindrance. With the neutron excess in the projectile/target, the barrier lowering (ΔV_B) decreases (less negative), hence fusion hindrance also decreases in agreement with experimental observation. Alternatively the fusion hindrance phenomena is also dealt with in the framework of extended Wong model. The fusion excitation function are also studied for ^{132}Sn+^{58}Ni reaction at above and below the Coulomb barrier using different proximity potentials. It is found that mod-Prox 88 fits the data nicely at above as well as below the Coulomb barrier energies whereas other potentials require barrier modification in explaining the fusion hindrance phenomena.

After carrying out an extensive work on formation and decay path of Pt isotopes using variety of nuclear interactions, by employing deformation, orientation, temperature, angular momentum etc effects wherever applicable, a further attempt is made by investigating the barrier height and barrier positions of some 52 colliding nuclei with mass asymmetry parameter in range of 0 to 0.96 (i.e. smaller to superheavy nuclear systems) within framework of wong formula. Various proximity potentials i.e. Prox 77, Prox 88, Prox 00, Bass 80 and Denisov DP are used to extract barrier characteristics and the results are discussed in Chapter 5. It is observed that barrier height and barrier position get modified considerably with the inclusion of deformations for all the nuclear proximity potential considered. The fusion barrier heights get improved (with in $\sim \pm 5\%$ except for Prox 00) and hence come closer to the empirical barriers. As an application, these deformation dependent nuclear potentials are used for calculating fusion cross-sections of O-, Ca- and Ni-based reactions in medium mass region in reference to available data on fusion cross-sections at around and above the Coulomb barrier energies. For Ni- based reactions Prox 88 comes closer to the experimental data as compared to other potentials whereas for O and Ca- based reactions, Prox 77 seems a better option at below and near barrier energies. At above barrier energies Bass 80 and Denisov DP compete each other and are comparable with the experimental data. It is concluded that the deformation effects play significant role to address the data at near barrier energies.

It is important to note that so far the role of deformations, orientations and excitation energies etc. is investigated in reference to nuclear potential derived via various promity theorems and SEDF based interactions to address fusion-fission and related dynamics. It is of further interest to investigate the exclusive role of deformations and temperature effects independently on spin-saturated and spin-unsaturated interactions which collectively governs the nuclear potential in the semiclassical ETF approach. The results are discussed in Chapter 6 for a variety of colliding nuclei by considering symmetric and asymmetric reaction partners. This exercise is made for nine even-mass $^{156-174}$Yb* isotopes formed via two different incoming systems $^{56-74}$Ni+^{100}Mo and ^{16}O+$^{140-156}$Sm, using both the spherical and deformed choice of nuclei. It is observed that, for spherical choice of nuclei, the barrier height increases slowly with increase in number of neutrons in the projectile or the target. However, on inclusion of deformation effects with in optimum orientations, the barrier height increases significantly with increase in neutrons in the projectile/target and the variation is systematic, except that for oblate shaped projectiles where the barrier height and barrier distribution show different profile. In other words, for oblate projectiles the barrier is highest and the barrier position shifts towards smaller interaction radius, independent of the choice of Skyrme forces. The content of spin-orbit density dependent term is found to be only 5-10% of the spin-orbit density independent potential, and act opposite to each other (one repulsive and another attractive), nearly independent of the inclusion of temperature effects. Since deformation and orientation degrees of freedom, and the use of different Skyrme forces, change the barrier characteristics significantly, hence the effects of including the same is tested in the calculation of fusion excitation function of ^{60,64}Ni+^{100}Mo and ^{16}O+^{144,148}Sm reactions within framework of ℓ-summed Wong model, which shows that the new forces GSkI and KDE0v1 respond better than the old SIII force. Further the decay of Yb nuclei, formed in Ca-based reactions which involves stable and radioactive beams of Sn, is studied with in the framework of DCM. The decay pattern of $^{172}Yb^*$ formed in ^{124}Sn+^{48}Ca and ^{132}Sn+^{40}Ca reactions, and corresponding preformation probability, maximum angular momentum (ℓ_{max}), neck length parameter (ΔR) and ΔV_B are studied for the entrance channel dependence and fusion enhancement at comparable $E_{c.m.}$. It is observed that there is decrease in ΔV_B, i.e. increase in fusion probability for ^{132}Sn+^{40}Ca, which lead to fusion enhancement at sub barrier energies. Thus increase in N/Z ratio affect the yield significantly at low energies.

It is worth noting that the above mentioned work has the potential of getting extended to other mass regions such as neutron/proton halo nuclei and super-heavy synthesis for better understanding of the reaction dynamics and associated nuclear structure effects. The use of various Skyrme forces within energy density formalism (EDF) is also being extended with the inclusion of higher order deformations within planar and non-coplanar approach, to understand the heavy ion collisions and related dynamical aspects. Beside this, various nuclear interaction potentials can be explored with in the framework of collective clusterization process to account for ground state and excited state decay mechanism of variety of nuclear reactions. The present work involves to investigate the formation and decay of compound nucleus and hence it would be of further interest to understand the non-compound nuclear mechanism, particularly the ones associated with radioactive ion beams.